Fabrication and Characterization of Sub 5 nm Iron Nanoparticles Deposited on Boehmite, Alumina and Kaolinite Nanoplatelets

By: Xinlong Chen

Thesis submitted to the

Faculty of Graduate and Post Doctoral Studies

In partial fulfillment of the requirements for the degree of

Master of Applied Science

In

Chemical Engineering

Department of Chemical and Biological Engineering

Faculty of Engineering

Abstract

There is a need for new methods of energy production, from sources of any origin, that do not involve the production of carbon dioxide. Hydrogen is increasingly viewed as a promising fuel for transportation. Hydrogen has a high energy density and can replace a significant portion of our fossil fuel consumption. The overwhelming majority of hydrogen produced today (96%) is derived from fossil fuels. Methane has the highest hydrogen-to-carbon molecular ratio of all fossil fuels and is the best raw material for hydrogen production. Direct methane cracking is a reaction that produces hydrogen gas and solid carbon without the production of carbon dioxide.

Magnetite nanoparticles were synthesized using a wet chemical co-precipitation approach with the application of surfactants at selected concentrations. These particles were deposited on various nanoplatelet supports such as boehmite, alumina and kaolinite. Transmission electron microscopy (TEM) and image software were used to characterize the iron oxide nanoparticle morphology and to determine the iron oxide nanoparticle diameters. In-situ Energy-Dispersive X-ray Spectroscopy (EDS) was used to detect the existence of aluminum, iron, silicon and oxygen elements in the sample. X-ray diffraction (XRD) spectroscopy was used to determine the composition of each iron oxide(s)-substrate complex.

Sixty five percent of the unsupported magnetite nanoparticles produced measured less than 5 nm. The nanoparticles deposited on boehmite had 41% of their diameters less than 5 nm. Those co-synthesised with magnetite-boehmite had 81% of their diameters less than 5 nm. When co-synthesized, magnetite nanoparticles and boehmite were observed not to precipitate simultaneously due to the different pH of precipitation of their hydroxides. The nanoparticles deposited on kaolinite had rectangular and circular morphologies. It was found that magnetite nanoparticles deposited on boehmite tend to locate around the perimeter of the nanosheet. Calcination was shown to increase nanoparticle diameters due to nanoparticle coarsening.

Kaolinite delamination was also studied. Kaolinite was ultrasonicated at 30, 40, 50 and 100% power near the solubility of the urea and surfactants. The kaolinite delaminated under the presence of a surfactant was found to have few fractured platelets compared to the results of exfoliation reported in the literature.

Heterogenous magnetite nanoparticles (both deposited and co-synthesized on the substrate) were used in the Fenton degradation reaction of methyl orange. A series of experiments demonstrated that individual stand-alone magnetite nanoparticles with hydrogen peroxide had the fastest degradation rate, while the calcined batches of catalyst-substrate complex have no or miniscule Fenton degradation reaction of methyl orange. Boehmite nanoplatelets were found to act as catalysts in the Fenton reaction. The results were in agreement with the observation that calcination lead to the formation of hematite and maghemite which are not Fenton catalysts.

This work was successful in demonstrating that sub 5 nm iron nanoparticles, with the potential to lead to base growth CNTs, can be made and deposited on open nanoplatelet substrates. All metal oxides produced in this work; magnetite, hematite and maghemite can be used to synthesize CNTs. These catalysts have the proper characteristics to be useful in methane cracking where hydrogen and solid carbon can be produced without the release of carbon dioxide.

Résumé

Il existe un grand besoin de nouvelles méthodes de production d'énergie qui n'impliquent pas la production de dioxyde de carbone. L'hydrogène est de plus en plus considéré comme un carburant prometteur pour le domaine des transports. L'hydrogène a une densité énergétique élevée et peut remplacer une part importante de notre consommation de combustibles fossiles. La majorité de l'hydrogène produit aujourd'hui (96%) provient de combustibles fossiles. Le méthane a le rapport moléculaire hydrogène / carbone le plus élevé de tous les combustibles fossiles et est la meilleure matière première pour la production d'hydrogène. Le craquage direct du méthane est une réaction qui produit de l'hydrogène gazeux et du carbone solide sans production de dioxyde de carbone.

Des nanoparticules de magnétite ont été synthétisées en utilisant une approche de coprécipitation chimique par voie humide avec l'application de tensioactifs à des concentrations sélectionnées. Ces particules ont été déposées sur différents supports de nanoplaquettes tels que la boehmite, l'alumine et la kaolinite. La microscopie électronique en transmission (MET) et un logiciel d'image ont été utilisés pour caractériser la morphologie des nanoparticules d'oxyde de fer et pour déterminer les diamètres des nanoparticules d'oxyde de fer. La spectroscopie à rayons X à dispersion d'énergie in situ (EDS) a été utilisée pour détecter l'existence d'éléments d'aluminium, de fer, de silicium et d'oxygène dans l'échantillon. La spectroscopie par diffraction des rayons X (XRD) a été utilisée pour déterminer la composition de chaque complexe oxyde de fer-substrat.

Soixante-cinq pour cent des nanoparticules de magnétite non supportées produites mesuraient moins de 5 nm. Les nanoparticules déposées sur boehmite et celles co-synthétisées avec magnétite-boehmite avaient respectivement 41 et 81% de leurs diamètres inférieurs à 5 nm. Lorsqu'elles sont co-synthétisées, les nanoparticules de magnétite et la boehmite ne précipitent pas simultanément en raison du pH différent de précipitation de leurs hydroxydes. Les nanoparticules déposées sur la kaolinite avaient des morphologies rectangulaires et circulaires. Il a été constaté que les nanoparticules de magnétite déposées sur la boehmite ont tendance à se localiser autour du périmètre de la nanoparticule. Il a été démontré que la calcination augmentait les diamètres des nanoparticules en raison du grossissement des nanoparticules.

La délamination de la kaolinite a également été étudiée. La kaolinite a été ultrasoniquée à une puissance de 30, 40, 50 et 100% près de la solubilité de l'urée et des surfactants. La kaolinite délaminée en présence d'un tensioactif s'est avérée avoir peu de plaquettes fracturées par rapport aux résultats d'exfoliation rapportés dans la littérature.

Des nanoparticules de magnétite hétérogènes (déposées et co-synthétisées sur le substrat) ont été utilisées dans la réaction de dégradation de Fenton du méthylorange. Une série d'expériences a démontré que les nanoparticules de magnétite autonomes individuelles avec du peroxyde d'hydrogène avaient le taux de dégradation le plus élevé, tandis que les lots calcinés de complexe catalyseur-substrat n'avaient pas ou peu de réaction de dégradation de Fenton du méthylorange. Les nanoplaquettes de boehmite agissent comme catalyseur dans la réaction de Fenton. Les résultats sont en accord avec l'observation selon laquelle la calcination conduit à la formation d'hématite et de maghémite qui ne sont pas des catalyseurs de Fenton.

Ce travail a réussi à démontrer que des nanoparticules de fer inférieures à 5 nm, susceptibles de conduire à des NTC de croissance de base, peuvent être fabriquées et déposées sur des substrats ouverts de nanoplaquettes. Tous les oxydes métalliques produits dans ce travail; la magnétite, l'hématite et la maghémite peuvent être utilisées pour synthétiser des NTC. Ces catalyseurs ont les caractéristiques appropriées pour être utiles dans le craquage du méthane. Réaction par laquelle de l'hydrogène et du carbone solide peuvent être produits sans libération de dioxyde de carbone.

Acknowledgements

The first person to thank is Professor Tremblay for supervising me and the guidance and insight he has given to this project, especially in recipe development for kaolinite exfoliation and nanoparticle synthesis. His rapid response prevented the project from going astray. This project would not have been successful without his enlightening discussions, time, effort, and support.

I also wish to thank Professor Baranova for her course in nanotechnology and her Q/A sessions, the course provided a systematic study of nanoparticle synthesis and its characterization.

I would also like to thank the support staff in the Department of Chemical and Biological Engineering, Franco Ziroldo, Gérard Nina and James Macdermid for technical troubleshooting with many equipment.

Also, I would like to thank Dr. Yun Liu for her work on the TEM and EDS to perform nanoparticle characterization and the insights she has provided on XPS techniques.

Last but not least, I would like to thank my parents and friends for their constant support and encouragement.

Statement of Contributions of Collaborators

I hereby declare that I am the author of this thesis. I performed all the experiments and the data analysis. I have written the chapters contained in this thesis.

Dr. Andre Y. Tremblay supervised this thesis project and provided continual guidance and support. He also made many editorial comments and corrections to the written work presented. His day-to-day guidance, discussion and never-ending support have resulted in tremendous improvements to the thesis.

Table of Contents

List of Figures

List of Tables

Nomenclature and list of abbreviations

$Al_2O_7Si_2H_2O$ – kaolinite

AlOOH – aluminium hydroxide oxide (boehmite)

ASU – air separation unit

ATR - auto thermal reforming (MAR/SMR+MOP)

CMR - combined methane reforming (CMR/DMR+SMR)

CNT – carbon nanotube

MWNT – multiple wall nanotube

SWNT – single wall nanotube

C_P – specific heat capacity ($J/mol \cdot K$)

CTAB - cetrimonium bromide

D – diameter

DI – de ionized

ΔH – change in specific enthalpy (J/mol)

ΔS – change in specific entropy ($J/mol \cdot K$)

DMR - dry methane reforming

EDS - energy-dispersive x-ray spectroscopy

$FeCl_3 \cdot 6H_2O$ - iron trichloride hexahydrate

$FeSO_4 \cdot 7H_2O$ - iron (II) sulfate heptahydrate

FT - Fischer-Tropsch

FESEM - Field-Emission Scanning Electron Microscope

FETEM - Field-Emission Transmission Electron Microscope

GHG – green house gas

h_{phy} – specific enthalpy (J/mol)

HCl – hydrochloric acid

L – length

$M_{avg.}$ – average molecular mass

MPO - methane partial oxidation

MTR - methane tri-reforming

NaOH: sodium hydroxide

NP – nanoparticle

P_0 – reference temperature

P – pressure

PVP - polyvinylpyrrolidone

QM – quantum mechanics

R – ideal gas constant $(J/mol \cdot K)$

RR- Rietveld refinement

S – specific entropy (J/K)

SC - sodium cholate

s_{phy} – specific entropy $(J/mol \cdot K)$

SEM – scanning electron microscope

SL – solubility limit

SMR - steam methane reforming

T_0 – reference temperature

T – temperature

TAN – twinned alumina nanosheet

TEM – transmission electron microscope

TMR – tri-methane reforming

x_i – mole fraction of an induvial component (unitless)

XPS - x-ray photoelectron spectroscopy

XRD – x-ray diffraction

Chapter 1 Introduction

The majority of society's global energy requirements are supplied by fossil fuels [1], [2]. Common pollutants such as CO_2, C_xH_y, NO_x, SO_x and organic vapour products resulting from the combustion of these fuels have caused the continuous deterioration of our environment leading to acid rain and climate change [3]–[5]. Global carbon dioxide emissions increased from 2 billion tonnes in 1900 to over 36 billion tonnes 115 years later [6]. These carbon dioxide emissions originate from the combustion of oil, natural gas and coal in proportions of 35, 20 and 40% respectively [6].

The ever-increasing concentration of CO_2 in the atmosphere and the resulting increase in global temperatures, have driven the interest for alternative energy sources. However, to date, renewable energy has only met 14% of our global energy needs. Biofuels, hydroelectricity, wind, solar and geothermal have contributed 45, 25, 21, 6 and 2% respectively to the renewable energy envelope. Their contributions are all dependant on geographical constraints, feedstock limitations, and food supply considerations. Such limitations on renewables pose serious challenges to the sustainability of our species.

Carbon capture and storage (CCS) offers a partial solution to this problem. In this process CO_2 is captured from point sources, transported to a storage site by pipeline and sequestered by storing it in an underground geological formation. In recent modeling, the management of the storage site is important in mitigating the release of CO_2 to the atmosphere. In a well-regulated onshore storage facility, the leakage over 10000 years could range between 2 and 25%. In a poorly regulated storage facility, the leakage over the same period could range between 7 and 33 %. This indicates that CCS is not a permanent solution to the green house gas (GHG) problem [7].

There is a need for new methods of energy production from sources of any origin, that do not involve the production of CO_2. Hydrogen is increasingly viewed as a promising fuel for transportation. Hydrogen has a high energy storage density and can replace a significant portion of our fossil fuel consumption [8]. The overwhelming majority of hydrogen produced today (96%) is derived from fossil fuels [9]. Methane has the highest hydrogen-to-carbon molecular ratio of all fossil fuels and is the best raw material for hydrogen production [10]–[12]. This hydrocarbon is

available in vast quantities. As of 2019, there were an estimated 7.177 quadrillion cubic feet of total world proved reserves of natural gas [13]. Its known supply is estimated to last over 50+ years [14]. It can be stored in reservoirs and is easy to ship and handle. Methane is abundant in the permafrost and has a 96 times higher global warming potential than CO_2[15]. As the planet warms, it will be increasingly necessary to contain this methane [16] and use it to produce energy.

Research on hydrogen production in the past 4 decades has been driven by its production for use in fuel cells. Many hydrogen production pathways utilizing methane reforming have been proposed and explored, each have advantages and disadvantages. The hydrogen produced in methane reforming must be purified in a complex separation process that requires high capital investment and operating expenditures.

The carbon dioxide produced in methane reforming processes must be sequestered to reduce its environmental impact [17]–[24]. This involves the need for carbon capture systems. Issues related to storage and transportation of CO_2 to storage sites challenge the viability of the production of hydrogen using methane steam reforming.

Direct methane cracking is a specific chemical reaction that produces hydrogen gas and pure carbon without the production of CO_2. This reaction offers the possibility of storing the reaction product as a solid rather than gases as is the case with present CCS approaches. It offers an everlasting solution to global warming as coal beds have remained stable over millions of years. The reaction could eventually lead to energy generation from fossil fuels that achieves zero carbon dioxide emissions.

One of the most significant technical hurdles towards industrial-scale thermo-catalytic methane cracking for hydrogen production is catalyst deactivation due to coking on the catalyst surface [25]. Various catalyst regeneration methods have been proposed such as air [26]–[32], steam [26], [33]–[35] and dry regeneration [29], [36]–[38], however, the original catalyst performance is not recovered due to the persistent accumulation of coke on the catalyst. It would be a great advantage if catalyst activity were maintained during this reaction.

The fabrication of carbon nanotubes (CNTs) provides insight in sustaining catalyst activity. The carbon produced during the cracking reaction proceeds at the micron level [39], [40] whereas CNT synthesis happens at the nanometer level [41]. There are two types of growth modes in CNT

fabrication, i.e., tip and base growth. For tip growth, the reactive site on the catalyst is encapsulated by solid carbon and leaves the surface of the catalyst leading to catalyst deactivation [42][43]. In the base growth mode, carbon encapsulation of the catalyst nanoparticle does not occur and the nanoparticles remain on the surface of the catalyst. The catalyst's surface remains exposed to the reactant gas and catalyst activity is maintained [44].

The growth of carbon nanotubes on surfaces can be achieved by synthesizing catalytic nanoparticles that have an appropriate diameter to avoid the tip growth mode of CNTs. The critical diameter for base growth (surface growth) is approximately 5 nm for iron nanoparticles deposited on common substrates. The 5 nm nanoparticle size delimits the boundary between base and tip growth. As previously mentioned, if particles grow by the tip mechanism, then the metal nanoparticle on the surface of the catalyst will be lost and a metal-carbon compound will be produced. This can lead to the loss of metallic sites on the catalyst and deactivation. Growing the nanotube on the surface of the catalyst and releasing the nanotube is the desirable outcome for this future process.

In order to release carbon nanotubes, the catalyst support must be very open. Twinned alumina nanosheets have been synthesized in our laboratories [45], [46]. Delaminated kaolinite is another thin nanosheet candidate to support the metallic nanoparticles. Iron nanoparticles can be used as catalysts as they are non-toxic, widely available and inexpensive compared to other metals.

The primary objective of nanoparticle fabrication is to synthesize non-aggregated nanoparticles that are close to the critical size for the base growth of CNTs in order to prevent catalyst deactivation. The aim of this work is to synthesize sub 5 nm iron nanoparticles and deposit them on several types of nanosheets. The reactivity of the catalysts produced is this work will be determined using a Fenton reaction to degrade methyl orange.

Objectives and Thesis Structure

The objective of this thesis is to fabricate catalysts having iron oxide nanoparticle have diameters less than 5 nm supported on boehmite, alumina and kaolinite nanoplatelets. This is to eventually

enable direct methane cracking and produce hydrogen without the formation of CO_2 as a coproduct. The thesis is divided into six chapters as follows:

Chapter 1 Introduction and Objectives

Chapter 2 Background and Literature review.

This chapter contains a comprehensive literature overview that presents the current status of reaction pathways and thermodynamics used for direct methane cracking for hydrogen production. It also covers the fabrication of iron-based nanoparticles and kaolinite exfoliation.

Chapter 3 Kaolinite Exfoliation Using Low-Temperature Urea.

This chapter describes the experimental results for the delamination/exfoliation of kaolinite in large sheets. In this chapter, a significantly modified procedure for kaolinite exfoliation was developed. The modified procedure includes using greater ultrasonicator power (intensity), urea concentration and the introduction of surfactants to enhance kaolinite exfoliation.

Chapter 4 Magnetite Nanoparticle Synthesized on Aluminum-based Substrates.

This chapter describes the synthesis of magnetite nanoparticles using a wet chemical coprecipitation approach and their deposition on boehmite, alumina and kaolinite nanosheets. SEM and TEM with EDS along with statistical analysis via image processing software ImageJ were used to characterize the magnetite nanoparticle size, morphology, degree of aggregation and distribution. XRD spectroscopy revealed which materials were present during the nanoparticle fabrication procedure. The diameter, morphology and distribution relations of iron-based nanoparticles deposited on alumina-based substrates were statistically analyzed.

Chapter 5 Magnetite catalyzed Fenton degradation reaction of Methyl Orange

This chapter describes studies on the degradation of methyl orange using selected catalysts produced in this work.

Chapter 6 Conclusions and Recommendations for future work.

Chapter 2 Background and Literature Review

In the future, fossil fuels as a source of energy will most likely be required to be substituted by hydrogen [47]. If hydrogen were to become a mainstream fuel for transportation, its production would need to reach 100 and 13 845 tonnes per day [48] per day in order to achieve full scale hydrogen economy. Industrially, hydrogen is currently produced by catalytic steam reforming [49]–[54], a mature technology that produces 70 million tons of hydrogen annually. However, in this process 9 to 12 tons of CO_2 are produced for every ton of hydrogen synthesised [55]. This process has a considerable environmental impact and a substitute process must be found if hydrogen is to become a major source of energy for transportation.

Carbon capture and storage (CCS) is currently under study to reduce this environmental burden. Here, carbon dioxide is stored in underground reservoirs preventing its release to the atmosphere [56]. Goto *et al*. calculated the energetic cost of using this technique and is approximately 3.6 GJ/t_{CO_2} spent to capture 99% of carbon dioxide emission stream at high purity [57]. The possibility of CO_2leaking from underground CO_2 reservoirs over 1000 years is a growing concern, as some carbon dioxide is already leaking from some reservoirs [58].

Catalytic methane cracking can be considered as a vital bridge technology from the current carbon emission-intensive energy systems to the widespread use of novel fuels [59]. Methane undergoes thermal decomposition at temperatures above 1300 °C, however, under the presence of a catalyst, the cracking reaction can proceed at the lower temperature of 650K (376.85°C) [60]. Direct methane cracking has three advantages over steam reforming; lower heat input, no carbon dioxide production and integrated final product separation. With integrated final product separation, a gas separation unit can be eliminated thus reducing the complexity and capital cost of the system. Typically, an inert gas is fed along with the methane in the reactor to control coking.

Fluidized bed reactors are the most common type of reactors for methane cracking. A fluidized bed reactor is convenient for catalytic methane cracking reaction since it allows the continuous addition or removal of solid particles. The catalyst can be looped between the cracking reactor and the carbon extractor unit based on the deactivation rate of the catalyst. Compared to conventional

fix bed reactors, fluidized bed reactors allow greater temperature control, and greater heat and mass transfer due to more exposure to the catalyst [35], [36], [61].

Recently novel reactors have been developed, such as solar and membrane reactors. Rodat et al. [60] tested a pilot scale solar furnace methane cracking reactor, and it was found that the solar reactor achieved high methane conversion (~95%) and hydrogen yield (~77%) when the reactor temperature approached 1700K. Total methane conversion (100%) and highest hydrogen yield (~80%) when the reactor temperature surpasses 1775K. However, despite having achieved high methane conversion, their highest thermochemical and thermal efficiencies were 13.5% and 15.2%, respectively. The thermochemical efficiency is less than the thermal efficiency is due to the fact there was an inert argon gas mixture with the methane feed and unreacted methane exited the reactor.

Membrane reactors are particularly interesting in this regard since they can affect reaction and separation in one operation. The cracking reaction in membrane reactors proceeds at much lower temperatures compared to their non-membrane reactor counterpart. The significant advantage of using a catalytic membrane reactor for direct methane cracking is its ability to separate in-situ and exploit the Le Chatelier principle [62]. Applying the Le Chatelier principle can increase both hydrogen production and concentration with faster reaction kinetics and lower operating temperature requirements [20], [63]–[67]. For example, Ishihara et al. achieved near 100% methane conversion operating at 775K while packed bed reactors (PBR) only reach 45% methane conversion [68].

Nickel and palladium are the most common metal catalysts studied in the methane cracking processes [60], [69]–[72]. Activated carbon was also studied in indirect methane cracking [73]–[75]. Nickel and palladium had a higher performance than the activated carbon catalyst in terms of methane conversion and hydrogen yield. However, both nickel [76] and palladium [77] compounds are classified as human carcinogens [78], [79]. Both metal catalyst and activated carbon have been extensively studied in fluidized bed reactors configurations. Recently, rare-earth metal alloys used for catalysts were studied in a membrane reactor configuration with high methane conversion and hydrogen yield with very limited coking [70], [80], [81]. Despite the high performance of rare earth metal catalysts, the availability of rare earth metals is insufficient to meet the requirements for large scale hydrogen production. In order to scale methane cracking at the

industrial level, a catalyst made from an abundant material that does not comprise catalytic performance has to be selected. In this regard, iron is a promising catalyst material. It is available in vast quantities and far less toxic than other alternatives [82]. Iron has better performance when operating at temperatures greater than 700K compared to Ni catalysts [20], [66], [67], [83]–[85]. However, it exhibits lower catalytic activity than nickel when the operating temperature is lower than 700K [82]. Recently, Ibrahim et al. [86] and Fakeeha et al [87] conducted methane cracking reactions using iron as the catalyst. They observed considerable coking on the catalyst after only 4 hours of operation.

Laboratory scale experiments have demonstrated that one of the main technological hurdles preventing the development of methane cracking processes on the industrial-scale is carbon deposition on the catalyst leading to deactivation. The same material shrunken down to the nanometer scale has completely different physical and chemical properties due to surface and electronic effects [88]. Most works reporting methane cracking reaction under the presence of iron-based catalysts are devoted to study the characteristics Multi Walled Carbon Nanotubes (MWCNTs) fabrication [66], [67], [82], [89].

Methane cracking has a low energy requirement and no side reactions as will be demonstrated in the next section which presents the reaction pathways and their thermodynamics. Iron nanoparticle synthesis, kaolinite exfoliation using low-temperature urea and magnetite nanoparticle synthesized on aluminum-based substrates are also presented.

2.1 Reaction Pathways and Thermodynamics

In general, there are four reaction pathways for industrial-scale hydrogen production: 1). Steam methane reforming; 2). Dry methane reforming; 3). Direct methane cracking, and 4). Water spitting. Currently, steam methane reforming is the dominant process for industrial hydrogen production. The reaction pathways will be described based on the reactants needed, products produced and operating conditions. The advantages and disadvantages of each reaction path are also presented in the following sections.

2.1.1 Steam Methane Reforming

Approximately 80 to 85% of the world's hydrogen is produced by methane-steam reforming [22], [90], [91] as shown in Eq. (2.1);

$$CH_4(g) + 2H_2O(g) \rightarrow CO_2(g) + 4H_2(g) \quad \Delta H°_{f_{298.15K}} = 164.7\,kJ/mol \tag{2.1}$$

The hydrogen produced is separated from the gas mixture by pressure swing adsorption [17], [92] or by a membrane separator [93].

Methane steam reforming is a multistage process. The first stage is an endothermic reaction shown in reaction 2.2 and requires a high temperature between 800 to 900°C in order to proceed. The end products are mixed CO and H_2 gases. However, the separation of these two gas products is complicated. This reaction is highly endothermic; heat can be supplied by either the additional combustion of methane from the initial feed or combusting the hydrogen product after separation or supplying additional electrical heating. The reforming process has a mild energy efficiency (65-75%) and high carbon dioxide emission due to hydrogen production and heat produced from reaction 2.3 [21], [90], [94]. This is counterproductive with regards to GHG reduction objectives.

$$CH_4(g) + H_2O(g) \rightarrow CO(g) + 3H_2(g) \quad \Delta H°_{f_{298.15K}} = 206\,kJ/mol \tag{2.2}$$

$$CO(g) + H_2O(g) \rightarrow CO_2(g) + H_2(g) \quad \Delta H°_{f_{298.15K}} = -41.17\,kJ/mol \tag{2.3}$$

The second stage is the water shift reaction, shown in second reaction (Eq. 2.3) is an equilibrium reaction. This involves a 2-step reaction;

1). The 1st step (reforming) is performed at a temperature range between 400 to 500°C in order to reduce CO concentration from 2 to 5% vol (Eq. 2.2).

2). The 2nd step (water shift) is performed at a temperature range between 177 and 257°C in order to reduce CO concentration to 1% vol. Yielding essentially a mixture of CO_2 and H_2 (Eq. 2.3).

If the hydrogen product is to be used in a fuel cell, the last stage of the process involves the separation of CO from the products as CO can poison PEM catalysts used in hydrogen fuel cells. A pressure swing absorption unit is used to separate CO and H_2 gases in the final stage [29], [95], [96].

2.1.2 Dry Methane Reforming

Hydrogen can be produced while consuming CO_2 by the dry methane reforming reaction as shown in reaction 2.4.

$$CH_4(g) + CO_2(g) \rightarrow 2H_2(g) + 2CO(g) \quad \Delta H°_{f_{298.15K}} = 246.98\,kJ/mol \tag{2.4}$$

The most challenging technical hurdle in using this approach are the many side reactions occurring in the process. These side reactions will eventually consume the hydrogen product. The reactants and products from both initial and side reactions will have to be separated. The CO and H_2 gases produced in reaction (2.2) and (2.4) are challenging to separate. The following side reactions are involved during the dry methane reforming process Eq. (2.5) to (2.7);

$$CH_4(g) + H_2O(g) \rightleftharpoons CO(g) + 3H_2(g) \quad \Delta H°_{f_{298.15K}} = 205.81\,kJ/mol \tag{2.5}$$

$$CH_4(g) + CO_2(g) \rightleftharpoons 2CO(g) + 2H_2(g) \quad \Delta H°_{f_{298.15K}} = 246.98\,kJ/mol \tag{2.6}$$

$$H_2(g) + CO_2(g) \rightleftharpoons CO(g) + H_2O(g) \quad \Delta H°_{f_{298.15K}} = 41.17\,kJ/mol \tag{2.7}$$

As seen in Eq. 2.7, the reverse water-gas shift reaction consumes the newly produced hydrogen to form water [97]. This problem is not well acknowledged because the vast majority of dry reforming reactions are conducted at atmospheric pressure, where the water production is at a minimum as described below (Eq. 2.8);

$$CO(g) + H_2O(g) \rightleftharpoons CO_2(g) + H_2(g) \quad \Delta H°_{f_{298.15K}} = -41.66\,kJ/mol \tag{2.8}$$

Conventional steam reforming for hydrogen production does not have this problem because the water shift reaction is favoured, and therefore more hydrogen gas can be produced during the reaction process. Moreover, as long as the pressure $P > 5atm$, Eq. 2.7 dominates the dry reforming process, this is because CO_2 is favored towards Eq. 2.7 due to a higher reactivity of H_2 over CH_4 [97].

The use of a membrane reactor can shift the reaction towards the product side. If the produced hydrogen is purged before it can react with the carbon dioxide, then the reverse water-gas shift can be eliminated or minimized. However, the membrane must have the capability of withstanding the high pressure and temperature operating conditions during the dry methane reforming process [80].

2.1.3 Direct methane cracking

Currently, there are no economic and mature technologies to capture and store CO_2 during hydrogen production. A practical approach to reduce CO_2 emissions is to avoid its generation altogether. Compared to methane-steam reforming, catalytic methane cracking is a more attractive route for hydrogen production because there is no CO_2 generation. Also, this process has the lowest energy requirement for industrial-scale hydrogen production [61]. The most distinguished feature of his reaction route is integrated in-situ carbon sequestration and hydrogen separation as expressed in Eq. (2.9);

$$CH_4(g) \rightarrow C(s) + 2H_2(g) \quad \Delta H°_{f_{298.15K}} = -74.6\,kJ/mol \tag{2.9}$$

The reaction can proceed at a reasonable rate when the operating temperature is greater than 600℃ [61]. Various production methods were proposed in literature such as the solar radiation [98], [99], plasma [18], molten metal bath [19] and thermal reactors that do not use catalysts [100] and with metallic catalyst [20], [26], [63], [101] as well with active carbon catalyst [61], [73], [102], [103].

2.2 Iron Nanoparticle Synthesis

Nanoparticles (NPs) have much different mechanical, thermal and magnetic properties compared to their bulk counterparts [104]. It was also found that the particle size and its size distribution of nanoparticles play a key role in governing their properties [105], [106]. Two fundamental properties that make nanoparticles unique are their high specific areas and electronic properties [88]. High specific areas provide a great opportunity for surface catalytic reactions [107]. The size of nanoparticles lies between 0.5 to 100 nm [108]. For the transition range between 2 to 10 nm, neither quantum mechanics nor classic physics can be used to explain their properties [109]. When a strong chemical bond(s) is present between the atoms of the nanoparticle, the delocalization of valence electrons can be extensive and can vary with size; this in turn can lead to different chemical and physical properties [109].

Magnetite nanoparticles possess catalytic activity with respect to methane cracking. Catalyst recovery is easier due to the magnetic properties of magnetite compared to non-magnetic nanoparticles. CNTs are typically grown on magnetite and not hematite ($\alpha - Fe_2O_3$) . Magnetite possesses catalytic activity for CNT growth [110], [111]. Maghemite ($\gamma - Fe_2O_3$) is the allotropic form of magnetite (Fe_3O_4). These two iron oxides are crystallographically isomorphous and the main difference between the two is the presence of ferric ions only in $\gamma - Fe_2O_3$, and both ferrous and ferric ions in Fe_3O_4. The magnetic properties of Fe_3O_4 are superior than $\gamma - Fe_2O_3$, however maghemite is far more stable as it cannot be farther oxidized. However the catalytic activity of maghemite is not well studied [112].

The synthesis of sub 5 nm metal nanoparticles [113] is the main limitation towards the industrial-scale production of hydrogen via thermo-catalytic methane cracking. To date, extensive studies were performed, and the results are available in the literature covering various iron salts, their types, surfactant concentrations and solvents used in their synthesis.

In order to achieve successful CNT base growth mode, the nanoparticle must be deposited on a substrate and it must not detach during the cracking reaction. The nanoparticle must also maintain its catalytic activity throughout the entire reaction [114].

Regarding the nanoparticle synthesis, for example of magnetite nanoparticles, many synthesis routes have been explored, such as the wet chemical synthesis [115]–[117], gas-phase flame synthesis [118] and electrochemical synthesis [119]. In these synthesis approaches, the so-called wet chemical synthesis is widely used because of its simplicity, versatility and economic viability.

In order to synthesize magnetite nanoparticles, an initial mixture of both Fe^{2+} and Fe^{3+}-based salts are prepared. To prevent Fe^{2+} based salts to prematurely oxidize to Fe^{3+} salts, an acid is often added to the iron salt solution. It was reported [120] that adding a strong acid such as HCl into a solution can prevent Fe^{2+} oxidation; but this addition of a strong acid can lead to a low pH of the solution and interfere with the NP synthesis. This interference can be minimized by utilizing a weak acid so that a low pH can be avoided. The synthesis of magnetite nanoparticles is expressed by the following chemical formula Eq. (2.10);

$$Fe^{2+} + 2Fe^{3+} + 8OH^{-} \rightarrow Fe_3O_4 + 4H_2O \tag{2.10}$$

2.2.1 Monodispersed iron nanoparticles

Monodisperse nanoparticles can be fabricated by wet chemical synthesis and deposited on a substrate. The wet chemical synthesis approach is versatile and can be industrially scaled. A dot-matrix nanoparticle distribution layout can be obtained by much more complex methods such as physical vapor deposition (PVD), chemical vapor deposition (CVD) and atomic layer deposition (ALD) techniques [88].

Monodisperse nanoparticles with a size variation of less than 5% normally show unique properties and higher performances as compared to polydisperse nanoparticles [121]. The advantages of having near equal separation between nanoparticles is that it reduces the possibility of nanoparticles aggregation. If the separation between each nanoparticle is sufficient, nanoparticles coarsening can be avoided during the calcination process [122], [123].

Park et al. [124] produced individual iron nanoparticles with diameter from 4 to 11 nm by refluxing a solution of 0.2 mL of 1.52 mmol of iron pentacarbonyliron ($Fe(CO)_5$) mix with 10 mL dioctyl ether and 1.28 g oleic acid at 373 K. The mixture was refluxed at 100°C for 1 hour and then the solution was cooled down to room temperature. Anhydrous trimethylamine N-oxide ($((CH_3)_3NO \cdot H_2O)$ was added to the refluxed solution. The solution was then heated to 403 K in an argon atmosphere and maintained at this temperature for 2 hours and transitioned from brown to black. The function of the organic component of iron pentacarbonyliron is to prevent aggregation. Thermal decomposition removes the organic component of the iron pentacarbonyliron after synthesis.

They used iron oleate solutions to prepare iron nanoparticles. Seven combinations of iron oleate solutions were prepared and the average iron nanoparticle's diameter are listed in Table 2.1. The initial and the final diameter was measured just before and after refluxing with pentacarbonyliron and oleic acid in dioctyl ether at 403 K for 12 hours.

TEM images were used to measure the nanoparticle diameters. The standard distribution of the particle sizes ranged from $\sigma = 8.5\%$ (standard deviation) for the 6 nm particles to $\sigma \leq 5\%$ for all other particles. The iron nanoparticle's diameter was also determined by the molar ratios of $Fe(CO)_5$ and oleic acid. From Table 2.1, it was observed that increasing iron oleate concentration increases the iron nanoparticle's diameter.

Table 2.1: Size of the final Fe nanoparticles synthesized from various combinations of initially monodisperse Fe nanoparticles and iron oleate solutions.

Iron oleate solution (mmol)	**Initial iron nanoparticle diameter (nm)**	**Final iron nanoparticles diameter (nm)**
1.5	4	6
3	4	7
1.5	8	9
3	8	10
1.5	11	12
3	11	13
4.5	11	15

2.2.2 Anion effects of iron salts in the synthesis of iron nanoparticles

A study by Yazdani et al. [125] examined the effect of anions on the magnetite nanoparticle diameter of two Fe^{2+} anion salts and three Fe^{3+} anion salts. The six combinations of these salts used in the study are list below,

1) $FeCl_2 \cdot 4H_2O$ and $FeCl_3 \cdot 6H_2O$;
2) $FeCl_2 \cdot 4H_2O$ and $Fe_2(SO_4)_3$;
3) $FeCl_2 \cdot 4H_2O$ and $Fe(NO_3)_3 \cdot 9H_2O$;
4) $FeSO_4 \cdot 7H_2O$ and $FeCl_3 \cdot 6H_2O$;
5) $FeSO_4 \cdot 7H_2O$ and $Fe_2(SO_4)_3$;
6) $FeSO_4 \cdot 7H_2O$ and $Fe(NO_3)_3 \cdot 9H_2O$.

According to these combinations, an attempt was made to evaluate the effect of the anion combinations on the diameter of the nanoparticle. Stock solutions of 0.1 M Fe^{2+} and 0.1 M Fe^{3+} were combined to produce the Fe_2O_4 precipitate. An excess of 1M NaOH was used as the base. It was observed that anions of weaker ionic strength resulted in a decrease in the magnetite

nanoparticle diameter. It was suggested that larger anions usually lead to smaller diameter magnetite nanoparticles[125].

Extensive studies were conducted to identify the effect of organic anions on the formation of iron oxide (magnetite and maghemite) nanoparticle diameter distribution [126]–[128]. It was demonstrated that citrate ions could affect the growth and the diameter of iron oxides [128]–[130]. Furthermore, a correlation was established concerning the citric acid concentration and diameters of both spherical and polydisperse magnetite and maghemite nanoparticles [131].

The typical maghemite nanoparticle diameter is around 8 nm without the presence of citrate ions, while upon the presence of citrate ions, the maghemite diameter can reach as small as 2 nm. Generally, the maghemite nanoparticle diameter was found to follow a decreasing trend with increasing the citric acid concentration.

2.2.3 Iron Oxide Nanoparticles produced in Microreactors

Simmons et al. [132] used the iron(II) chloride tetrahydrate, iron(III) chloride, NaOH and 35% HCl to fabricate the magnetite nanoparticles. A precursor iron salt solution was made first by mixing 0.01M of iron (II) chloride in 1.1 M HCl aqueous solution, and the solution was then purged of oxygen with nitrogen gas for an hour before usage. From Figure 2.1, the iron nanoparticles have an average diameter between 3 to 3.5 nm; however, the nanoparticles have a tendency to agglomerate as surfactants were not used in this study.

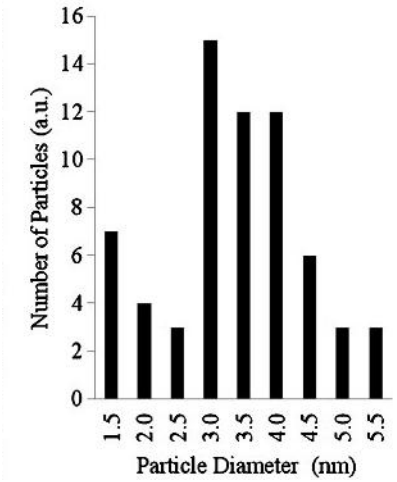

Figure 2.1: Size distribution of the nanoparticles produced at a total flow rate of $3000\ \mu L/h$ of the microreactor sample [132].

2.2.4 Surfactant Effect on the synthesis of iron nanoparticles

An effort was made to investigate the effect of a positively charged surfactants on the size, morphology and structure of magnetite nanoparticles fabricated by coprecipitation. Cetrimonium bromide (CTAB, $[(C_{19}H_{42})N(CH_3)_3]Br$) is a cationic surfactant that interferes with the negatively charged external iron oxide nanoparticle's crystal surface produced during coprecipitation within an alkaline pH. For example, it is reported that CTAB was widely used as a surfactant for the synthesis of Au nanorods where it was found that CTAB can affect the nanoparticle size and shape.

Filippousi et al. [133] used Iron(II) sulphate heptahydrate ($FeSO_4 \cdot 7H_2O$), CTAB to fabricate iron nanoparticles, in which the resulting precipitates were continuously stirred for 20 minutes in a conical flask with a magnetic stirrer. The black precipitates were then collected by centrifugation and washed several times with distilled water and dried by freeze drying.

The surfactant did not change the geometry and structure of the iron oxide nanoparticles produced. The batch without surfactants produced the smallest diameter magnetite nanoparticles, however it also resulted the highest degree of aggregation. The presence of surfactant did control the degree of aggregation of the produced nanoparticles due to hydrophobic interaction [134]. Selected area electron diffraction (SAED) was used to determine the particle size distribution of Fe_3O_4

nanoparticles. Figure 2.2 shows the size distributions of iron nanoparticle produced without surfactants and with PVP, sodium cholate (S.C.) and CTAB with average diameters of 7.5, 9, 9.7 and 11.5 nm respectively. The presence of surfactant PVP and S. C. in the manufacturing process results in a larger particle diameter, while the CTAB leads to the largest nanoparticle diameter. From Figure 2.2, the surfactant has a strong influence on the iron oxide nanoparticle's diameter due to the surfactant ability to control the iron nanoparticle aggregation.

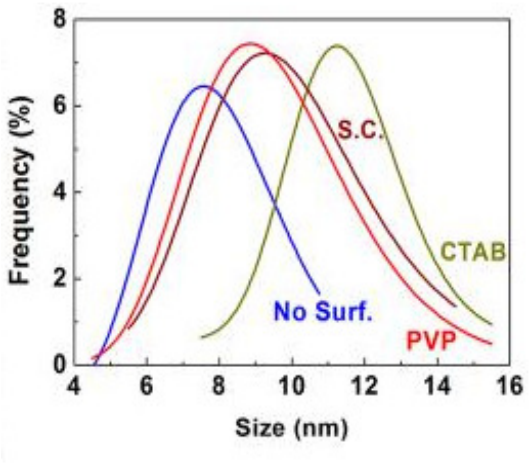

Figure 2.2: The particle size distribution of all the studied samples. [133]

Although the lower crystallite size values may be attributed to the aggregation of the iron oxide nanoparticles (Figure 2.2), the crystallite sizes depends on the choice of surfactant.

2.2.5 Deposition on substrate

Iron deposition on alumina and silica by utilizing physical and chemical deposition methods are reported in literature [135]–[137]. Moody *et al*. have synthesized iron oxide nanoparticles on a silica membrane [136]. The iron oxide nanoparticles were calcined with a gas mixture of hydrogen and argon in order to prevent magnetite to oxidize into hematite or maghemite. The magnetite nanoparticle was well distributed (spacing between each nanoparticles) from each other and hence no large nanoparticle aggregates were spotted in their TEM images.

Another example of depositing nanoparticles on a thin film of silica was conducted by Gohier et al. [135]. They deposited cobalt, iron and nickel nanoparticles of different mean diameters on a

thin film of silica by PVD method. These films were then annealed under vacuum at 700°C in order to form nano-scale islands. The nano-scale islands had distance greater than 10 nm between each nanoparticle deposited on the substrate.

2.3 Substrates

2.3.1 Kaolinite delamination

Kaolinite ($Al_2(OH)_4Si_2O_5$) is a widely used industrial clay mineral. It is used in many applications, including paper coating, plastic filler, adhesives, ink extender, enamels, and molecular sieves [138]. Kaolinite is a layered silicate mineral, with one tetrahedral sheet of silica (SiO_4) linked through oxygen atoms to one octahedral sheet of alumina (AlO_6) [139]. The adjacent layers of kaolinite are tightly held together by hydrogen bonds between the OH groups on the octahedral (aluminum) sheets and the tetrahedral (silicon) sheets [140].

Exfoliation is a process where large aggregates are broken into smaller platelets. This process is traditionally implemented by mechanical approaches such as by grinding or stirring. For instance, the traditional exfoliation process typically shatters kaolinite layers into smaller pieces. Delamination is another process that separates each individual aggregate layers into thin platelets. To date, several grinding techniques were applied to exfoliate kaolinite; however, these techniques are both energy and labour-intensive processes.

Fast milling is a technique of kaolinite delamination; however, the fast milling of kaolinite result cracking along the basal planes, which leads to platelet cracking and an increase in the number particles [141], [142]. Frost et al. [143], [144] carried out a series of kaolinite delaminations and found that the specific surface area increases during the first two hours of milling. After 10 hours of milling, however, the specific surface area decreases due to the agglomeration of the platelets [145]. Mechanical grinding of kaolinite could result in a disturbance of its periodicity along specific direction due to reducing dimensions of crystallite below the critical size necessary to meet coherent x-rays scattering [142], [146]. Ultrasound has also been used to delaminate kaolinite. In this situation, the specific surface normally increases causing structural disorder because of translation defects between the 1:1 layer [147].

Urea delamination [148], [149] and dry grinding in a ball mill [150] are two methods to delaminate kaolinite. Tsunematsu *et al.* [150] conducted a series of delamination of kaolinite by using a ball mill, mechanical mortar and a combination of both devices, with and without urea. Their conclusion indicated that ball milling of the urea-kaolinite solution is an ineffective approach for kaolinite intercalation. The mechanical grinding of kaolinite for a week at 45% humidity in the presence of a urea solution of 5, 10 and 30% wt. urea content was found to be more effective than grinding without urea. As a result of such a process, the specific areas of the processed kaolinite were then increased from 20.8 to 34.4 and 36.5 m^2/g for grinding in 5, 10 and 30% wt. urea solutions respectively. Another kaolinite grinding test was conducted by Tsunematsu et al. [151] in 30% wt. urea for two days at 95°C. The kaolinite urea colloid solution was brought to a boil and washed five times in water. The specific area of the processed kaolinite was increased from 18 to 116 m^2/g. The processed kaolinite platelets were thinner compared to the unprocessed kaolinite platelets.

2.3.2 Boehmite

Due to its high specific surface area and negative surface charge, boehmite, known as "transition alumina" is often used as a catalyst support [152]–[154]. Atomic diffusion, sintering and grain growth occur, during phase transformation from γ to α alumina resulting in a decrease of specific surface area. Experiments were conducted to slow down such phase transformation to α-alumina either by use of additives, i.e. silica, phosphoric acid, barium hydroxide, cerium a oxides and lanthanum oxides [155], [156] or by controlling the morphology of boehmite precursors. A number of chemical synthesis approaches were tested to control morphology and porosity [157]–[160] of boehmite powders to hence maintain the high surface area and porosity.

Hochepied et al. [159] studied the precipitation conditions (pH and temperature) that affect morphology and porosity of boehmite particles, and concluded that : 1) if the initial conditions lead to formation of an isolated amorphous hydroxide and subsequently transformed into boehmite, then porous particles are formed by the agglomeration of boehmite nanocrystals; 2) if the initial

conditions lead to the formation of a crystallized boehmite phase, then polycrystalline nanofibers are obtained.

2.3.3 TAN

Roebuck et al. [45] calcined boehmite into twinned alumina nanosheets (TAN) at 600°C for 4 hours in muffle furnace. The original boehmite rhombic shape is still kept after calcination into TAN. Ab initio MD simulations showed that at higher temperatures of 800 and 1100 K, respectively, that this monolayer is still stable at 1100 K [161]. Since the monolayer is stable at 1100 K, the thicker TAN counterpart is much more stable as it is closer to bulk $\alpha - Al_2O_3$.

The surface charge distribution of TAN is different compared to their bulk $\alpha - Al_2O_3$ counterpart [161]. The oxygen atom in alumina when it is monolayer state is less electronegative, however, it covers a larger area and thus reducing the positive charged area contributed by the aluminum atom. These properties along with high dispersion ratio provides more opportunities for a positively charged nanoparticle to be deposited on the surface of the alumina nanosheet and a negatively charged particle on the edge of the nanosheet.

The band gap of bulk $\alpha - Al_2O_3$ is 8.6 eV whereas a monolayer is calculated to be 5.99 eV, these observations suggests that TAN has band gap in between bulk and monolayer alumina with leaning towards monolayer alumina when the thickness of TAN is reduced.

Chapter 3 Kaolinite Exfoliation Using Low-Temperature Urea

Xinlong Chen, A. Y. Tremblay

The manuscript for submission, Xinlong Chen, A. Y. Tremblay

Abstract

Traditional kaolinite exfoliation/delamination techniques typically result in the fracturing of kaolinite nanoplatelets. In this work, a new procedure for kaolinite delamination was developed. The new procedure involves the periodic operation of an ultrasonicator at its maximum power consisting of 10 s on and 1 min off pulses and the use of urea (50% wt. solution) and surfactants near their solubility limit. The delaminated kaolinite was characterized by scanning electron microscopy (SEM). The circular equivalent diameter and the circularity of the particles produced as a result of delamination were calculated using the image analysis software ImageJ.

The introduction of a surfactant significantly altered the morphology of the delaminated kaolinite. Adding CTAB into 50 % wt. urea solution produced single or multilayer kaolinite nanoplatelets with circular edges, 50% wt. urea solution is near the solubility limit of urea in water. Fine kaolinite nanoplatelets were not formed when the surfactant PVP K30 was used. The geometric morphology of the platelets was different compared to the CTAB batch, as the vertices of the particles were much sharper. The morphology of the platelets using PVP-10 was circular and had a “dish” like structure.

It was concluded that the presence of surfactant has positive effects on kaolinite delamination process to form nanoplatelets. The kaolinite is delaminated to a greater extent when higher ultrasonication power and a high concentration of urea and surfactant are used. Kaolinite is most delaminated when the concentration of urea and surfactant is near its solubility limit and at the highest sonication power.

Keywords: Kaolinite, exfoliation, delamination, ultrasonication, urea, surfactants, CTAB, PVP K30, PVP-10, sodium cholate

3.1 Introduction

The separation of kaolinite particles into thin platelets is referred to as delamination. It is typically conducted by mechanical grinding or stirring. Exfoliation is a process of breaking large aggregates into smaller particles, whereas delamination is defined as the process of separation of individual layers from larger laminated particles. Exfoliation is the process that cuts parallel to the (001) crystal planes, fracturing the platelets, breaking the kaolinite structure and thus increasing its specific surface area [162], [163].

It was suggested that the fast milling of kaolinite can cause fracturing along basal planes, increasing its specific surface area [141], [142]. Frost et al. [143], [144] conducted studies on kaolinite delamination and observed that the specific surface area increases during the first 2 hours of milling and then decreases after 10 hours of milling due to agglomeration [145]. The kaolinite layers are tightly held together by hydrogen bonds between OH groups on octahedral (aluminum) sheets and the tetrahedral (silicon) sheets [140]. Compared to the delamination process through mechanical grinding, ultrasonication normally increases the specific surface area, however, it causes structural disorder because of translation defects in the basal plane [147].

The effect of both mechanical and chemical processes on the grinding of kaolinite, including the structure and thermal transformation behaviour [164], [165]. Using XRD spectroscopy they found that the A band shifted slightly downward in frequency while the D band increased in frequency. The mechanical grinding of kaolinite disturbs its periodicity along the basal plane because the dimensions of the crystallites drop below the critical size needed to have coherent x-ray scattering [142], [146]. These structural changes broaden the x-ray diffraction signal peaks and decrease the x-ray intensity.

Chemical delamination of kaolinite induced by the chemical intercalation of urea, ammonium acetate, hydrazine and or potassium acetate combined with the mechanical process [145], [150], [166]–[168] cause the weakening of the hydrogen bond of the interlayer. This facilitates the displacement of kaolinite layers and their detachment form larger stacks. Weiss and Thielepape [148] conducted the first observation of kaolinite delamination by grinding kaolinite in aqueous urea in 1963. Folded thin particles were observed under a SEM after grinding kaolinite in an

ammonium acetate solution. The role of urea is to disrupt the hydrogen bonding between kaolinite interlayers [169], [170], where mechanical vibration only shatters the platelets.

Urea delamination [148], [149] and dry grinding in a ball mill [150] are two methods to delaminate kaolinite. Tsunematsu *et al.* [150] conducted a series of delamination of kaolinite by using a ball mill, mechanical mortar and a combination of both devices, with and without urea. Their conclusion indicated that ball milling of the urea-kaolinite solution is an ineffective method for kaolinite intercalation. The mechanical grinding of kaolinite for a week at 45% humidity in the presence of a urea solution of 5, 10 and 30% wt. urea content was found to be more effective than grinding without urea. As a result of such a process, the specific areas of kaolinite were then increased from 20.8 to 34.4 and 36.5 m^2/g for grinding in 5, 10 and 30% wt. urea solutions respectively Another kaolinite grinding test was conducted by Tsunematsu et al. [151] in 30% wt. urea for two days at 95°C. The kaolinite urea colloid solution was brought to a boil and washed five times in water. The specific area of the processed kaolinite was increased from 10 to 116 m^2/g. The processed kaolinite platelets were thinner compared to the unprocessed kaolinite platelets.

To date, many grinding techniques have been used to delaminate kaolinite; however, these techniques tend to destroy the kaolinite nanosheets. The objective of this work is to develop a method that delaminates kaolinite while maintaining high surface area nanosheets.

3.2 Materials

Fluka Analytical grade kaolinite powder was purchased from Sigma Aldrich. Certified ACS urea pellets were obtained from Fisher Scientific. Four surfactants were mixed with kaolinite urea colloid. 99% purity Cetyltrimethylammonium bromide (CTAB) and PVP-10 $\left(M_{avg.} = 10000\ g/mol\right)$ were also bought from Sigma Aldrich. Acros Organic. Polyvinylpyrrolidone (PVP) K30 $\left(M_{avg.} = 111.14\ g/mol\right)$ was bought from Fisher Scientific. Alfa Aesar 99% purity sodium cholate (SC) was also bought from Fisher Scientific.

3.3 Equipment

An ultrasonicator from Fisher Scientific 550 Sonic Dismembrator was used to ultrasonicate the kaolinite urea colloid. Hermle Z400K Refrigerated Bench Top Centrifuge was used to separate the kaolinite from the urea solvent. SEM images were taken by Phenom Pro Desktop SEM (Nanoscience Instruments, Virginia) at accelerating voltages of 5 and 10 kV. XRD spectroscopy was done by Rigaku Ultima IV Diffractometer and scanning powder samples at $1°/min$ using CuK radiation (λ= 1.5418 A).

3.4 Procedure

All sample batches were composed of 0.7 g kaolinite in 50% wt. urea solution (near the solubility limit of urea) and ultrasonicated at 100% power, unless otherwise indicated. The urea solution was prepared by mixing 20g of urea with 20 mL of distilled water. The solubility data of urea in water was taken from the literature [171], [172]. The raw kaolinite was first mixed with 50 wt. %. urea and then agitated by a vortex spinner before undergoing ultrasonication. The kaolinite urea colloid was ultrasonicated for 30 mins under the following program: 10 s pulse and 1 min cooldown between each pulse. The reason for pulse ultrasonication instead of continuous ultrasonication is to prevent overheating of the ultrasonicator and sample solution. A sheet of parafilm was placed over the beaker in order to prevent water from evaporating from the urea solution (hence increasing urea concentration).

Post ultrasonication samples were completed and then decanted 5 times with 30 mL distilled water and isopropanol consecutively. The samples were mixed by a vortex mixer before centrifugation at 6000 rpm for 5 mins. After the decantation stage, the samples were poured into an alumina pan dish and left to dry for 24 hours in a fume hood.

Approximately 5 mL of ultrasonicated kaolinite colloid soaked in isopropyl alcohol was poured into a plastic dish and left to dry for 24 hours in a fume hood. The ultrasonicated kaolinite colloid sample was stored in isopropyl alcohol. The dried powders were collected and then characterized

by SEM. Statistical analysis of the SEM images was conducted using the ImageJ software. Platelet area less than 0.2 μm^2 were ignored, as these points in the SEM image were in the range of the background noise area. Areas greater than 706 μm^2 were considered to be agglomerates and not taken into account in the analysis.

Four experimental batches were conducted without the presence of any surfactants. Four ultrasonication powers were selected to study the effect of the ultrasonication power on kaolinite delamination. The selected ultrasonication intensities are 30 (345W), 40 (460W), 50 (575) and 100% (1150W) power respectively.

Experiments using the four surfactants CTAB, PVP (K30), PVP-10 and sodium cholate were performed to study the effect of surfactants on kaolinite delamination. The quantities of surfactant used are as follows: 0.2 g and 2 g of CTAB, 0.2 g and 13.3 g of PVP (K30), 0.2 g of PVP-10 and 8.6 g of sodium cholate. Selected surfactants were added near their water solubility limit (denoted as SL) to test kaolinite exfoliation near the solubility limit of urea and surfactant. 20, 13.3 and 8.6 g of CTAB [173], PVP (K30) [174] and sodium cholate [175] respectively were added to 20 mL of distilled water. The levels of 0.7g of kaolinite, 50% wt. urea concentration and 100% ultrasoniction power were still kept for the experiments with surfactants.

Runs were performed to determine if greater amounts of kaolinite can be delaminated using the same surfactant and urea concentrations. Three runs were performed using 5, 10 and 15 g of kaolinite. The three kaolinite batches were ultrasonicated in 50% wt. urea and 2 g of PVP-10 solution set at 100% power.

The content of kaolinite and surfactant as well as the ultrasonication power used in the tests are summarized in (Table 3.1) below:

Table 3.1: Batch conditions summary.

Kaolinite added (g)	**Surfactant added (g)***	**Ultrasonication power (%)**
0.7	None	30 (345W)
0.7	None	40 (460W)
0.7	None	50 (575W)
0.7	None	100 (1150W)
0.7	2 g CTAB	100 (1150W)
0.7	20 g CTAB	100 (1150W)
0.7	2 g PVP (K30)	100 (1150W)
0.7	13.3 g PVP (K30)	100 (1150W)
0.7	2 g PVP-10	100 (1150W)
0.7	8.61g sodium cholate	100 (1150W)
5	2 g PVP-10	100 (1150W)
10	2 g of PVP-10	100 (1150W)
15	2 g of PVP-10	100 (1150W)

*These quantities represent the amount of surfactant added to 20 grams of 50% wt. urea solution.

3.5 Results and Discussion

Two parameters were calculated in order to characterize the delaminated kaolinite; circular equivalent diameter (CED) and circularity. The CED based on area (Eq. 3.1) calculates the diameter x_A of the particle, assuming the sample particle is a perfect circle.

$$x_A = \sqrt{\frac{4A}{\pi}} \tag{3.1}$$

The CED based on the perimeter is $x_P = \frac{P}{\pi}$. Where A represents the sample area and P the perimeter.

The circularity is the degree to which a particle is similar to a circle. It is defined by (Eq. 3.2) according to ISO9276-6 on the descriptive and quantitative representation of particle shape and morphology. A circle has a circularity of 1 and a square a circularity of 0.886 indicating how the

observed samples are close to a perfect circle's orientation. The CED value is 1for perfect a circle, 0.605 for an equilateral triangle, 0.886 for a square, 0.907 for a hexagon.

$$C = \sqrt{\frac{4\pi A}{P^2}} \tag{3.2}$$

3.5.1 Raw kaolinite

Figure 3.1 shows the multiple layers of kaolinite powder assembled in a stack. An approximate spacing between each kaolinite layer is estimated to be between of 8.7 to 17.4 µm. Also, all of the kaolinite has a few small to submicron particle defects on the outer most layers (red circles in Figure 3.1). The role of the urea is to seep through the kaolinite interlayer spacing and disrupt the hydrogen bonding between the interlayers, and the kinetic energy to separate the layers is to be supplied by the ultrasonicator. The desired outcome is to sever the nanoplatelet stacks at their interlayers (yellow arrow in Figure 3.1) and obtain an isolated kaolinite nanosheet.

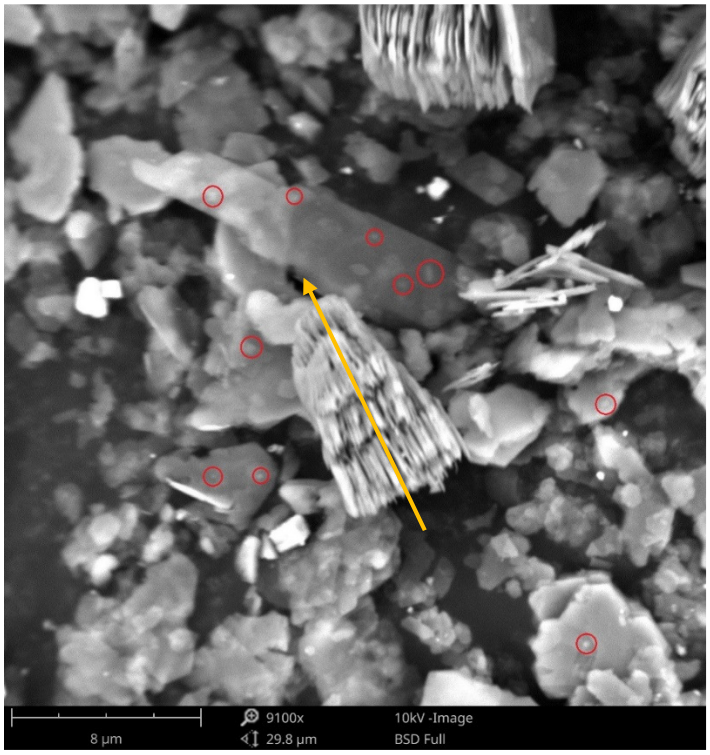

Figure 3.1: Fresh kaolinite. Each kaolinite powder consists of tightly packed interlayers held by hydrogen bonding. The scale bar is 8 µm.

A second SEM image of raw kaolinite is shown in Figure 3.2. The platelets in Figure 3.2 are less aggregated and have increased separation distance between individual platelets layers. The statistical analysis and data calculation from Figure 3.2 listed in Table 3.2 will be identified as "untreated kaolinite" and will form a basis to compare future samples.

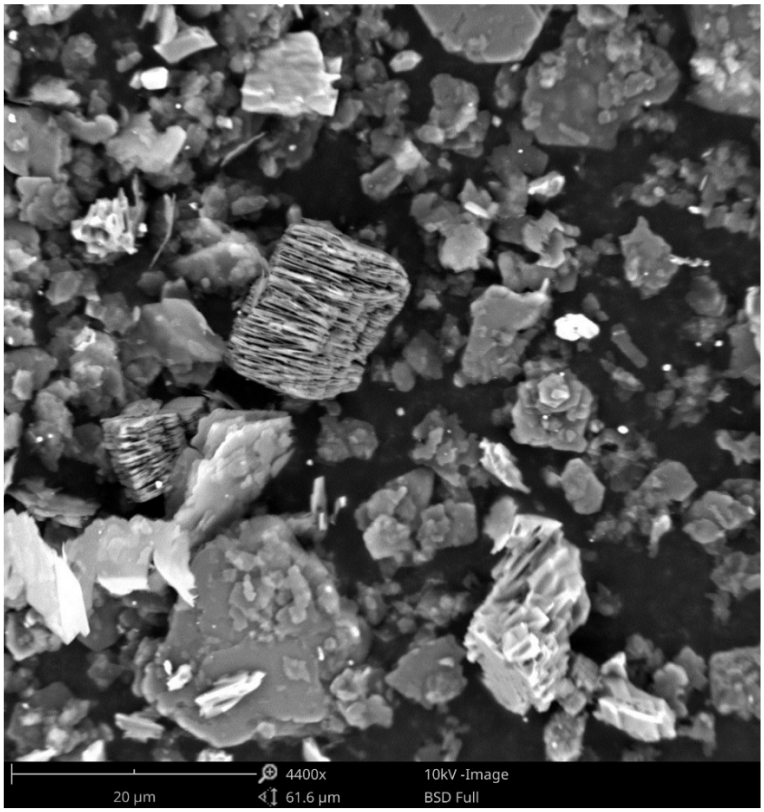

Figure 3.2: The platelets are less aggregated and farther separated. The white scale bar is 20 µm.

Table 3.2: Figure 3.2 statistical summary

Criteria	Area (μm^2)	Perimeter (μm)
Mean	4.53	14.7
SD	14.22	22.8
Min	0.20	2.0
Max	152.0	203

3.5.2 The role of ultrasonication

Ultrasonication and its intensity play a critical role in kaolinite delamination. Operating at higher intensities during the ultrasonication stage results in thinner layers of kaolinite and more fragmented flakes. Sufficient kinetic energy is needed to break the hydrogen bonds joining the kaolinite platelets.

In Figure 3.3, Figure 3.4, Figure 3.5 and Figure 3.6 shows a collection of SEM images of ultrasonicated kaolinite in 50% wt. urea solution at 30, 40, 50 and 100% power, respectively. Multilayer kaolinite is observed in Figure 3.3, Figure 3.4, Figure 3.5 and no multilayer kaolinite is observed in Figure 3.6. Without the ultrasonication step, kaolinite has an average circularity of 0.51. With sonication the average circularities are 0.63, 0.66, 0.7, 0.67 for 30, 40, 50 and 100 % ultrasonication power. This indicates that sonication reduced the elongation of the particles making them closer to squares. At a higher ultrasonication power the platelets were more fragmented as the distribution of the CED and circularity was broadened compared to non sonicated particles as seen in Figure 3.7, Figure 3.8 and Figure 3.9. In Table 3.3, the average perimeter decreases when operating at a higher ultrasonication intensity. Kaolinite is the least delaminated in Figure 3.3 because a large stacked kaolinite layer is observed in the middle of the image in Figure 3.3. It is shown from Figure 3.7 that the ultrasonicated kaolinite has a higher share of CED distribution above 3 µm.

The circularity is mostly distributed on the left side in Figure 3.9 for untreated kaolinite and the 30% ultrasonication power batch. In direct contrast, kaolinite is more circular (shift right) when the ultrasonication power is operating at the maximum power (100%). This result is shown in Figure 3.8 since there is no multilayers kaolinite observed (Figure 3.6).

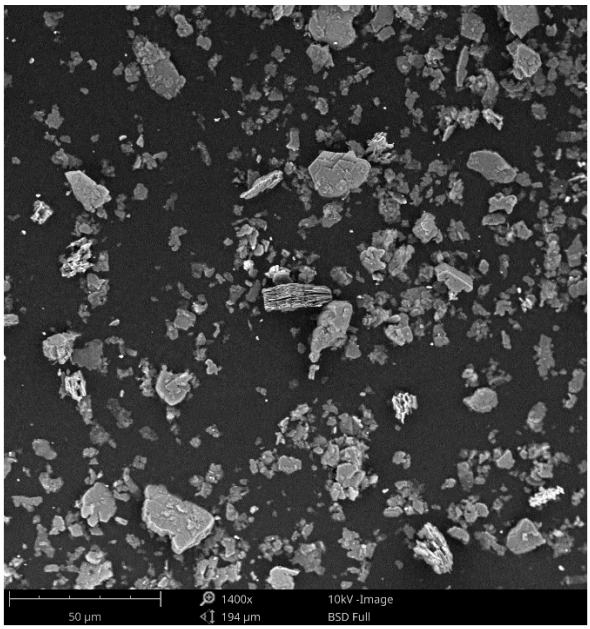

Figure 3.3: 0.7 g of kaolinite ultrasonication at 30% power in 50% wt. urea solution. Multiply large infoliated kaolinite layers are present. The scale bar is 50 µm.

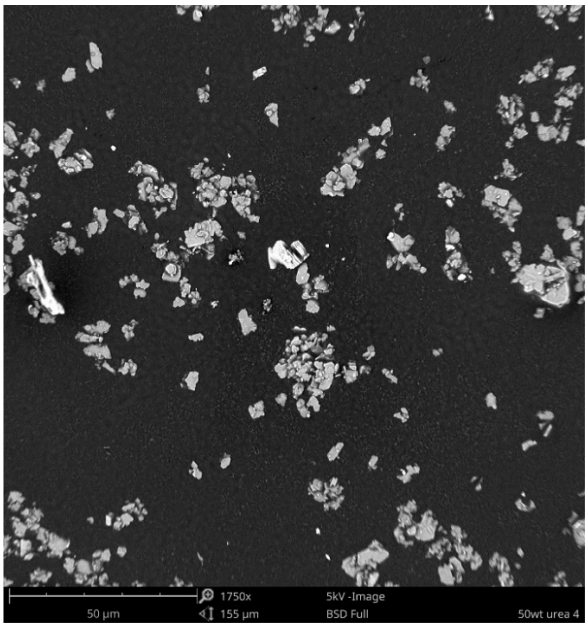

Figure 3.4: 0.7 g of kaolinite ultrasonication at 40% power in 50% wt. urea solution. Lots of large infoliated kaolinite are present. The smaller platelets are on top of the larger platelet. The scale bar is 50 µm.

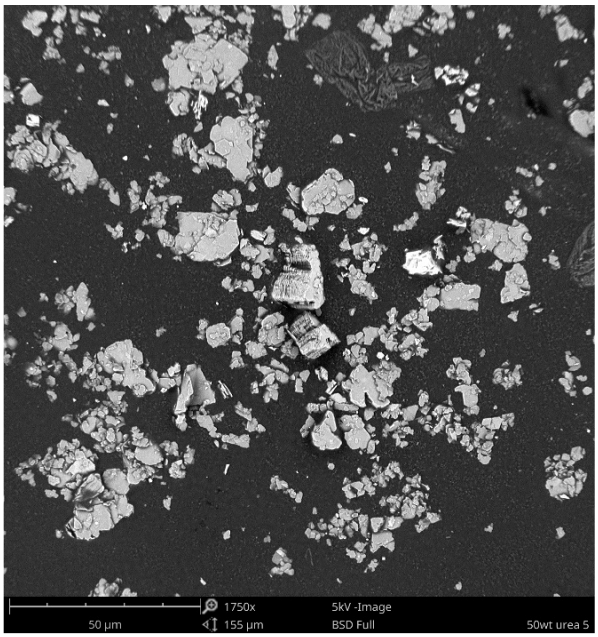

Figure 3.5: 0.7 g of kaolinite ultrasonication at 50% power in 50% wt. urea solution. Two large delaminated kaolinite are spotted. The scale bar is 50 µm.

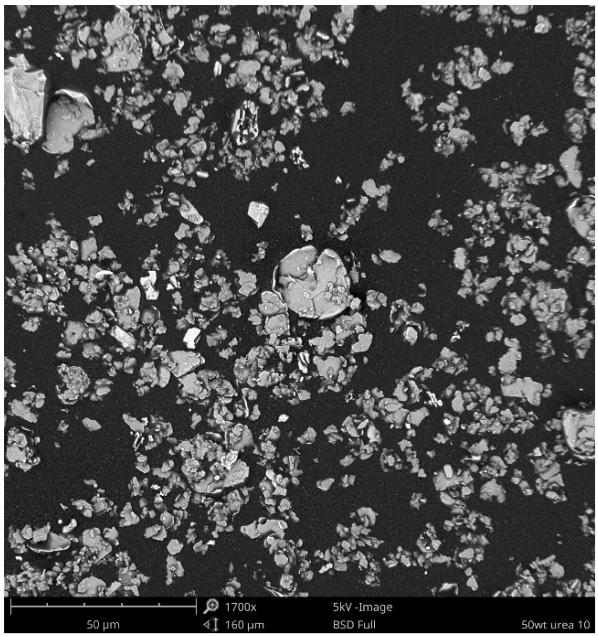

Figure 3.6: 0.7 g of kaolinite ultrasonication at 100% power in 50% wt. urea solution. A shattered dish like platelet is spotted at the center and upper left corner. The scale bar is 50 µm.

Table 3.3: No surfactant statistical summary

	30% power		**40% power**		**50% power**		**100% power**	
Criteria	Area (μm^2)	Perimeter (μm)	Area (μm^2)	Perimeter (μm)	Area (μm^2)	Perimeter (μm)	Area (μm^2)	Perimeter (μm)
Mean	10.488	18.293	7.14	14.262	10.068	16.059	5.81	12.73
SD	28.318	26.418	13.465	18.085	27.402	26.816	15.17	17.521
Min	0.203	1.758	0.204	1.666	0.204	1.73	0.204	1.714
Max	336.29	255.04	129.22	180.214	269.13	238.05	320.24	236.92

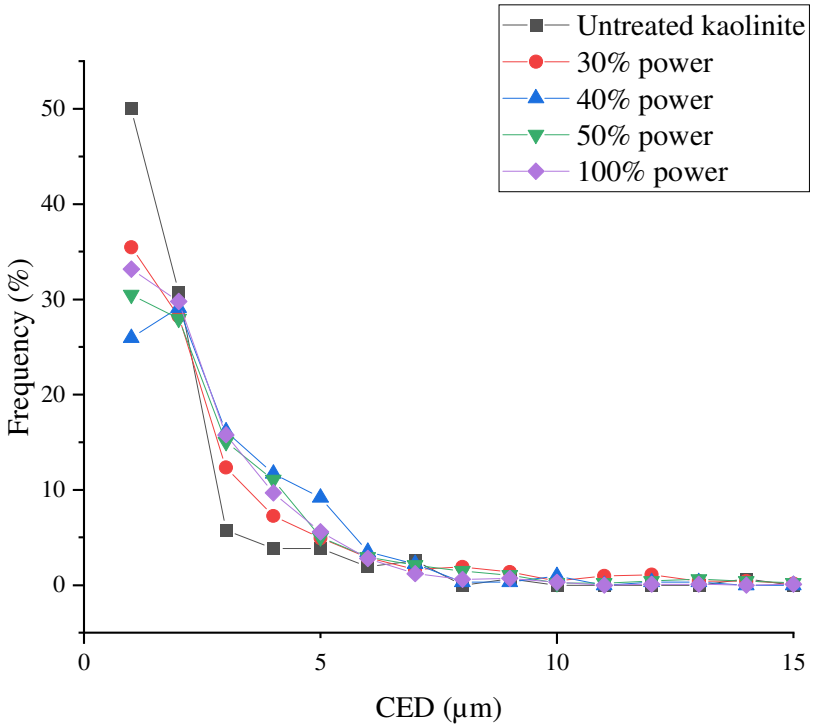

Figure 3.7: No surfactant circular equivalent diameter (CED) distribution based on area

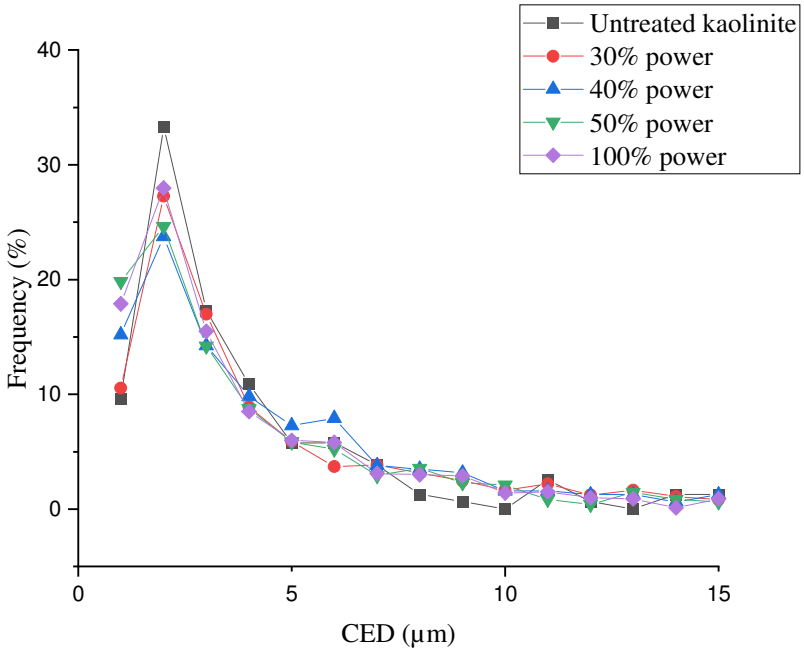

Figure 3.8: No surfactant circular equivalent diameter (CED) distribution based on perimeter

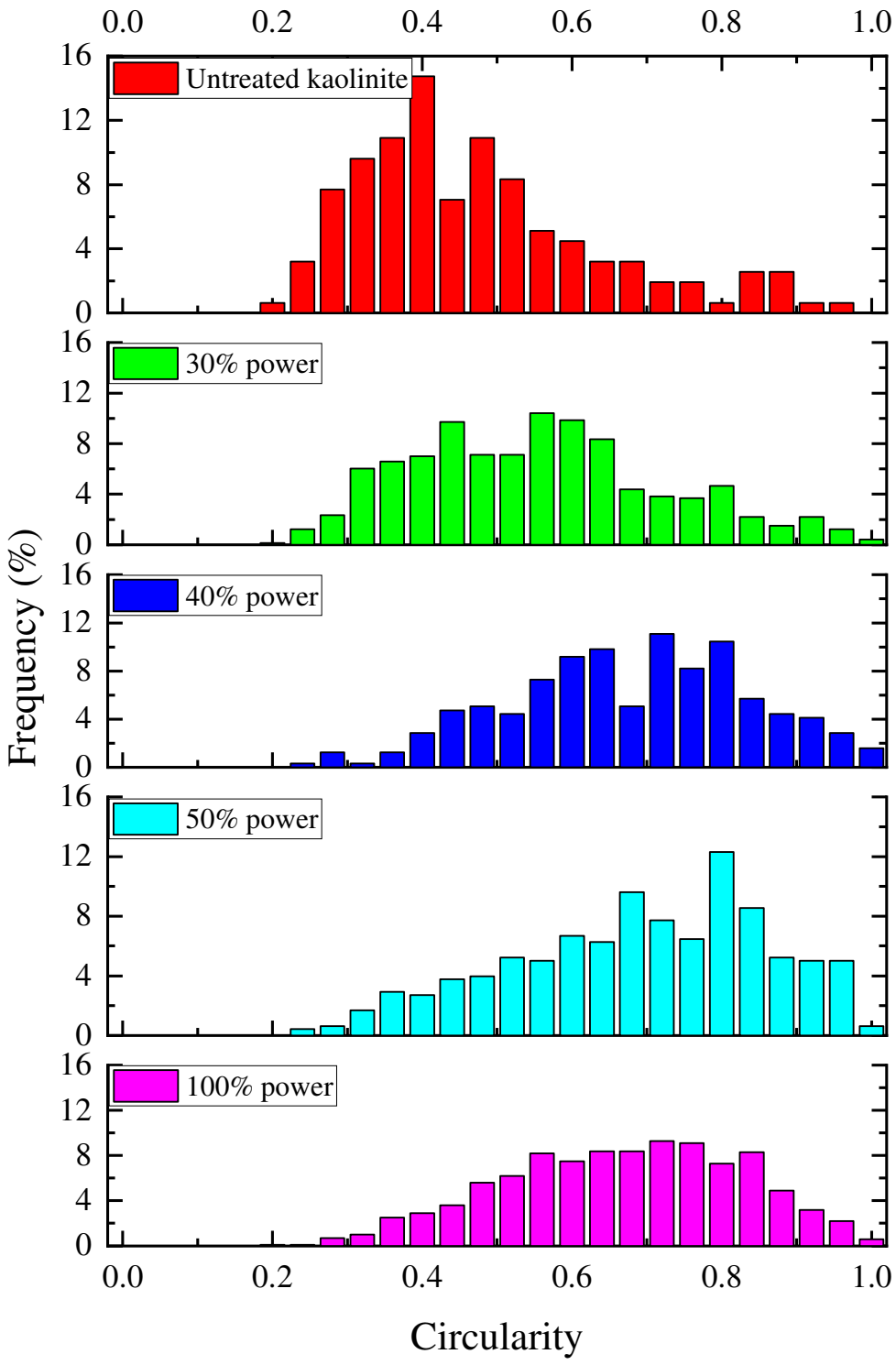

Figure 3.9: No surfactant circularity distribution

3.5.3 The effect of surfactants

The presence of a surfactant has positive effects on kaolinite delamination. Processing without the use of surfactants results in kaolinite particles having sharp edges resembling broken glass fragments. The role a surfactant is to prevent the delaminated kaolinite layers from recombining into large aggregates due to the strong hydrogen bonding between the kaolinite interlayers [176].

Four surfactants were studied; CTAB, PVP (K30), PVP-10, and sodium cholate. Selected surfactants were added at their water solubility limit in water as shown in Table 3.1 above.

3.5.3.1 CTAB

The results of ultrasonicating 2 g of CTAB mixed with 50% wt. urea solution for 30 min is shown in Figure 3.10. The kaolinite powder is converted into a bowl-shaped sheet with the kaolinite platelets exposed instead of being stacked on top of each other. Figure 3.10 reveals that there are many kaolinite "bowls" shaped micro-structures in its early stages. Some of the kaolinite layers are still not completely delaminated but rather semi-delaminated. Other kaolinite sheets were also present. These micron-sheets have semi-round edges, as this is in direct contrast with the unprocessed kaolinite powder (Figure 3.1), where all the kaolinite layers are stacked on top of each other. Using ImageJ, 259 particles were used to determine the average area and perimeter. These were $18.8\ \mu m^2$ and $27.0\ \mu m$ respectively. The minimum, the maximum areas and perimeters were $0.201\ \mu m^2$, $381.4\ \mu m^2$, $1.6\ \mu m$ and $390.1\ \mu m$ respectively. In Figure 3.16 below, this treatment follows the same trend as all the other surfactants with the overwhelming majority of CEDs measuring at 1 µm. According to Figure 3.16, the 2 g CTAB experiment has the broadest distribution range for the circularity. The higher standard deviation value for this treatment in Table 3.4 is that some of the delaminated kaolinite layers were overlapped in Figure 3.10, as overlapping layers give a false area and perimeter reading in separated individual delaminated kaolinite layers.

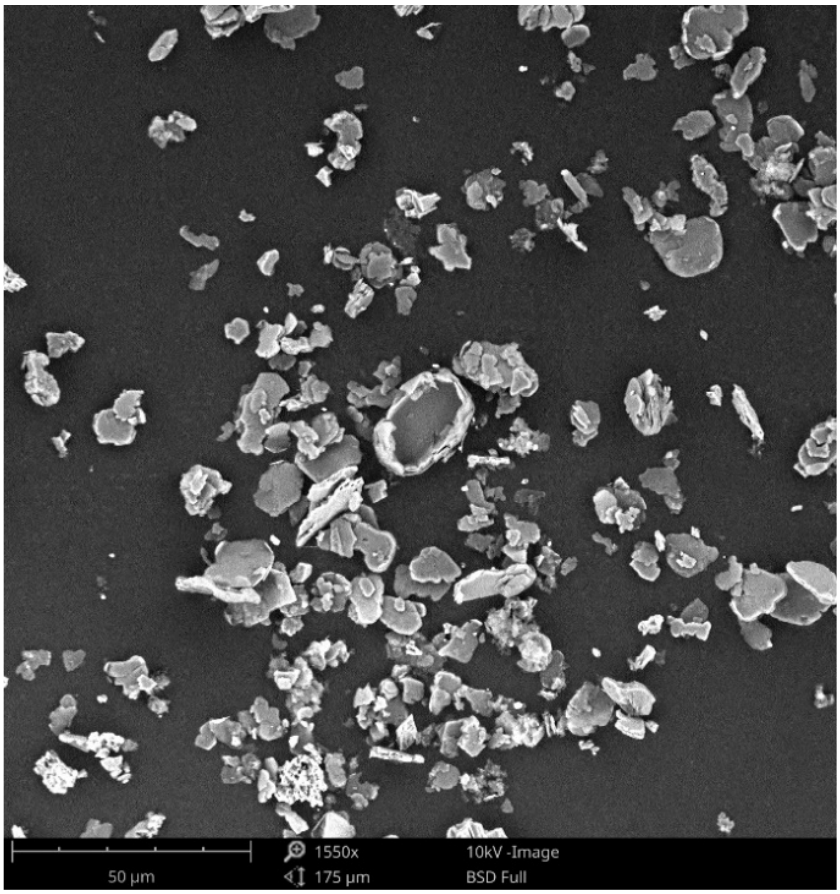

Figure 3.10: An SEM micrograph of delaminated kaolinite with 2 g of CTAB in 50% wt. urea solution ultrasonicated for 30 mins. The scale bar is 50 µm.

Figure 3.11, is an SEM of kaolinite delaminated at the solubility limit of CTAB [177]–[180]. The kaolinite interlayers are separated, and each of the kaolinite layers aggregates to form a "bowl" shape micro-structure is shown in Figure 3.9. It shows that more single layers of kaolinite are produced compared to the multilayers produced at the 2 g CTAB level shown in Figure 3.10. Each individual delaminated layer is also further separated, a possible explanation is that a higher CTAB concentration prevents the aggregation of delaminated kaolinite nanoplatelets. Also, kaolinite delaminated at a higher CTAB concentration has a smoother surface and fewer smaller particles are generated compared to those obtained at lower 2g CTAB concentration. A total of 37 samples were used to carry out the statistical analysis. From Table 3.4, the average area and perimeter were 35.4 μm^2 and 28.8 µm, respectively. The overlapping layers contribute to a moderate standard deviation. The minimum, the maximum areas and perimeters were measured to 0.34 μm^2, 198.0 μm^2, 3.2 µm and 116.3 µm, respectively. From Figure 3.16, when CTAB is added at the

solubility limit (20 g of CTAB in 20 mL of distilled water), it is the only run that does not follow CED distribution trend of other surfactants. It has the smallest fraction of 1 µm CED and has local maxima at 7 and 11 µm. Figure 3.18 shows the circularity results of all the kaolinite ultrasonicated with a surfactant present. Out of all the surfactant runs, the 20 g CTAB batch has the narrowest circularity distribution as seen in Figure 3.18 below. The highest bar located at 0.7 indicates that most platelets have a square like orientation.

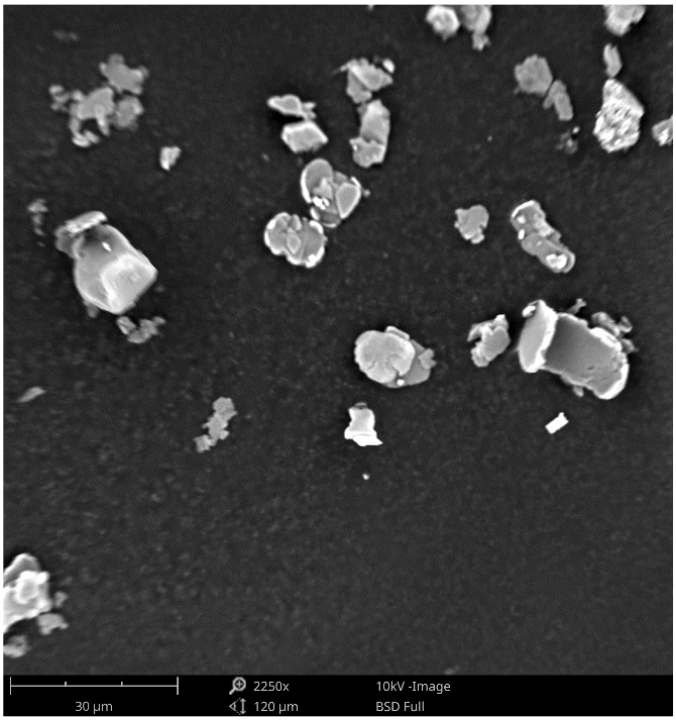

Figure 3.11: SEM micrograph of delaminated kaolinite with 20 g of CTAB in 50% wt. urea solution ultrasonicated for 30 mins. Most of the kaolinite interlayers are entirely delaminated and separated. The white scale bar is 30 µm.

Table 3.4: CTAB surfactant statistical summary

	2 g CTAB		**20 g CTAB**	
Criteria	Area (μm^2)	Perimeter (μm)	Area (μm^2)	Perimeter (μm)
Mean	18.82	27.03	35.383	28.798
SD	45.925	45.503	48.966	29.132
Min	0.201	1.657	0.344	3.191
Max	381.44	390.10	198.05	116.34

3.6.3.2 PVP (K30)

The results of delaminating kaolinite using 2 g of PVP K30 surfactant in a 50% urea solution is displayed in Figure 3.12. The kaolinite nanosheet edges are sharper compared to the CTAB batch. A large multilayer nanosheet with a miniature folded nanosheet is found at the center of this image. Utilizing PVP as a surfactant produces sharper vertices vs. CTAB. Another critical difference further demonstrates that if the same amount of surfactant were used, then ultrasonicating using PVP (K30) surfactant results in more single layers, and there are fewer fine particles that have remained on the delaminated layer. A particular aggregation of the delaminated kaolinite sheets can be observed in the center and at the upper left corner. From Table 3.5, the average area and perimeter were $24.0\,\mu m^2$ and $35.4\,\mu m$ respectively. The minimum, maximum areas and perimeters were $0.21\,\mu m^2$, $461.8\,\mu m^2$, $2.0\,\mu m$ and $355.3\,\mu m$ respectively. Some of the overlapping delaminated kaolinite contributes towards a higher standard deviation value.

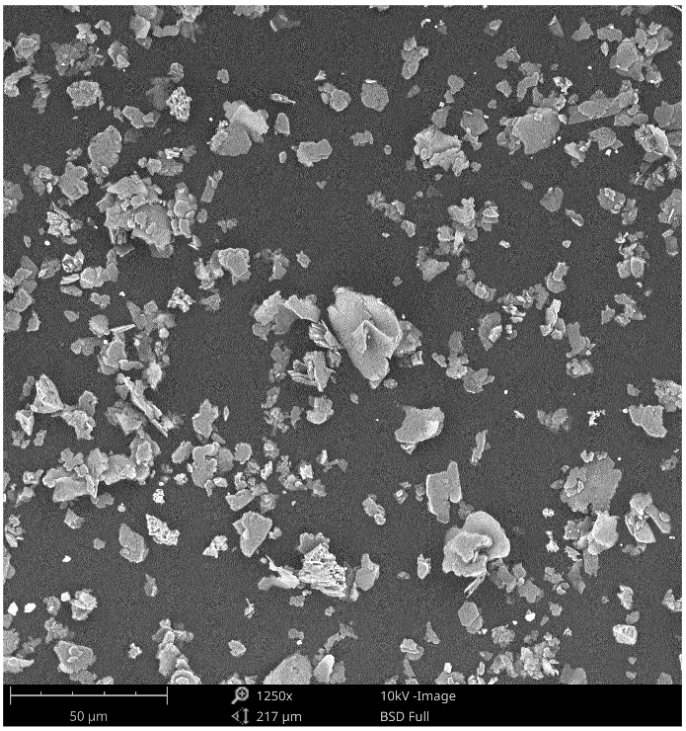

Figure 3.12: SEM micrograph of kaolinite ultrasonicated with 2 g of PVP (K30) in 50% wt. urea solution for 30 mins. The scale bar is 50 µm.

Kaolinite powder delaminated at the PVP (K30) solubility limit [174] (Figure 3.13) shows different results compared to Figure 3.12. In Figure 3.13, smaller sheets are deposited on the top of a larger kaolinite sheet. Sharp flake like shape platelets, are also observed as indicated by the green circles. Ultrasonicating at the solubility limit of PVP (K30) leads to different results compared to the original 2 g of PVP (K30). Figure 3.13 shows that the nanosheet edges are more jagged compared to Figure 3.12. The degree of aggregation also dropped, as this is expected when surfactant concentration is increased. The area and perimeter of 466 samples were studied using ImageJ and the results are listed in Table 3.5. The average area and perimeter are 28.2 μm^2 and 35.9 µm, respectively. The minimum, the maximum areas and perimeters were 0.2 μm^2, 627.8 μm^2, 2.1 μm and 418.1 μm respectively.

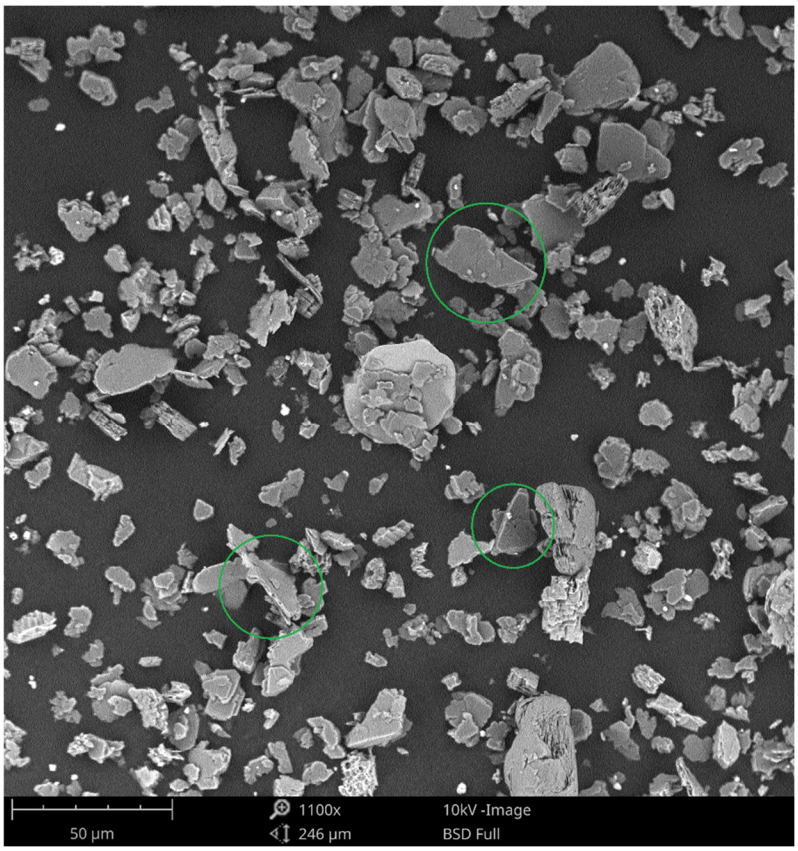

Figure 3.13: The raw kaolinite has been delaminated into single or few layers sheet using 13.3 g of PVP (K30) in 50% wt. urea solution for 30mins. The nanosheets have jagged but no sharpened edges. The green circles are “flint” like platelets. The white scale bar is 50 µm.

The CED distribution in Figure 3.16 for both 2 g and 13.3 g PVP (K30) have miniscule difference at the initial starting point. The higher PVP (K30) concentration has much higher frequency percentage for the 1 to 2 µm peaks. The circularity distribution for both 2 g and 13.3 g of PVP (K30) batch in Figure 3.18 is almost identical with the 13.3 g run being slightly narrower.

Table 3.5: PVP (K30) surfactant statistical summary

	2 g PVP K30		**13.3 g PVP K30**	
Criteria	Area (μm^2)	Perimeter (μm)	Area (μm^2)	Perimeter (μm)
Mean	24.037	35.454	28.277	35.879
SD	58.016	52.939	65.64	60.28
Min	0.21	1.993	0.214	2.098
Max	461.81	355.338	627.847	418.067

3.6.3.3 PVP-10

The results of delaminating 13.3 g of PVP-10 in 50% wt. urea solutions are shown in Figure 3.14. The edges and vertices of the delaminated kaolinite flakes in Figure 3.14 are smoother compared to those using the same amount of mass basis PVP (K30) shown in Figure 3.12. The resulting circularity distribution is similar to the 2 g CTAB batch in Figure 3.10. The delaminated kaolinite flakes observed in Figure 3.14 are scattered but not aggregated; however, the appearance of multilayer or semi delaminated kaolinite and the small white particles are more numerous compared to the same amount of PVP (K30) in Figure 3.12.

The area and perimeter of 424 samples were chosen to perform statistical analysis and listed in Table 3.6. The average area and perimeter are 11.2 μm^2 and 15.5 µm respectively. The small particles on the top of the main platelets increase the standard deviation. The minimum, the maximum areas and perimeters were estimated as 0.2 μm^2, 465.5 μm^2, 1.6 μm and 199.5 μm respectively. Comparing Figure 3.13 to Figure 3.14 it can be see that the higher molecular weight PVP K30 did not penetrate between the kaolinite nanoplatelets and properly delaminate the kaolinite. The PVP 10 platelets are not shattered like he PVP K30 platelets and have a thin disk like appearance. In Figure 3.16, 2 g PVP-10 batch has the highest ultrasonicated kaolinite 2 µm

peak out of the surfactant set. This 0.2 g PVP-10 batch has second narrowest circularity distribution after the 20 g CTAB batch, however, this PVP-10 batch has smoother and continuous distribution.

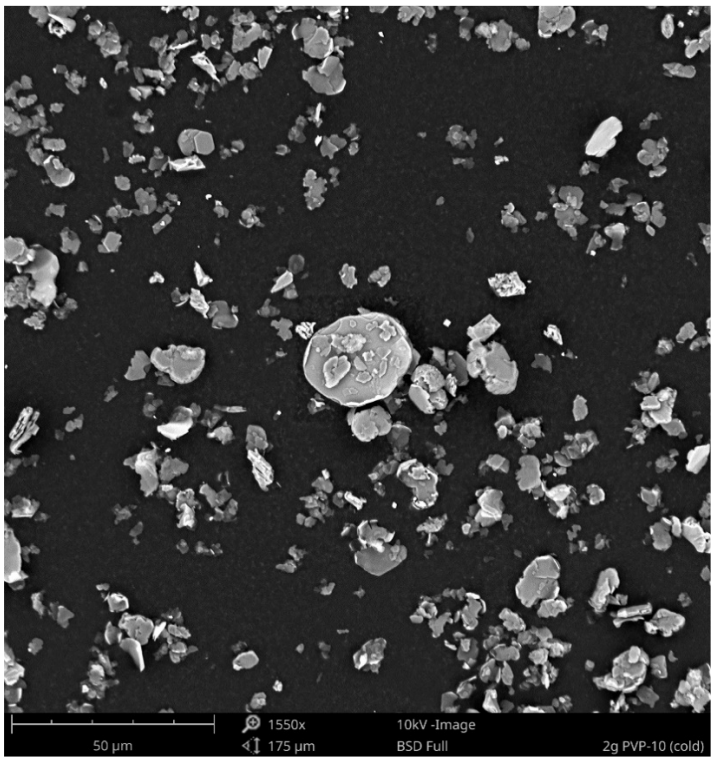

Figure 3.14: Kaolinite ultrasonicated using 2 g of PVP-10 in 50% wt. urea solution for 30 mins. Multiple circular kaolinite platelets have multi-layers. The edges are less sharp compared to using PVP-10. The white scale bar is 50 µm.

Table 3.6: PVP-10 surfactant statistical summary

Criteria	Area (μm^2)	Perimeter (μm)
Mean	11.19	15.46
SD	30.292	19.552
Min	0.201	1.616
Max	465.484	199.649

3.6.3.4 Sodium cholate

Sodium cholate is a positively charged surfactant. It was added near its solubility limit (0.02 M) [181] in 50% wt. urea solution. The delaminated kaolinite layers are clearly seen in Figure 3.15. They are similar to those in Figure 3.10 and Figure 3.14, as many platelets have smooth edges and circular geometric orientation. However, there are more miniature particles present on the delaminated kaolinite platelets. A sample size of 541 was selected to perform statistical analysis. From Table 3.7, the average area and perimeter were $23.0\ \mu m^2$ and 32.9 µm. The minimum, maximum areas and perimeters were 0.21, $408.6\ \mu m^2$, $1.8\ \mu m$ and $357.0\ \mu m$ respectively summarized in Figure 3.7. Overlapping of kaolinite layers and the small particles contributes towards standard deviation. The CED distribution presented in Figure 3.16 follows the same trend as other surfactant. The circularity distribution of 8.611 g SC in Figure 3.18 is very similar to the untreated kaolinite, thus proving that sodium cholate is not an effective surfactant for altering geometric orientation.

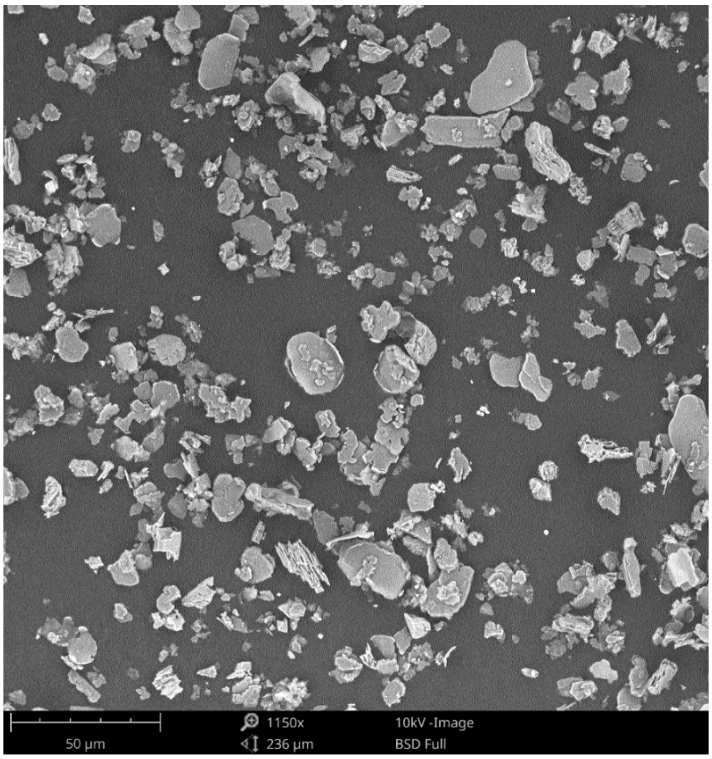

Figure 3.15: Kaolinite exfoliation using 8.611g sodium cholate in 50% wt. urea solution for 30 mins. A few dish-like objects along with multiple kaolinite nanosheets. The nanosheets have round edges. The white scale bar is 50 µm.

Table 3.7: Sodium cholate surfactant statistical summary

Criteria	Area (μm^2)	Perimeter (μm)
Mean	23.023	32.916
SD	52.092	48.753
Min	0.209	1.748
Max	408.639	357.036

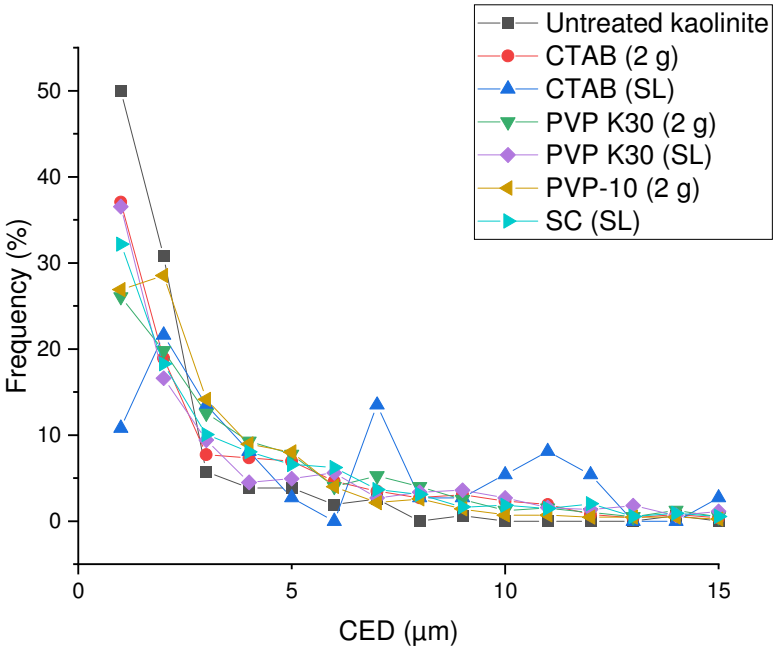

Figure 3.16: Surfactant CED distribution based on area.

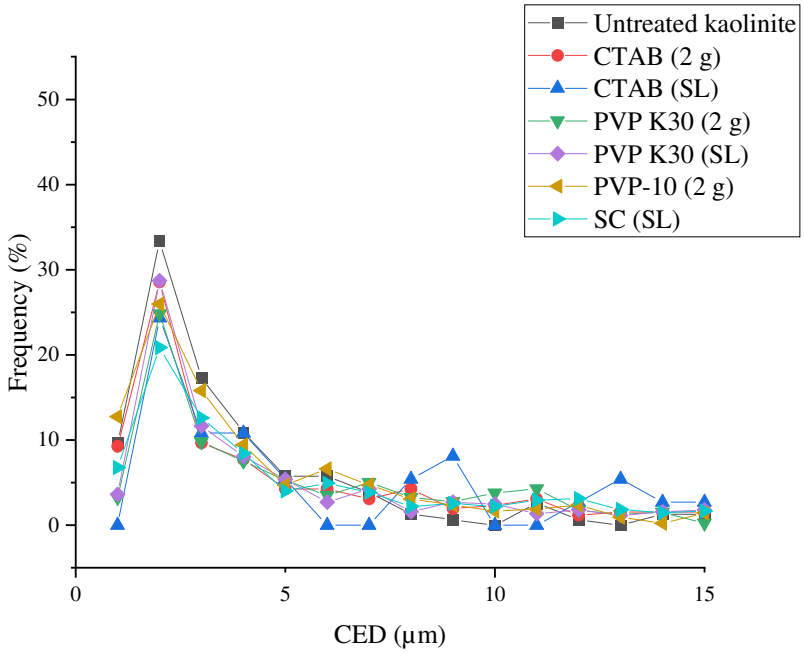

Figure 3.17: Surfactant CED distribution based on perimeter

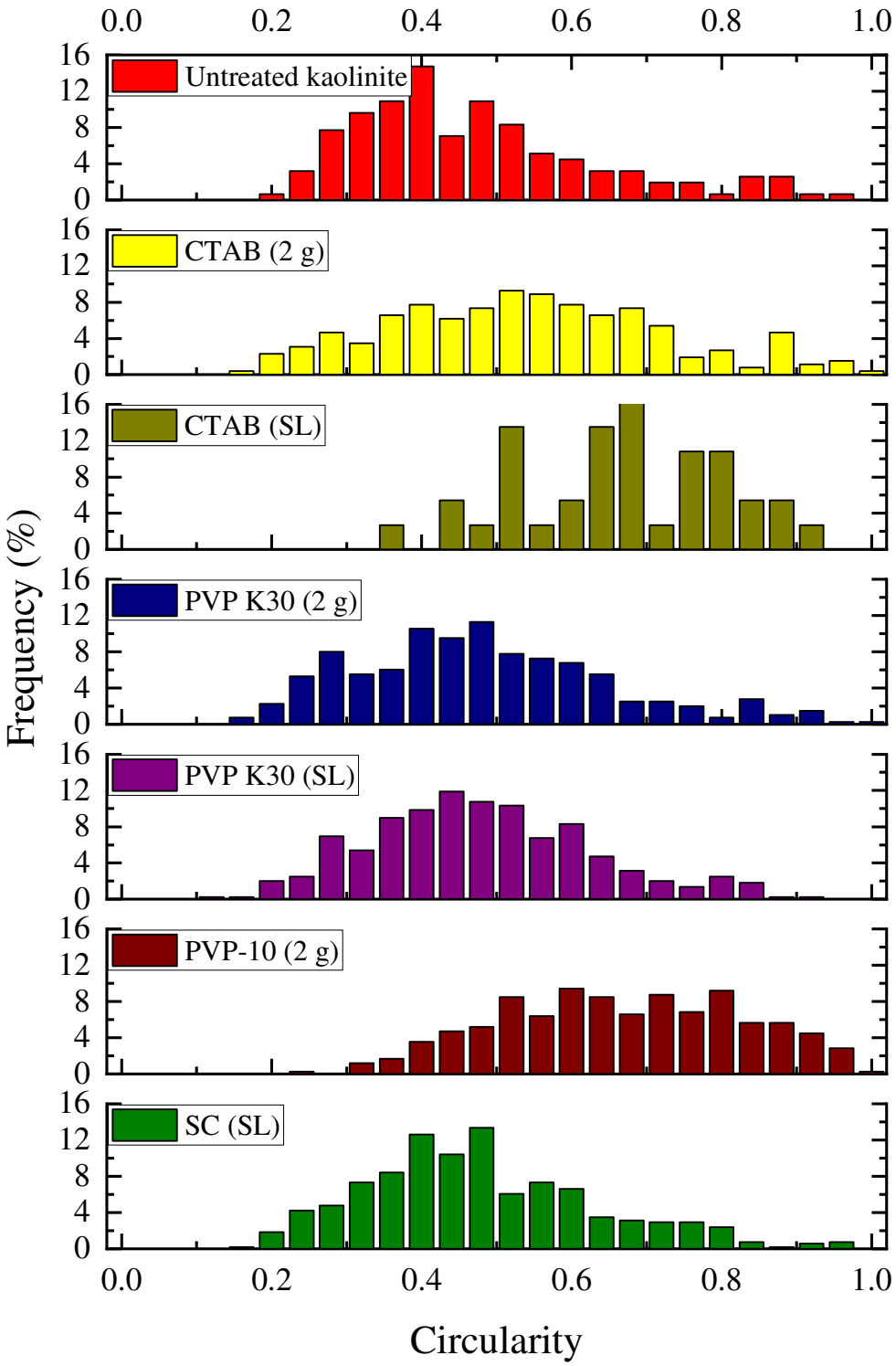

Figure 3.18: Surfactant circularity distribution

3.6.3.5 Increasing the amount of kaolinite in the sonication mixture

The SEM image of 5 g of kaolinite added into 2 g PVP-10 in 50% wt. urea solution and ultrasonicated for 30 mins are shown in Figure 3.19. The statistical results are summarized in Table 3.8. The dish-shaped orientation with circular vertices are the most common platelets found along with delaminated platelets indicated by the red circles in Figure 3.19, and a square-like "dish" platelet is also found as indicated by the green circle. The degree of aggregation of the delaminated kaolinite is slightly higher compared to the original fresh kaolinite (Figure 3.1). A sample size of 360 was selected, and from Table 3.8, the average area and perimeter were 15.8 μm^2 and 19.6 µm respectively. The minimum, maximum areas and perimeters were 0.2 μm^2, 392.4 μm^2, 1.7 µm and 347.7 µm respectively.

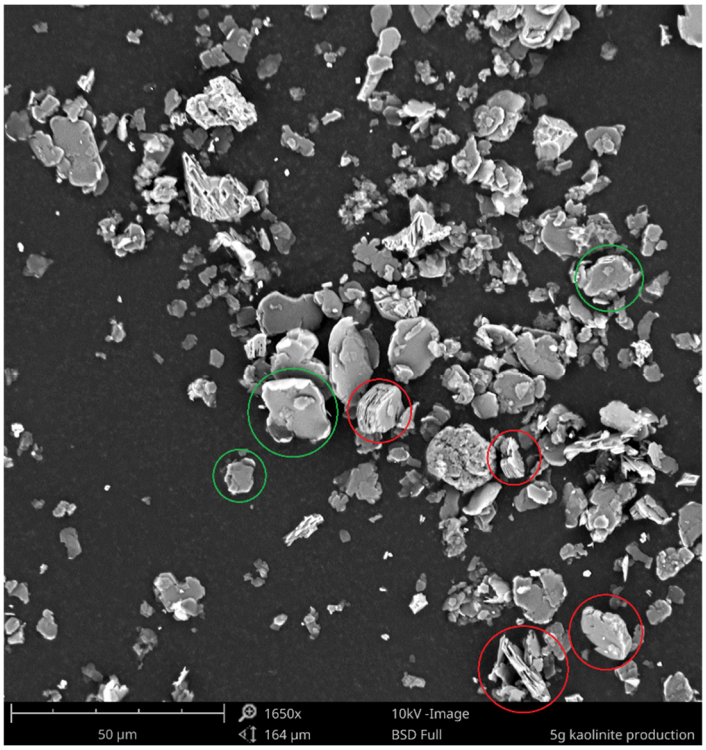

Figure 3.19: 5 g of kaolinite ultrasonicated in 5 g of PVP-10 in 50% wt. urea solution for 30 mins. The green circle is a square-like "dish" platelet. The red circles are delaminated kaolinite. The white scale bar is 50 µm.

The result of ultrasonicating 10 g of kaolinite for 30 mins with 2 g of PVP-10 in 50% wt. urea is shown in the Figure 3.20. The degree of aggregation is much higher in Figure 3.20 compared to

the 5 g kaolinite ultrasonication run (Figure 3.19) and raw kaolinite (Figure 3.1 and Figure 3.2). It is interesting to note that the there are more single layer kaolinite platelets present when adding 10 g of kaolinite rather than 0.7 and 5 g of kaolinite ultrasonicated. A sample size of 408 chosen to perform analysis statically is listed in Table 3.8, the average area and perimeter were 11.085 μm^2 and 20.962 µm respectively. The minimum, maximum areas and perimeters were 0.203 μm^2, 398.797 μm^2, 1.621 µm and 661.371 µm respectively.

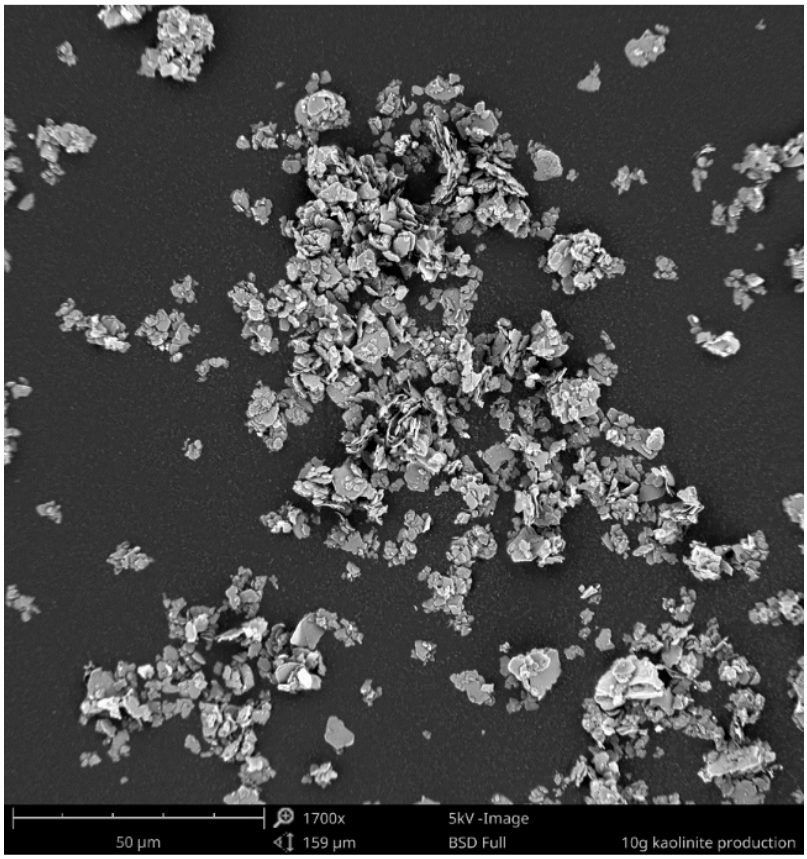

Figure 3.20: 10 g of kaolinite ultrasonicated with 2 g of PVP-10 in 50% wt. urea solution for 30mins. A large cluster of the aggregated delaminated plate is observed. The white scale bar is 50µm.

The results for the sonication of 15 g of kaolinite for 30 mins with 2 g of PVP-10 in 50% wt. urea solution are shown in Figure 3.21. Large aggregates of platelet clusters with smaller kaolinite flakes on top are found in Figure 3.21. An exciting feature is that three of the aggregate cluster platelets have cracks on the large sheet as indicated by the green circles. Figure 3.14 and Figure 3.21 where 2 g and 5 g of PVP-10 are used in the sonication batch gave delaminated nanoplatelets

whereas increasing the weight to 10 g and 15 g produced particulates with sharper edges having an aspect ratio closer to a square. The sample size was 316 in order to perform statistical analysis listed in Table 3.8, and the average area and perimeter were 10.1 μm^2 and 15.5 µm. The minimum, maximum areas and perimeters were 0.2 μm^2, 372.7 μm^2, 1.7 µm and 304.9 µm respectively.

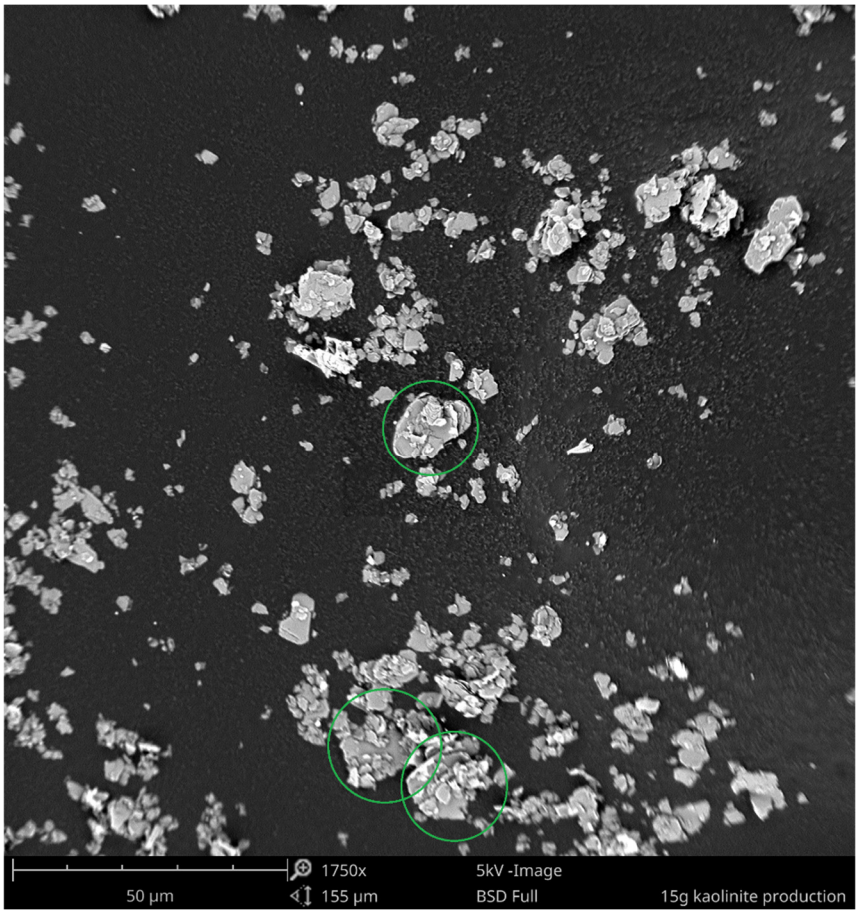

Figure 3.21: 15 g of kaolinite ultrasonicated with 2 g of PVP-10 in 50% wt. urea solution for 30 mins. The green circles are example of shatter disk like platelets. The white scale bar is 50 µm.

Table 3.8: Increased kaolinite statistical analysis summary

	5 g kaolinite		10 g kaolinite		15 g kaolinite	
Criteria	Area (μm^2)	Perimeter (μm)	Area (μm^2)	Perimeter (μm)	Area (μm^2)	Perimeter (μm)
Mean	15.852	19.641	11.085	20.962	10.129	15.549
SD	40.674	33.126	30.391	48.4	28.238	27.433
Min	0.203	1.697	0.203	1.621	0.204	1.711
Max	392.431	347.728	398.797	661.371	372.764	304.939

The distributions for the CEDs and circularity are shown Figure 3.21, Figure 3.22 and Figure 3.24 for 5, 10 and 15 g of kaolinite. The CED distribution of 5 g kaolinite slightly shifted right with lower than 2 µm CED being the dominating particle. The circularity is shifted to the right compared to the untreated kaolinite.

The CED distribution of the 10 g kaolinite follows the same trend as the previous batch (5 g kaolinite) increased kaolinite batch with a slight difference in sub 2 µm distribution as shown in Figure 3.21 and Figure 3.22. In Figure 3.24, the 10 g kaolinite batch shape distribution is broader compared to raw kaolinite and 5 g kaolinite batch. The aggregation and overlapping of miniature platelets along with background noise contributes towards standard deviation.

The CED and circularity distribution for 15 g are show in Figure 3.21, Figure 3.22 and Figure 3.24 respectively. From Figure 3.21 and Figure 3.22, this batch (15 g kaolinite) has the highest 2 µm peak for the CED distribution. The average circularity of the 15 g batch was 0.7 with many of the particles having the circularity of a square (0.886). The increased amount of kaolinite in the sonicating mixture lead to the breakup of the nanoplatelets. This indicates that there is an upper limit to the load of kaolinite that can be present in the sonication batch for a successful delamination.

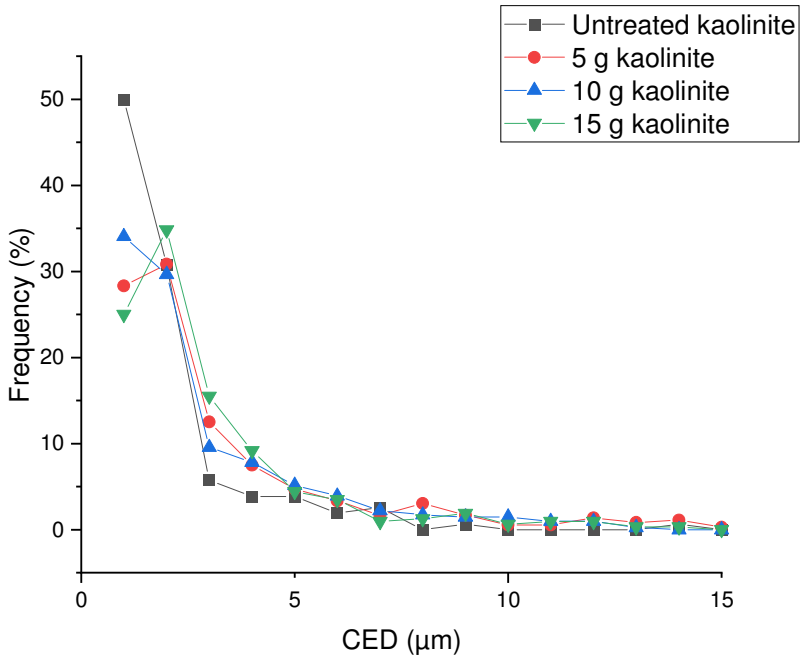

Figure 3.22: Increased kaolinite CED distribution based on area

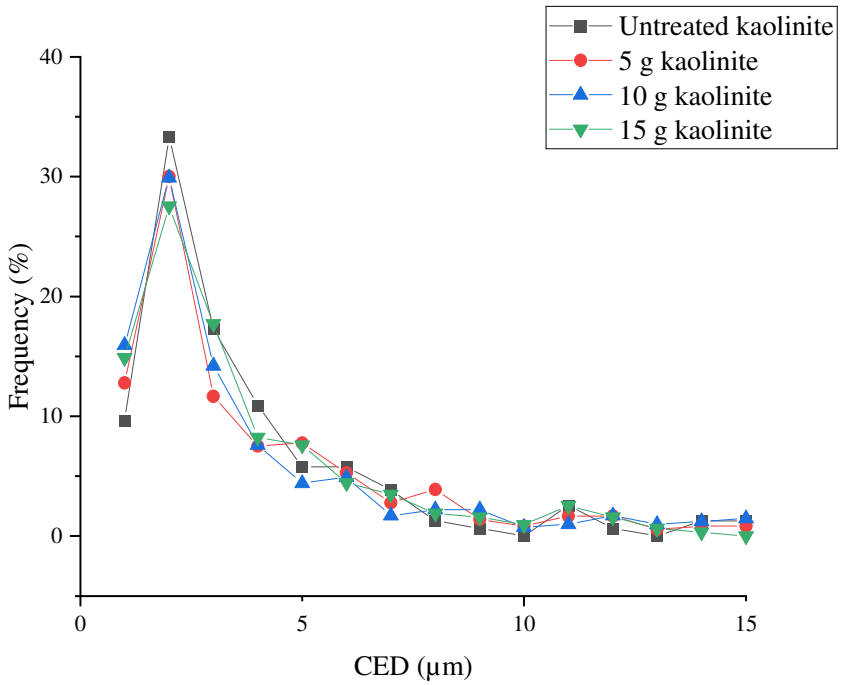

Figure 3.23: Increased kaolinite CED distribution based on perimeter

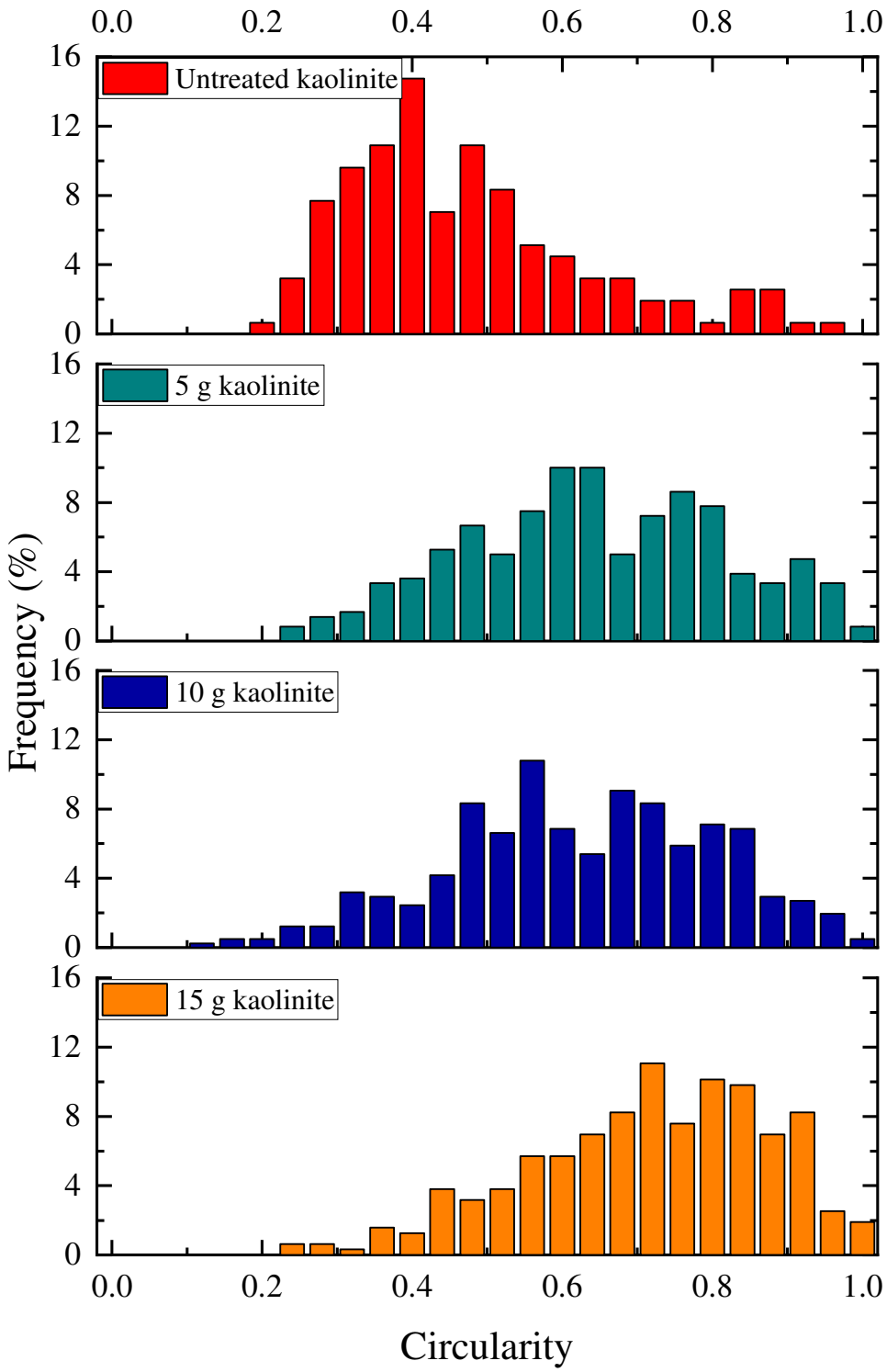

Figure 3.24: Kaolinite circularity distribution

3.6 Discussion summary

Increasing sonication power in the absence of surfactants creates a greater number of particles between 3 and 6 μm due to the fracture of larger particles. From the CED based on perimeter the number of 1 μm particles increases with sonication power. The circularity of the particles changes from thin rectangles to squares as the sonication power increases.

When CTAB is used at its solubility limit with urea, the kaolinite interlayers are separated to form nanosheets in the shape of a "bowl". More single layers of kaolinite are produced at the solubility limit of CTAB compared to the multilayers produced at the 2 g CTAB level. Each individual delaminated layer is also further separated; a possible explanation is that a higher CTAB concentration prevents the aggregation of delaminated kaolinite nanoplatelets.

The higher molecular weight PVP K30 did not penetrate between the kaolinite nanoplatelets and properly delaminate the kaolinite. The PVP 10 platelets are not shattered like he PVP K30 platelets and have a thin disk like appearance. The delaminated kaolinite layers with sodium cholate as a surfactant gave many platelets having smooth edges and circular geometric orientation. However, there were more very small particles present on the delaminated kaolinite platelets.

Lower amounts of kaolinite treated in a batch produced delaminated nanoplatelets whereas increasing the weight to 10g and 15 g produced particulates with sharper edges having an aspect ratio closer to a square. This was verified by the increased circularity close to that of a square. The average circularity of the 15 g batch was 0.7 with many of the particles having the circularity of a square (0.886). The increased amount of kaolinite in the sonicating mixture lead to the breakup of the nanoplatelets. This indicates that there is an upper limit to the load of kaolinite that can be present in the sonication batch for a successful delamination.

CTAB at its solubility limit and PVP 10 were the surfactants that produced the most successful delamination of kaolinite nanoplatelets.

The average CED and the circularity data for each batch are summarized in Table 3.9. All of the batches were delaminated at 50% wt. urea solution. The 20 g of CTAB, 2g of PVP-10 and 15 g of kaolinite are the most circular. These batches also produced the most delaminated platelets.

Table 3.9: Summary of CED and circularity

Batch	**Average CED from area (μm)**	**Average CED from perimeter (μm)**	**Average Circularity**
30% power	3.6	5.8	0.628
40% power	3.0	4.5	0.664
50% power	3.6	5.1	0.700
100% power	2.7	4.0	0.671
2 g of CTAB	4.9	8.6	0.569
20 g of CTAB	6.7	9.2	0.732
2 g of PVP (K30)	5.5	11.3	0.49
13.3 g of PVP (K30)	6.0	11.4	0.525
2 g of PVP-10	3.8	4.9	0.767
8.611 g of sodium cholate	5.4	10.5	0.517
5 g of kaolinite	2.95	6.3	0.625
10 g of kaolinite	2.5	6.7	0.607
15 g of kaolinite	2.54	5.0	0.694

Table 3.10 is the summary of the minimum, maximum area and perimeter for delaminated batches. 13.3 g of PVP (K30) batch has the largest platelet area and 10 g of kaolinite batch has the longest perimeter.

Table 3.10: Summary of minimum, maximum area and perimeter.

Batch	**Minimum area** (μm^2)	**Maximum area** (μm^2)	**Minimum perimeter** (μm)	**Maximum perimeter** (μm)
30% power	0.20	336	1.76	255
40% power	0.20	129	1.67	180
50% power	0.20	269	1.73	238
100% power	0.20	320	1.71	237
2 g of CTAB	0.20	381	1.66	390
20 g of CTAB	0.34	198	3.19	116
2 g of PVP (K30)	0.21	462	1.99	355
13.3 g of PVP (K30)	0.21	628	2.10	418
2 g of PVP-10	0.20	465	1.62	200
8.611 g of sodium cholate	0.20	465	1.62	200
5 g of kaolinite	0.20	392	1.70	348
10 g of kaolinite	0.20	399	1.62	661
15 g of kaolinite	0.20	373	1.71	305

3.7 Conclusions

The ultrasonication of kaolinite was studied as a function of sonication power, concentration of kaolinite and the presence of both urea and selected surfactants in the sonication mixture. Increasing ultrasonication power in a 50 % wt. urea solution without the presence of surfactants shatters kaolinite nanoplatelets into smaller particles. The introduction of a surfactant significantly altered the morphology of the delaminated kaolinite.

Adding CTAB into 50 % wt. urea solution produced single or multilayer kaolinite nanoplatelets with circular edges. There were fewer fine particles deposited on the delaminated kaolinite layers compared to the non-surfactant runs. Fine kaolinite nanoplatelets were not formed when PVP K30 was used. The geometric morphology of the platelets was different compared to the CTAB batch, as the vertices of the particles were much sharper.

The morphology of the platelets using PVP-10 was circular and had a “dish” like structure. The distance between each platelet was moderately close with fine kaolinite particles on the larger platelets. The delaminated kaolinite layers using sodium cholate as a surfactant gave many platelets having smooth edges and circular geometric orientation. However, there were more very small particles present on the delaminated kaolinite platelets.

The final experiment set was performed to determine if a larger quantity of kaolinite can be delaminated at the same surfactant concentration. The results indicate that kaolinite was degraded to a greater extent with increasing amount of kaolinite in the sonication mixture. The increased amount of kaolinite in the sonicating mixture lead to the breakup of the nanoplatelets. This indicates that there is an upper limit to the load of kaolinite that can be present in the sonication batch for a successful delamination.

It can be concluded that the presence of surfactant has positive effects on kaolinite delamination process to form nanoplatelets. The kaolinite is delaminated to a greater extent when higher ultrasonication power and a high concentration of urea and surfactant are used. Kaolinite is most delaminated when the concentration of urea and surfactant is near its solubility limit and at the highest sonication power. CTAB at its solubility limit and PVP 10 were the surfactants that produced the most successful delamination of kaolinite nanoplatelets.

Chapter 4 Magnetite Nanoparticle Synthesized on Aluminum-based Substrates

The manuscript for submission, Xinlong Chen, A. Y. Tremblay

Abstract

Magnetite nanoparticles were synthesized using a wet chemical co-precipitation approach with the application of surfactants at selected concentrations. These particles were deposited on various nanoplatelet supports such as boehmite, alumina and kaolinite. Transmission electron microscopy (TEM) and image software were used to characterize the iron oxide(s) nanoparticle morphology and to determine the iron oxide nanoparticle diameters. In-situ Energy-Dispersive X-ray Spectroscopy (EDS) was used to detect the existence of aluminum, iron, silicon and oxygen elements in the sample. X-ray diffraction (XRD) spectroscopy was used to determine the composition of each iron oxide(s)-substrate complex.

Statistical analysis reveals that 65% of the unsupported magnetite nanoparticles produced measured less than 5 nm. The nanoparticles deposited on boehmite and those co-synthesised with magnetite-boehmite had 41 and 81% of their diameters less than 5 nm respectively. When co-synthesized, magnetite nanoparticles and boehmite were observed not to precipitate simultaneously due to the different pH of precipitation of their hydroxides. The nanoparticles deposited on kaolinite had rectangular and circular morphologies. It was found that magnetite nanoparticles deposited on boehmite tend to locate around the perimeter of the nanosheet. Calcination was shown to increase nanoparticle diameters due to nanoparticle coarsening.

Keywords: magnetite nanoparticle, kaolinite, boehmite, twinned alumina nanosheet, wet chemical synthesis, co-precipitation

4.1 Introduction

Nanoparticles (NPs), made from either inorganic or organic materials, possess many novel properties compared to their bulk counterparts [104]. Nanoparticles are widely used in the fabrication of biosensors [182], MRI contrasting agents [183], arrays in magnetic data storage devices [184] and catalyst [185][186]. They are also used in drug delivery [187] and heavy metal ion separations [188], [189].

A potentially new application of nanoparticles is in the production of hydrogen from methane by direct methane cracking. In this process, methane is reacted over iron nanoparticles to grow carbon nanotubes [190]. Iron based catalysts were reported in the literature to be efficient for catalytic methane cracking [191]–[194]. Methane decomposition rates upon application of metal catalysts is in the order of (Co, Ru, Ni, Rh) > (Pt, Re, Ir) > (Pd, Cu, W, Fe, Mo) [44], [195], [196].

The calcination of iron precursors leads to the formation of a variety of iron oxides. Depending on the calcination temperature, magnetite (Fe_3O_4), maghemite ($\gamma - Fe_2O_3$), wustite (FeO), hematite ($\alpha - Fe_3O_3$) and/or spinel structures (AB_2O_4) are formed between the iron based oxides and support oxides [87]. The octahedral or tetrahedral crystal orientation is kept in cationic solution form (Fe^{2+}or Fe^{3+}) when oxygen is present. The hydrogen produced during the cracking reaction allows in-situ iron oxide reduction if the iron-based nanoparticles were to oxidize [197].

One of the primary concerns in nanoparticle synthesis is particle size control and its distribution as this directly governs nanoparticle properties [105]. In order to continuously synthesize carbon nanotubes (CNTs), they must synthesize by a base growth mode. This is required to maintain catalyst activity. Base growth mode occurs when the nanoparticle is less than 5 nm [113].

A thermodynamic analysis of the carbon nucleation at a metal surface was conducted by Kuznetsov et al [198], [135]. Their thermodynamic model established the relationship between nanocatalyst size with consideration of its immediate neighbor (substrate) and the mechanisms of different carbon allotropes formation. By modifying Kuznetsov's model, Dijion et al. [137] conducted a series of experimental test and applied the modified model to verify the correlation between the energy variation of system and nanoparticle size. To date, extensive studies were performed, and

the results are available in the literature covering various iron salts solutions, surfactants, solvents and their respective concentrations used in synthesizing CNTs.

In order to achieve successful CNTs by the base growth mode for methane cracking, the nanoparticle must be deposited on a substrate and must not be detached from the substrate during the cracking reaction. The nanoparticle must also maintain its catalytic activity throughout the entire reaction process [114]. The deposition of iron on alumina and silica substrates utilizing physical and chemical deposition methods was reported in literature [135]–[137]. For example, Moody *et al*. grew iron oxide nanoparticles on a silica membrane [136]. The iron oxide nanoparticles were then calcined with a gas mixture consisting of both hydrogen and argon in order to prevent magnetite from oxidizing into hematite and/or maghemite. The magnetite nanoparticles were well distributed (spacing between each nanoparticle) from each other and hence no large nanoparticle aggregates were seen in their TEM images.

Another example of depositing nanoparticles on a thin film of silica was conducted by Gohier et al. [135]. They deposited cobalt, iron and nickel nanoparticles of different average diameters on a thin film of silica by physical vapour deposition (PVD). These films were annealed under vacuum at 700°C in order to form nano-scale islands of catalyst.

Many magnetite synthesis routes have been developed, such as the wet chemical synthesis [115]–[117], gas-phase flame synthesis [118], electrochemical synthesis [119], microwave [199] and ultrasound [200], hydrothermal [201], inverted coprecipitation [202] and thermal decomposition [203]. Among these synthesis routes, wet chemical synthesis has been widely used due to its simplicity, versatility and economic viability. A mixture of Fe^{2+} and Fe^{3+} based salts are used to synthesize magnetite nanoparticles. The reduction of Fe^{2+} and Fe^{3+} is expressed in Eq. (4.1);

$$Fe^{2+} + Fe^{3+} + 8OH^{-} \rightarrow Fe_3O_4 + 4H_2O \tag{4.1}$$

In order to prevent Fe^{2+} ions in the reaction mixture from oxidizing to Fe^{3+} ions before the reduction reaction occurs, an acid is usually added to the solution to prevent the oxidation of Fe^{2+} ions [120]. The balance between $Fe^{2+}$and Fe^{3+} ions are controlled by the kinetics of oxidation

and reduction. Thermodynamic and kinetic parameters indicate that the reduced iron will be rapidly oxidized to the insoluble form, leaving a very low concentration of the soluble Fe^{2+} ions due to the presence of oxygen [204]. Oxidation kinetics are dependent on the state of the ions. Fe^{2+} ions in aqueous form are readily oxidized to Fe^{3+} due to the octahedral structure of both ionic states where only a single electron is transferred during the oxidation reaction and thus the activation energy is low, therefore reaching equilibrium within seconds to minutes [205]. A base is then added to the iron salt solution to affect the precipitation of the nanoparticles as in reaction 4.1.

There are extensive studies in the literature regarding the effect of organic anions on the formation of iron oxides and the size distribution of maghemite (Fe_2O_3, γ-Fe_2O_3) nanoparticle [126]–[128]. For example, citrate ions have been shown to influence the growth of iron oxides [128]–[130]. Bee et al. [131] studied the relationship between the citric acid concentration and the diameters of polydisperse spherical magnetite nanoparticles. In the absence of citrate ions, the typical maghemite nanoparticle diameter is approximately 8 nm, whereas when citrate ions are present, the maghemite diameter can be as small as 2 nm.

The relationship between the nanoparticle diameter and R, The citric acid concentration $[C_6H_8O_7]$ over the summation of iron ion concentration $([Fe^{2+}] + [Fe^{3+}])$ (Eq. (4.2)) is shown in in Figure 4.1. The total concentration of iron salts in solution is 0.13M and the molar ratio Fe^{2+} to Fe^{3+} ion is 0.5 in Figure 4.1.

$$R = \frac{[C_6H_8O_7]}{[Fe^{2+}]+[Fe^{3+}]} \tag{4.2}$$

In general, the maghemite nanoparticle's diameter decreases with increasing citric acid concentration. Where in Figure 4.1, D is the nanoparticle's diameter. It can be concluded that an average maghemite nanoparticle diameter of 2.2 nm can be synthesized at a value of R=3.

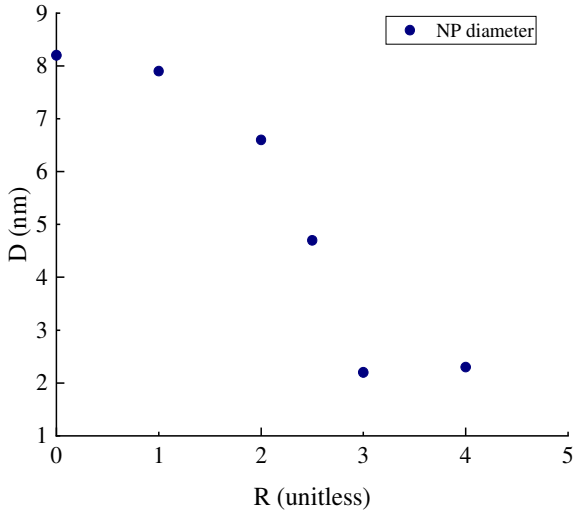

Figure 4.1: Relationship between nanoparticle diameter *D* and the *R* (citrate anion to total iron ions molar ratio [131]).

Yazdani et al. [125] studied the effect of the anions present in the iron salts used in the synthesis of the nanoparticles. Two reactant salts $FeCl_2$ and $FeSO_4$ were used as Fe^{2+} reagent ions, while three salts $FeCl_3$, $Fe_2(SO_4)_3$ and $Fe(NO_3)_3$ were used as Fe^{3+} reagents. Combinations of these salts were used to study the effect of anions on the resulting nanoparticle diameter. The combination of salts used and the resulting nanoparticle diameter are listed in Table 4.1. The concentrations were 0.1 M for both Fe^{2+} and Fe^{3+} cation salt solutions and an excess 1 M NaOH was used as the base.

Table 4.1: Combination of salts used and the resulting nanoparticle diameter

Set #	**Fe^{2+} reagent**	**Fe^{3+} reagent**	**Nanoparticle diameter (nm)**
1	$FeCl_2 \cdot 4H_2O$	$FeCl_3 \cdot 6H_2O$	10.03
2	$FeCl_2 \cdot 4H_2O$	$Fe_2(SO_4)_3$	6.6
3	$FeCl_2 \cdot 4H_2O$	$Fe(NO_3)_3 \cdot 9H_2O$	8.86
4	$FeSO_4 \cdot 7H_2O$	$FeCl_3 \cdot 6H_2O$	8.7
5	$FeSO_4 \cdot 7H_2O$	$Fe_2(SO_4)_3$	5.1
6	$FeSO_4 \cdot 7H_2O$	$Fe(NO_3)_3 \cdot 9H_2O$	8.23

Figure 4.2 shows the trend of ionic strength versus the magnetite nanoparticle diameter. The ionic strength of the solution is calculated as a half of the sum of the molar concentration of ions multiplied by the square of the ion charge [125]. It is evident that the weaker ionic strength results in an increase of the magnetite nanoparticle diameter by the order of S1 > S3 > S4 > S6 > S2 > S5. The magnetite nanoparticle diameters were also calculated using the Scherrer equation, and shown in Figure 4.2. It was also observed that larger size anions normally result in smaller diameters of magnetite nanoparticles due to an increase of diffusion distance that surrounds the nuclei.

Jolivet et al. [206] showed that the growth of nanoparticle oxides in aqueous solution can be controlled by the ionic strength of the reaction medium. The relationship between the ionic strength and the nanoparticle size is plotted in Figure 4.3. It can be concluded that higher ionic strength results in smaller nanoparticle diameters. From this conclusion, both Fe^{2+} and Fe^{3+} cations should have strong anion counterpart (SO_4^{2-} anion) to produce nanoparticles having the smallest size.

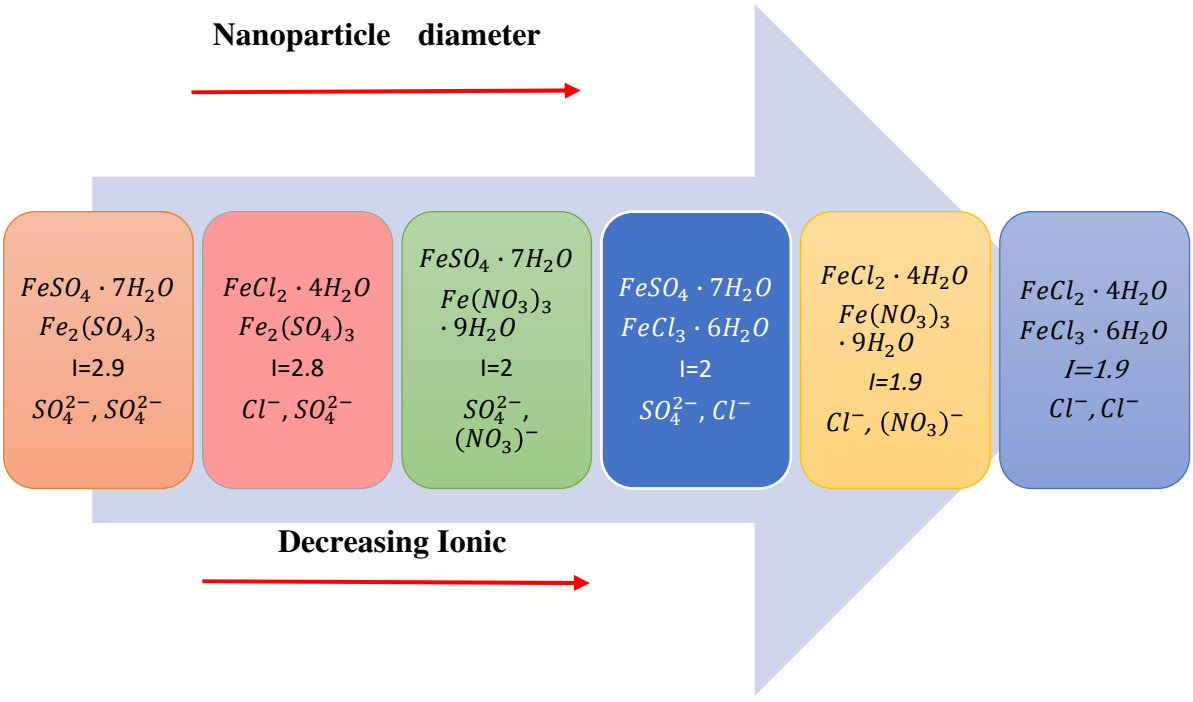

Figure 4.2: Iron salt reagent ionic size and strength effect on the final magnetite nanoparticle diameter [125].

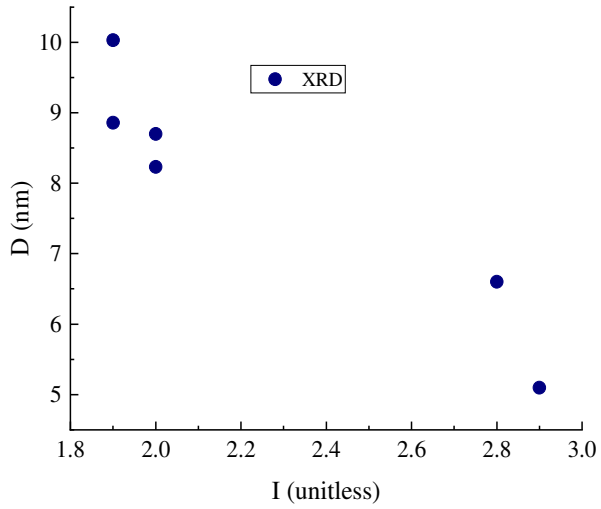

Figure 4.3: Relationship between ionic strength and nanoparticle diameter calculated from Scherrer's equation using XRD [125].

Apart from the correlation between the ion strength and the nanoparticle size, surfactants were reported to affect the morphology, structure and size of iron nanoparticles [125]. Cetrimonium bromide (CTAB) is a cationic surfactant that interferes with the negatively charged external iron oxide nanoparticle's crystal surface produced during a reduction reaction with sodium hydroxide.

Filippousi et al. [133] used iron(II) sulphate heptahydrate ($FeSO_4 \cdot 7H_2O$), iron(III) chloride hexahydrate ($FeCl_3 \cdot 6H_2O$) and cetrimonium bromide (CTAB) surfactant to synthesize magnetite nanoparticles. CTAB is a cationic surfactant that interferes with the negatively charged external iron oxide nanoparticle's crystal surface produced during the reduction reaction with sodium hydroxide. The surfactant itself does not change the geometry and structure of the magnetite nanoparticles; it also does not affect the magnetite nanoparticle morphology. However, the surfactant does control the degree of aggregation of the nanoparticles due to hydrophobic interactions [132].

Iron deposition on alumina and silica substrates by physical or chemical deposition approaches are reported in the literature [135]–[137]. Moody *et al*. have synthesized iron oxide nanoparticles on top of a silica membrane by thermal decomposition of iron carboxylate complexes. [136]. The iron oxide nanoparticles were then calcined with a hydrogen and argon gas mixture to prevent

magnetite nanoparticles from oxidizing further into hematite and/or maghemite nanoparticles. The individual magnetite nanoparticle were well spaced from each other and almost achieved monodispersed distribution on the silica membrane substrate.

Another study on the deposition of nanoparticles on a thin film of silica was conducted by Gohier et al. [135]. They sputtered cobalt, iron and nickel nanoparticles on a thin film of silica by PVD and obtained different diameter nanoparticles deposited on a film of silica. These films were then annealed under vacuum at 700°C in order to form nano-scale metal islands. The nano-scale islands had distance greater than 10 nm between each nanoparticle deposited on the substrate.

Motivated by the above analysis, the present study aims at investigating the size and morphology of magnetite nanoparticles produced by wet chemical synthesis methods [105], [134] and deposited on alumina based substrates. The magnetite nanoparticles were synthesized using cetrimonium bromide (CTAB) and iron salts. CTAB is a widely used surfactant for the synthesis of gold nanorods, and it was shown that it can control nanoparticle size. The resulting samples in this work were then characterized using a scanning electron microscope (SEM), transmission electron microscope (TEM) and with energy-dispersive x-ray spectroscopy (EDS) techniques to probe magnetite nanoparticle properties. The size and morphology of the nanoparticles were determined using an image analysis software (ImageJ).

In this study; kaolinite, boehmite and twined alumina sheets (TAN) were used as substrates for the deposition of magnetite nanoparticles as the thickness of their nanoplates is typically less than 100 nm. They can also be used as catalyst supports for CNT growth because they have smooth flat surfaces that could eventually lead to the release of the CNTs. The sub 100 nm thickness of the nanosheets also permits the study of magnetite nanoparticles on their surface by TEM.

4.2 Materials and Preparation

Aluminum chloride hexahydrate (99%, nitrogen flushed), iron chloride hexahydrate, iron sulphate heptahydrate, cetyltrimethylammonium bromide (CTAB), sodium hydroxide pellets and anhydrous ethanol were purchased from Fisher Scientific; Fluka Analytical grade kaolinite powder and PVP-10 $\left(\mathrm{M_{avg.}} = 10000\,\mathrm{g/mol}\right)$ were purchased from Sigma–Aldrich (Switzerland).

A Fisher Scientific 550 Sonic Dismembrator ultrasonicator was used to ultrasonicate the surfactant-kaolinite colloid. Samples were washed by a Corning LSE vortex mixer and Hermle Z400K refrigerated bench top centrifuge was used during the decantation process. Magnetite nanoparticles and substrates were mixed in a 250 mL conical flask and spun by a magnetic stirrer. Magnetite nanoparticles deposited on boehmite underwent hydrothermal reaction in Teflon tubes within a pressurized stainless-steel autoclave (Parr Instrument Company, Illinois). SEM micrographs were taken with JSM-7500F FESEM (JEOL) operated at 3 keV with EDS. TEM micrographs were taken with JEM-2100F FETEM (JEOL) operated at 200 keV. XRD spectroscopy was done by Rigaku Ultima IV Diffractometer and scanning powder samples at 0.5°/min using CuK radiation (λ= 1.5418 Å).

4.2.1 Magnetite nanoparticle

Initially, 0.656 g of CTAB and 0.5406 g (2mmol) of $FeCl_3 \cdot 6H_2O$ were dissolved in 30 mL of deionized (DI) water in a 50 mL centrifuge tube and then 0.27802 g (1mmol) of $FeSO_4 \cdot 7H_2O$ was added to the same solution. The original recipe by Filippousi et al. [133] was modified by adding 1:1 molar ratio of citric acid to Fe^{2+}. The introduction of citric acid into the iron salt solution is to prevent Fe^{2+} ions oxidizing to Fe^{3+} ions and precipitating out before reacting with base (NaOH).

The solution was then agitated in a vortex mixer for 5 min to ensure all of the iron salts in solution and the CTAB surfactant were well mixed. Five (5) mL of 5 M of NaOH solution was then added to the iron salt solution, and a black precipitate was immediately formed. This thin magnetite nanoparticle mixture colloid was then spun for 5 min in using a vortex mixer in order to ensure that the sodium hydroxide had completely reacted with the iron salt.

4.2.2 Boehmite and twined alumina nanosheet (TAN) preparation

Approximately 4.35g of $AlCl_3 \cdot 6H_2O$ was added into 60 g of DI water in an Erlenmeyer flask. 0.849 g of CTAB was added into 45 g of ethanol in a 100 mL beaker. The CTAB solution was then mixed with magnetic stirrer for 20 mins to ensure that the CTAB was completely dissolved and well mixed.

The pH was raised to 14 by adding 2.89 g of finely ground fresh sodium hydroxide powder into 30 g of DI water in 100 mL. The result was a fine dispersion of NaOH in DI water. This was immediately added into an aluminum chloride hexahydrate-CTAB solution. Clusters of small white flakes immediately formed upon adding the sodium hydroxide to the aluminum chloride hexahydrate-CTAB surfactant solution. This aluminum chloride hexahydrate-CTAB surfactant solution was poured in three 10 mL Teflon tubes and placed in a sealed pressurized stainless-steel reaction vessels (autoclaves) before loading into a 165 °C oven.

The $CTA^+ - AlO_2^-$ ion pairs were initially formed in the solution by electrostatic interaction between the CTAB surfactant and $NaAlO_2$. An ordered nanoplatelet structure of boehmite was produced by self-assembly of $CTA^+ - AlO_2^-$ ion pairs via the hydrothermal reaction expressed below in Eq. (4.3);

$$AlO_2^- + H_2O \rightarrow (\gamma - AlOOH) + OH^- \tag{4.3}$$

The hydrothermal reaction shown in Eq. (4.3) was carried out in a pressurized autoclave at 165 °C for 16 hours. After reaction, the autoclaves were taken out of the oven and cooled down to room temperature for 2 hours. The solids formed were decanted and of washed five times with distilled water and then 5 times with isopropanol. They were centrifuged after each washing step at 6000 rpm at 20°C for 20 mins. The resulting boehmite was decanted, and left to dry in a fume hood for 24 hours. Approximately 0.55 g of boehmite was obtained from each Teflon tube. Half of the boehmite was calcined for 4 hours at 600°C. The calcination process transformed boehmite $(\gamma - AlOOH)$ into gamma alumina $(\gamma - Al_2O_3)$ according to the reaction shown in Eq. (4.4);

$$2(\gamma - AlOOH) \rightarrow (\gamma - Al_2O_3) + H_2O \quad (4.4)$$

4.2.3 Kaolinite

A 50% wt. urea solution was prepared by adding 20 g of urea pellets into 20 mL distilled water and mixing in a vortex mixer to ensure the urea pellets dissolved completely. 2 g of PVP-10 surfactant and 20 g of kaolinite powder were added into the urea solution and mixed by a vortex mixer for 5 min to produce a well-mixed kaolinite-surfactant mixture. The kaolinite-surfactant mixture was then poured into a 140 mL beaker and ultrasonicated for 3 hours consisting of 10 s on at full power (100% intensity) and 1 min off. After the ultrasonication stage, the kaolinite underwent a decantation process consisting of washing five times with distilled water and then 5 times with isopropanol. The particles were recovered by centrifugation at 6000 rpm at 20°C for 20 mins. The processed kaolinite was stored in isopropanol and left to dry overnight in a plastic dish. They were used as substrates for nanoparticle deposition and studied under TEM.

4.2.4 Supported nanoparticle preparation

Six combinations of magnetite nanoparticles on boehmite, alumina and kaolinite were studied in this work. They are summarized in Table 4.2 characterized with or without calcination. The preparation of these supported catalysts is described in the following sections. The abbreviation refers to how the iron oxide nanoparticles that were prepared, deposited substrates and characterized with or without calcination. The preparation of these supported catalysts is described in the following sections.

Table 4.2: The six combinations of magnetite nanoparticle deposited on alumina-based substrates and kaolinite.

Combination number	**Name**	**Abbreviations**	**Characterized in Section**
1	Individual nanoparticles	MNP	4.3.1
2	Boehmite nanosheets	BN	4.3.2
3	Kaolinite platelets	Kao	4.3.3
4	5% wt. Fe_3O_4 deposited on boehmite	MNP-BN	4.3.4
5	5% wt. Fe_3O_4 deposited on alumina co-calcined	MNP-BN-calcined	4.3.5
6	5% wt. Fe_3O_4 and boehmite co-precipitation	COSYN-MNP	4.3.6
7	5% wt. Fe_3O_4, alumina co-precipitation and co-calcined	COSYN-MNP-TAN	4.3.7
8	5% wt. Fe_3O_4 deposited on kaolinite	MNP-Kao	4.3.8
9	5% wt. Fe_3O_4 deposited on kaolinite calcined	MNP-Kao-calcined	4.3.9

4.2.4.1 Direct deposition of MNP on BN and TAN

A schematic layout of depositing magnetic nanoparticle on boehmite nanosheets and TAN is presented in Figure 4.4. The calcination of the catalyst-substrate requires additional steps shown in below and also in Figure 4.4. A selected amount of magnetite nanoparticle prepared as shown in Figure 4.4 Step 1 a) was mixed with the boehmite colloid prepared as shown in Figure 4.4 Step 1b). The amount of magnetite nanoparticle was 5% wt. of the final MNP-BN catalyst.

1. 4.338 mL of $6.673 \times 10^{-3}\ g/mL\ Fe_3O_4$ nanoparticle solution was pipetted into a Teflon tube with an aluminum chloride hexahydrate-CTAB surfactant solution before undergoing hydrothermal reaction.
2. The Teflon tube was then sealed in a pressurized stainless-steel vessel and then loading into an autoclave and heated for 16 hours at 165°C under autogenous pressure.
    a. The precipitates formed during the crystallization stage accumulated at the bottom of the Teflon-lined tube in the form of a semi-ridged disc (step 1 in Figure 4.4) were collected.
    b. The precipitated underwent the decantation procedure in order to purify the catalyst and substrate complex.
3. Approximately half of the magnetite-boehmite complex by weight continued to step 3. The iron oxides and TAN were placed in an oven and calcined at 600°C for 4 hours (step 3 in Figure 4.4). Again, the sample underwent the decantation procedure before characterization.

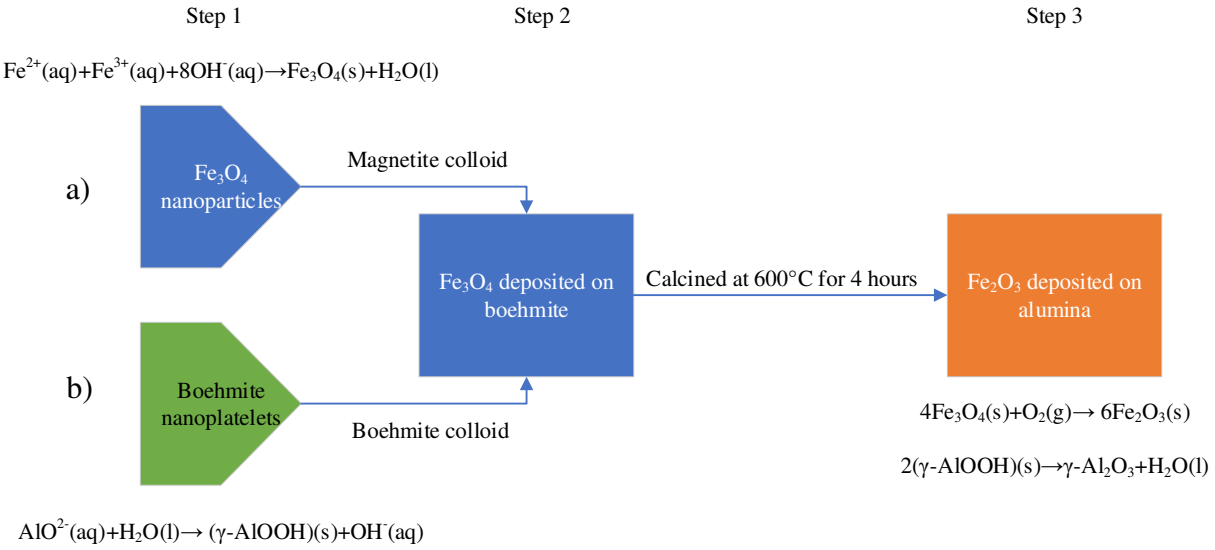

Figure 4.4: Direct deposition method of magnetite nanoparticle on boehmite and twinned alumina nanosheets. Boehmite was dehydrated into alumina after the calcination process.

4.3.4.2 Co-precipitation and co-calcination of MNP-BN and TAN

The co-precipitation and co-calcination procedure are summarized in Figure 4.5. Co-precipitation is the process of synthesizing both magnetite and boehmite simultaneously, and co-calcination is the process of calcinating magnetite and heating boehmite into TAN. The operating steps are presented as follows,

1. 3.18 mL of 1 mM of $FeSO_4 \cdot 7H_2O$ and 2 mM of $FeCl_3 \cdot 6H_2O$ solution was pipetted into a single Erlenmeyer flask containing aluminum chloride hexahydrate-CTAB solution.
    (a) The aluminum chloride hexahydrate-CATB solution turned from a transparent to a yellow transparent solution after mixing with Fe^{2+} and Fe^{3+} salt solutions.
    (b) A base solution containing 2.89 g of sodium hydroxide in 30 mL of DI water was added into the trinary metal salt solution. An opaque black colloid formed immediately.
    (c) The black opaque solution was stirred for 24 hours in a temperature-controlled bath set to 20°C. After 24 hours of stirring, the opaque black colloid turned into a brown colloid.
    (d) The opaque brown colloid was then transferred into the Teflon-lined tubes and then sealed in a pressurized stainless-steel capsule. The stainless-steel capsule was heated in an autoclave for 16 hours at 165°C under autogenous pressure.

(e) The stainless-steel vessel was then left to cool to room temperature. The precipitates formed during the crystallization stage accumulated at the bottom of the Teflon-lined tube in the form of a disk (step 1 in Figure 4.5) were collected and decanted. The co-precipitated catalyst-substrate complex was left to dry in a fume hood for 24 hours.

2. The co-calcination of the co-precipitation magnetite-boehmite complex requires an additional step. The same calcination procedure from the direct deposition was utilized. Magnetite-boehmite complex was calcined at 600°C for 4 hours (step 2 in Figure 4.5).

   (a) The co-calcined samples were decanted by washing five times with DI water and five times with isopropanol consecutively. The co-calcinated iron oxides-TAN complex were placed on a plastic dish in a fume hood and allowed to dry for 24 hours prior to characterization.

The direct deposition of magnetite on pre-synthesised TAN and the calcination treatment after deposition was not conducted.

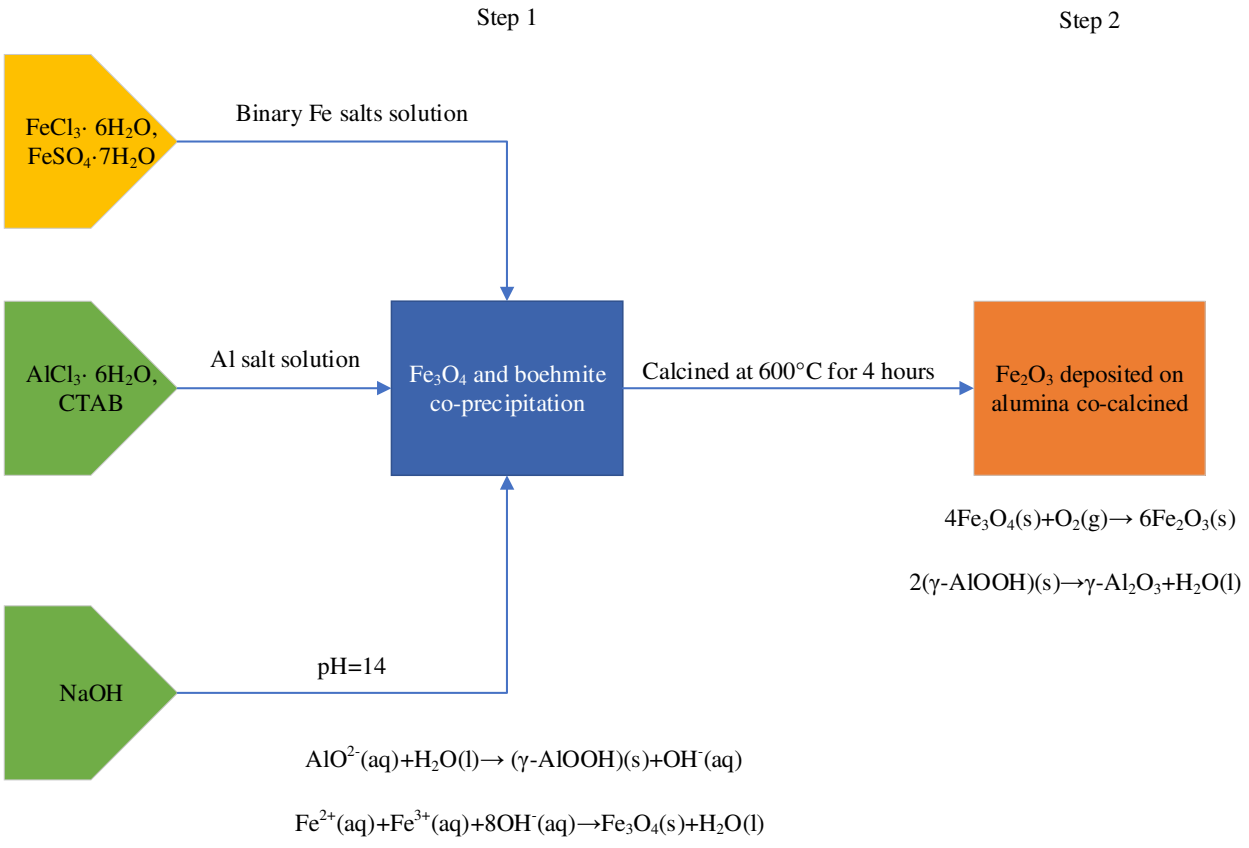

Figure 4.5: Magnetite nanoparticle and boehmite nanosheet co-precipitation in step 1. Both magnetite and boehmite are co-calcined in step 2. Boehmite was dehydrated into alumina after the calcination process.

4.3.4.3 Deposition of MNP on kaolinite

The procedure to deposit magnetite nanoparticles on kaolinite is almost identical compared to the direct deposition procedure discussed in section 4.3.4.2. A selected amount of magnetite nanoparticle prepared as shown in Figure 4.6 Step 1 a) was mixed with the boehmite colloid Figure 4.6 Step 1b). The amount of iron oxide nanoparticle was 5% wt. of the final MNP-Kao catalyst. The calcination of the magnetite-kaolinite complex requires an additional step.

1. 7.493 mL of $6.673 \times 10^{-3}\ g/mL$ magnetite nanoparticle colloid (prepared in step 1a) Figure 4.6) was pipetted into 0.95 g of ultrasonicated kaolinite (prepared in step 1b) in Figure 4.6) soaked in 30 mL of DI water.
    a. The ultrasonicated kaolinite-magnetite slurry was then stirred with a magnetic stirrer for 48 hours in ambient conditions.
    b. The colour of the kaolinite slurry before mixing, was white; after the addition of the magnetite nanoparticle colloid, the kaolinite slurry turned grey.
2. The magnetite-kaolinite complex underwent the decantation process and was left in a plastic dish placed in a fume hood for 24 hours to dry (step 2 in Figure 4.6) before characterization.
3. Approximately half of the magnetite-kaolinite complex was calcined in a muffled oven for 4 hours at 600°C (step 2 in Figure 4.6).
    a. The iron oxides-kaolinite complex was decantated and left to dry in a fume hood for 24 hours before characterization.

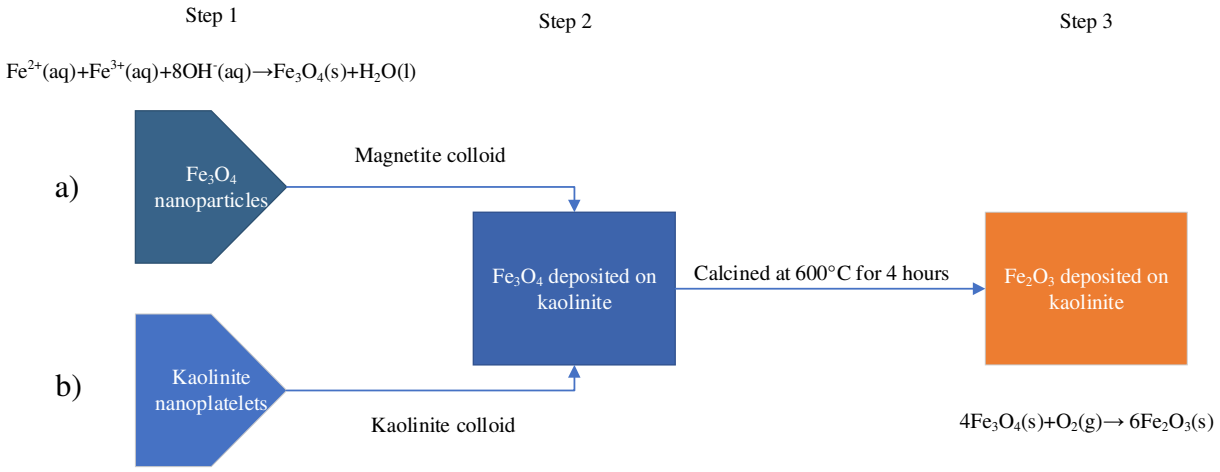

Figure 4.6: The deposition of magnetite nanoparticles on kaolinite nanosheets.

4.3 Results and Discussion

The magnetite nanoparticles listed in Table 4.2 above were characterized by SEM and TEM with in-situ EDS. Magnetite nanoparticles under the presence of CTAB surfactant were first synthesized using the recipe proposed by Filippousi et al. [133], this was done to verify if magnetite nanoparticles of sub 5 nm diameter could be fabricated. EDS analysis was conducted in order to confirm the presence of the iron, iron in magnetite, aluminum, and silicon in substrates. XRD spectroscopy was also done to verify the composition of iron oxide nanoparticles and substrates. All of the samples were stored in ethanol and ultrasonicated before placing them on a TEM grid. Each sample was left to dry in air for 5 minutes. The dry catalyst-substrate powder was placed directly on the XRD holder for scanning in the TEM.

Statistical analysis was conducted on the TEM micrographs by using the imaging software ImageJ. The nanoparticle's diameter was measured manually not automatically due to excessive background noise in each TEM micrograph. The limitation of ImageJ software is that it treats the static background noise as nanoparticles, another limitation is that slight changes in contrast ratio could result in large variance in the nanoparticle's area. Each nanoparticle's diameter was calculated from the nanoparticle's perimeter under the assumption that each nanoparticle was a perfect circle. The average, standard deviation, minimum and maximum diameters of the

nanoparticles were then calculated. The results were plotted using a data analysis software Origin Pro.

4.3.1 TEM and EDS observations of individual magnetite nanoparticles

Figure 4.7 shows a TEM of unsupported magnetite nanoparticles synthesized in the presence of CTAB using the recipe described in Filippousi et al. [133]. Both circular and rectangular orientation magnetite nanoparticle are observed. Aggregates of the nanoparticles are seen in the lower left and right corners in Figure 4.7 whereas the nanoparticles in the central region are more dispersed. It is interesting to see that several magnetite nanoparticle diameters are less than or approximately equal to 3.7 nm (inside the blue circle). Another factor to consider is that these nanoparticles are magnetic and are attracted to each other, thus promoting particle aggregation. The smaller magnetite nanoparticles are commonly located on the less densely packed area of the aggregate. A possible explanation for this phenomenon is that smaller magnetite nanoparticles have a much weaker magnetic field compared to larger counterparts and thus, the larger magnetite nanoparticles form larger aggregates.

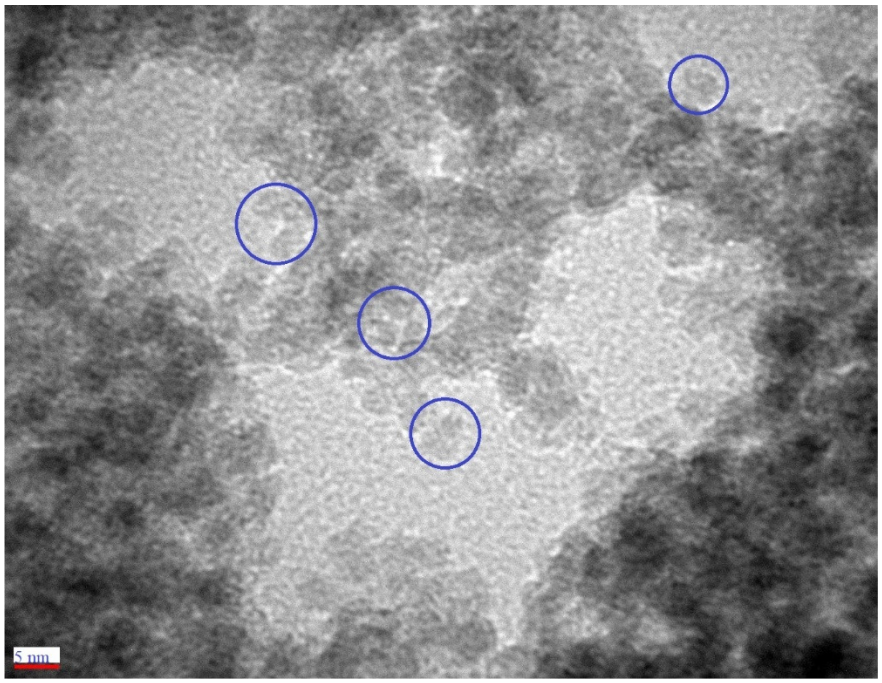

Figure 4.7: A cluster of magnetite nanoparticles. The red scale bar is 5 nm. The blue circle indicates that magnetite nanoparticles' diameter is less than or approximately 3.7 nm.

A sample size of 55 particles was selected for statistical analysis in Figure 4.9. The average, standard deviation, minimum and maximum diameter of magnetite nanoparticles in Figure 4.7 are 4.3, 1.75, 1.76 and 11.8 nm respectively. The diameter distribution of the magnetite nanoparticle of Figure 4.7 is plotted in Figure 4.8. From Figure 4.8, the vast majority (~65.42 %) diameter of the magnetite nanoparticles are less than 5nm, an interesting note is that there is an outlier peak for nanoparticles greater than 10 nm in diameter. A likely explanation is that clusters of miniature nanoparticles were counted as a larger single nanoparticle.

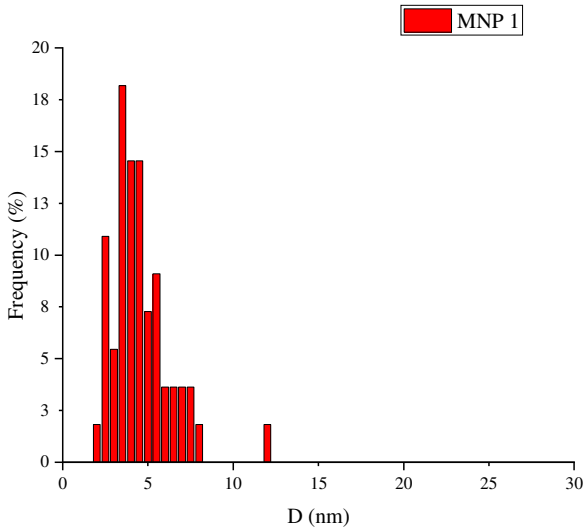

Figure 4.8: Diameter distribution for Figure 4.7

Figure 4.9 shows another TEM image of an isolated cluster of magnetite nanoparticles synthesized from this individual magnetite nanoparticle batch. Similar to the previous TEM micrograph (Figure 4.7), it was found that the smaller nanoparticles in Figure 4.9 were once again located at the clustered nanoparticles boundary. The packing of nanoparticles is least dense when the presence of neighboring nanoparticles is reduced. A noticeable difference between this image (Figure 4.9) and the previous micrograph (Figure 4.7) is that several rectangular oriented nanoparticles were detected. The vertices of each nanoparticles in this image are much shaper, whereas the edges are more curved as observed in the previous image.

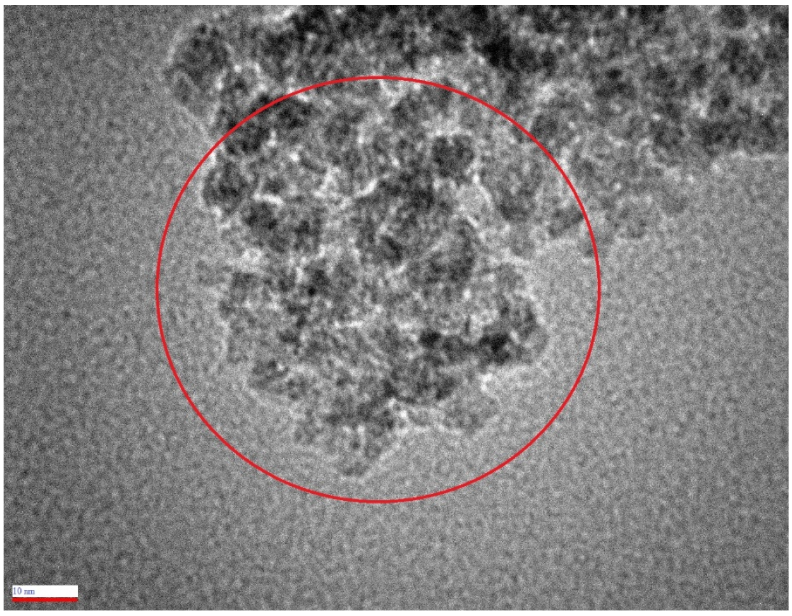

Figure 4.9: A cluster of magnetite nanoparticles. The red circle indicates the area where EDS analysis was conducted. The red scale bar is 10 nm.

A sample size of 39 was selected to conduct statistical analysis and the average, standard deviation, minimum and maximum diameter of the magnetite nanoparticles were 4.77, 1.7, 2.14 and 9.62 nm respectively. Once again, the size distribution obtained in this sample is comparable to those obtained by Filippousi et al. [133]. In Figure 4.10, approximately 41.6 % of the nanoparticles are less than 5 nm with a small peak at the 10 to 10.5 nm diameter range. The small black dots in the red circle in Figure 4.9 were not counted as nanoparticles due to the fact that these dots cannot be differentiated from the background noise or exposed part of a larger nanoparticle.

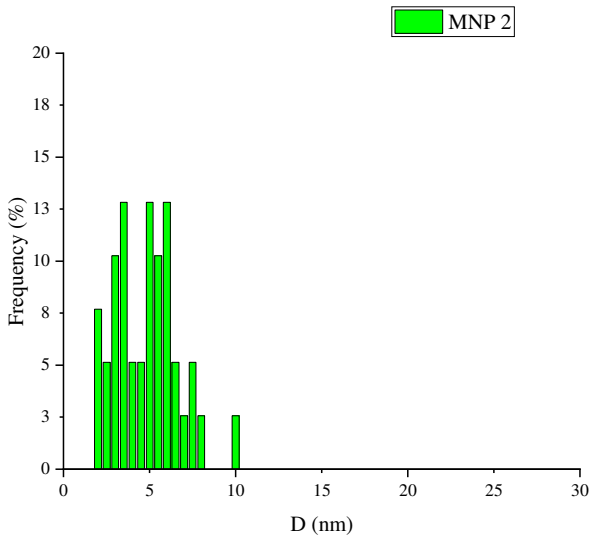

Figure 4.10: Diameter distribution for Figure 4.9

Figure 4.11 represents the EDS analysis of the TEM for the area marked by the circle in Figure 4.9. The presence of iron and oxygen elements were confirmed from the signal peaks, indicating that iron oxide compounds were formed during the synthesis. The corresponding EDS also shows a high presence of carbon, indicating that CTAB and trisodium citrate are present. Copper is present due to the background copper matrix used for the TEM image examination. Iron presence is well indicated. The presence of silicon indicates that there is possible silicon contamination perhaps due to sodium hydroxide etching on the glass containment vessel during magnetite synthesis.

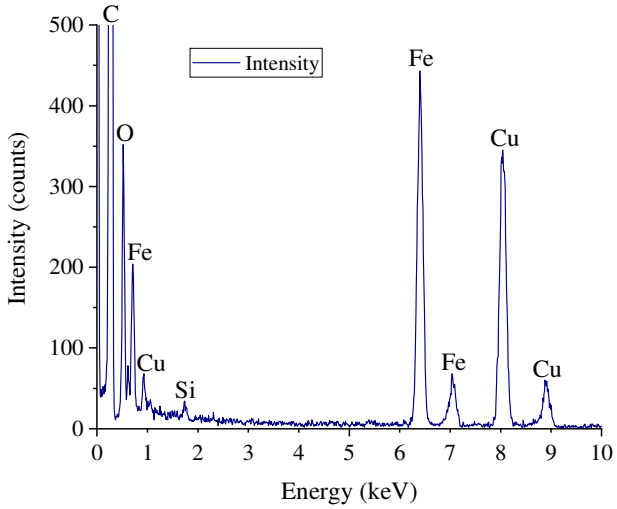

Figure 4.11: The EDS analysis of the red circle in Figure 4.9.

4.3.2 TEM and EDS observations of BN and TAN

Boehmite nanosheets were produced by adding sodium hydroxide into an aluminum chloride hexahydrate solution, while the TAN nanosheet were produced by calcinating the newly produced boehmite nanosheet. Both boehmite and TAN have a similar thickness, which confirms that the calcination process does not produce nanosheet coarsening. The structural orientation of boehmite is kept after the calcination reaction to TAN with straight edges and sharp vertices.

The thickness of the boehmite nanosheet ranges from 41.6 to 71.5 nm, as shown in Figure 4.12. Upon closer inspection in Figure 4.13, the boehmite's surface is much smoother at the nanometer scale compared to the micron level, where micron sized craters, grooves, ridges and valleys can be spotted on the left side of Figure 4.12. Upon higher magnification, it is revealed that boehmite is composed of multiple polycrystals separated by grain boundaries as shown in the backdrop of Figure 4.13. The length and width of the boehmite nanosheet are in the micron size range whereas in contrast the thickness of the nanosheet is in the sub 100 nm level. The edges of the nanosheets are straight, and the vertices are sharp with obtuse angles.

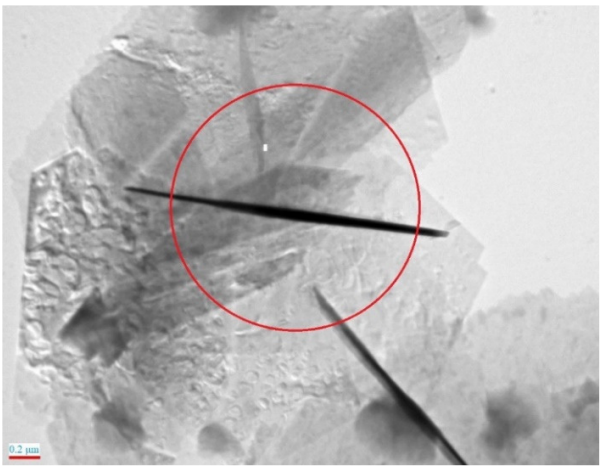

Figure 4.12: A TEM micrograph of two vertical standing boehmite nanosheets. The red circle is where the EDS scan was conducted. The red scale bar is 0.2 µm.

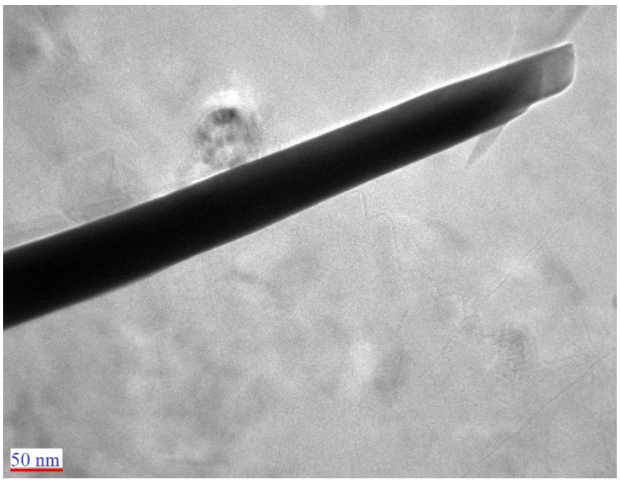

Figure 4.13: A segment of the right side of Figure 4.12. The red scale bar is 50nm.

Figure 4.14 is the EDS analysis of the red circle in the TEM micrograph (Figure 4.12). Both aluminum and oxygen have the highest peak in Figure 4.14, meanwhile chlorine has the weakest signal. The less intense chlorine peak confirms that almost all of the aluminum chloride hexahydrate reactant was consumed when sodium hydroxide base was added. The presence of sodium and chloride elements indicated by the peaks are most likely sodium chloride produced during the reduction reaction. While the CTAB surfactant residue left trapped within the overlapping boehmite nanosheets is responsible for the carbon peak signal. Another interesting fact is that this carbon peak signal is of lower intensity compared to that of Figure 4.11. The copper signal is from the background TEM gird matrix. The cobalt and iron peaks are either from contamination during the boehmite nanosheet synthesis stage or the background EDS equipment background noise.

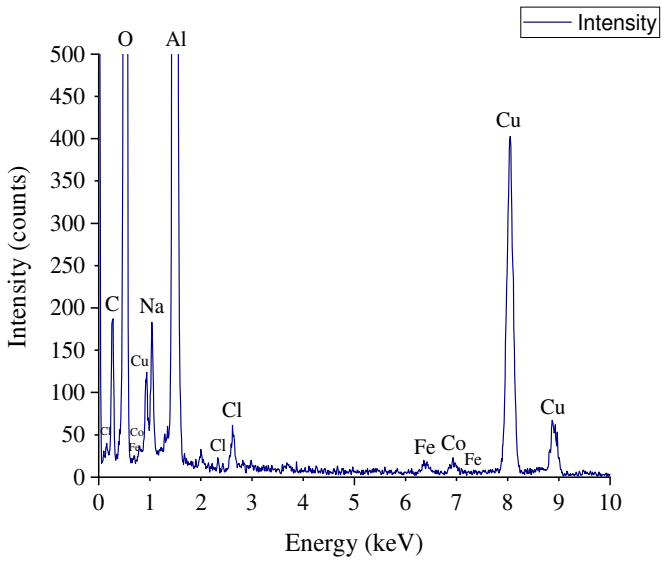

Figure 4.14: EDS analysis of the red circle in Figure 4.12.

The TAN nanoplatelets maintained the same thickness range as boehmite ranging from 14.9 to 87.6 nm thick as shown in Figure 4.15. The thickness measurements were taken on the right side of the darker TAN, which is oriented perpendicular to the plane of the micrograph, instead of the center area. The TAN in the center could be slanted on an angle and does not provide an accurate representation of its thickness. The length and width of TAN are in the micron scale, as shown in Figure 4.16, the edges are straight and jagged, and the vertices are sharp with obtuse angles. A segment of Figure 4.15 shows that the surface of TAN is different from the boehmite nanosheet; the TAN's surface is smooth at the nano level as there were no polycrystals or grain boundaries observed in the TEM image.

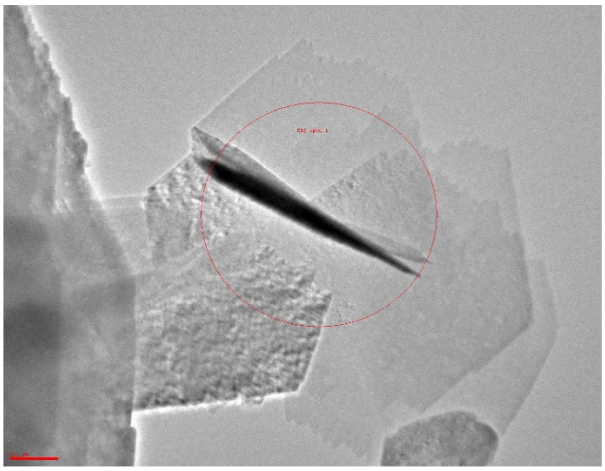

Figure 4.15: A TEM micrograph of multiple vertical standing TAN. The red circle is where the EDS scan was conducted. The red scale bar is 0.2 µm.

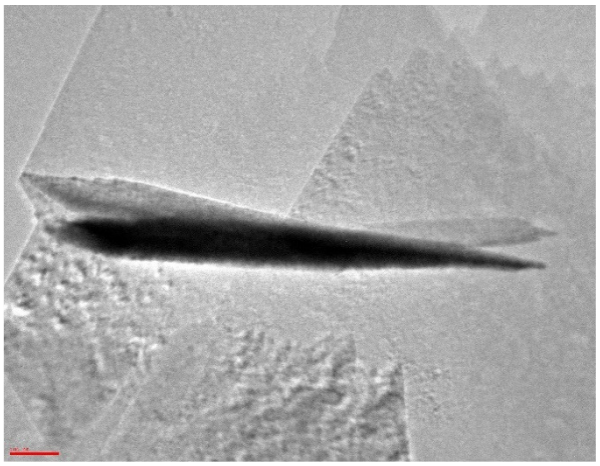

Figure 4.16: A segment of Figure 4.15. The red scale bar is 100 nm.

Figure 4.17 represents the EDS analysis of the area indicated by the red circle in TEM micrograph in Figure 4.15. The intense peak signals of aluminum and oxygen in Figure 4.17 confirm that aluminum oxide is present in the nanosheet. The sodium and chlorine peak signals are from sodium chloride products produced during the reduction reaction of aluminum chloride hexahydrate. The carbon peak signal is from the CTAB surfactant, as CTAB is the only compound that contains carbon elements. Cobalt and iron signal peaks are either contamination from the raw aluminum salt or background noise of the EDS detector. The copper peak signal is from the background TEM matrix grid slide.

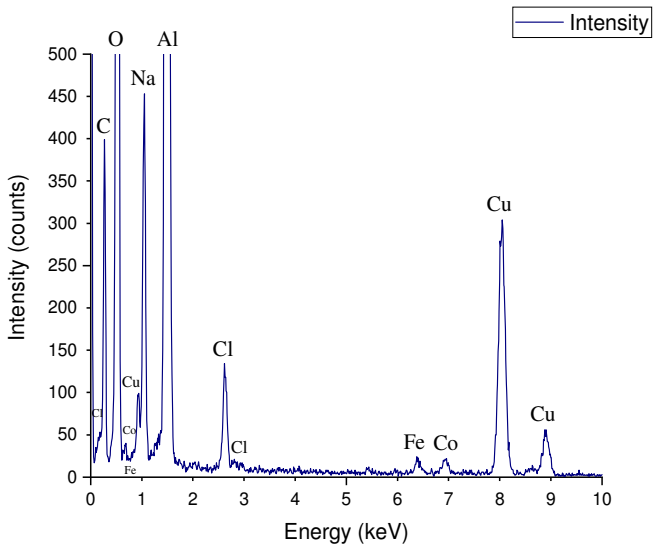

Figure 4.17: EDS analysis of the red circle in Figure 4.15.

4.4.3 TEM and EDS observations of kaolinite nanosheets

An overview of a multiple stacked kaolinite sheet is shown in Figure 4.18. The thickness of the kaolinite nanosheet is measured in Figure 4.19. The thickness of the kaolinite nanosheet ranges from 28.5 to 38.5 nm. The black lines observed in Figure 4.18 are possible interfaces between kaolinite interlayers held by hydrogen bonding. In direct contrast to boehmite and TAN, kaolinite nanosheets edges and vertices of perimeter are curved at the nanometer level as observed in Figure 4.19, whereas in boehmite and TAN the perimeter are straight featuring sharp edges (Figure 4.13 and Figure 4.16). The surface of kaolinite features craters and plateaus, where in direct contrast the surface of boehmite nanosheet and TAN are smoother. The kaolinite nanosheet observed at the micron level in Figure 4.18 are hexagonal, whereas the geometric orientation of boehmite nanosheet and TAN are rhombic shaped.

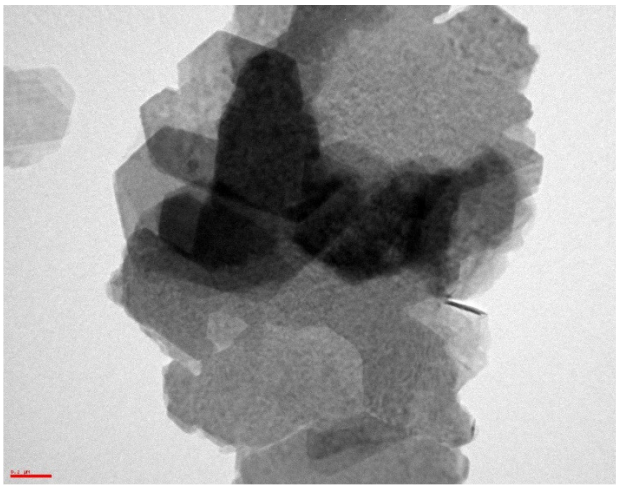

Figure 4.18: A TEM image of a kaolinite flake. A single vertical standing is observed. The red scale bar is 0.2 µm.

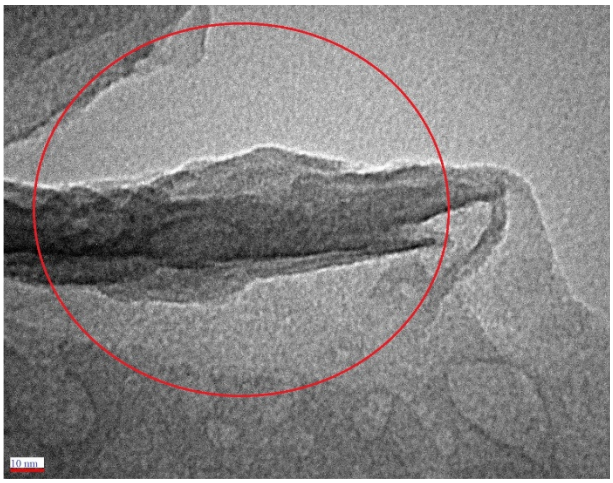

Figure 4.19: A zoomed in view of Figure 4.18 where the EDS analysis is conducted. The thick of the kaolinite nanosheet varies throughout the nanosheet. The red scale bar is 10 nm.

Figure 4.20 represents the EDS of the TEM for the area marked by the circle in Figure 4.19. The silicon peak in Figure 4.20 confirms the presence of silicon along with aluminum and oxygen as kaolinite (Al_2O_3 $2SiO_2 \cdot 2H_2O$) has silicon atoms in its structure. An almost equal intensity of aluminum and silicon were measured in Figure 4.20, this is expected from the formula of kaolinite. The copper peak is from the TEM matrix grid. The PVP-10 surfactant residues used during the delamination of kaolinite contribute towards the carbon peak. The cobalt and the iron peaks are either contaminants or the background signal from the EDS detector.

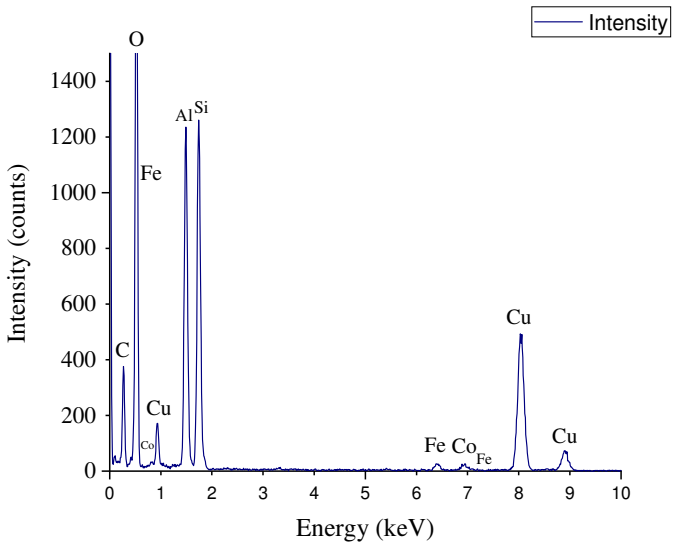

Figure 4.20: EDS analysis of Figure 4.19.

4.3.4 TEM and EDS observations for MNP-BN

The deposition of magnetite nanoparticles on boehmite nanosheet is shown in Figure 4.21. The magnetite particles are negatively charged [207] and the boehmite's surface is also negatively charged due to the hydroxide groups on its surface [208]; however the boehmite's edges are positively charged [208]. Thus, the magnetite nanoparticles are all aggregated on the boehmite nanosheet edges and vertices. A combination of circular, rectangular and irregular shaped magnetite nanoparticles can be seen in Figure 4.21. The circular shaped nanoparticles are located at the outer rim of the nanoparticle cluster, whereas rectangular shaped nanoparticles are typically found inside the cluster. Figure 4.22 is the EDS of the red circle in Figure 4.21. The iron, aluminum and oxygen peaks confirm the presence of magnetite and aluminium hydroxide oxide. The carbon atom in the CTAB molecule contributes to the carbon peak signal. The copper peak signal is from the TEM support grid.

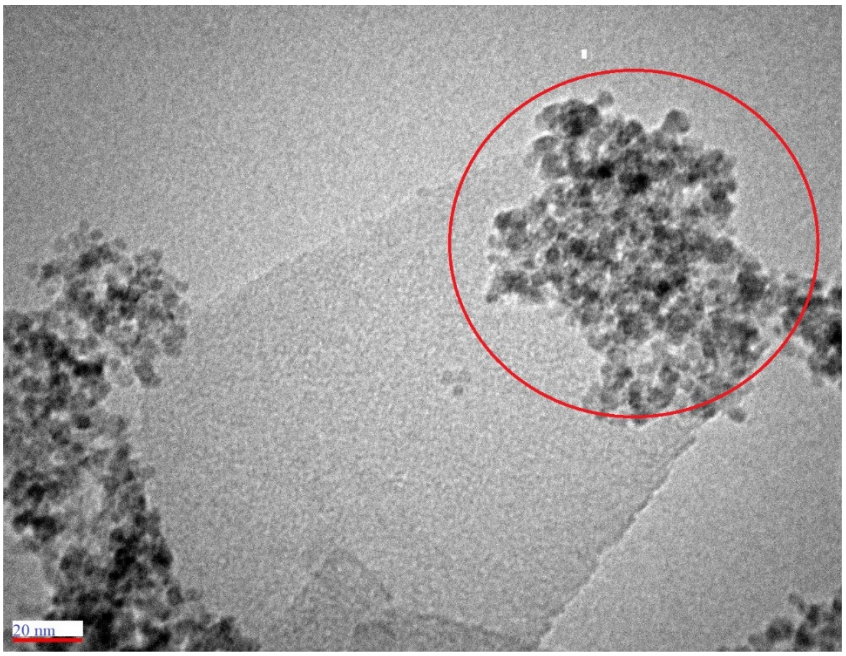

Figure 4.21: Magnetite nanoparticles deposited on boehmite nanosheet. The red circle is where the EDS spectroscopy analysis was conducted. The red bar is 20 nm.

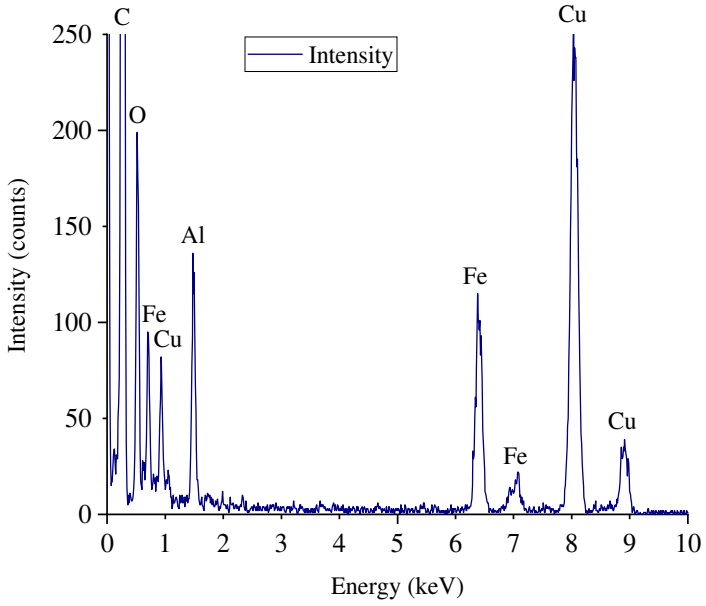

Figure 4.22*: EDS analysis of the red circle in Figure 4.21.*

A sample size of 78 was selected to conduct particulate statistical analysis and to plot the distribution function of particles in red circle in Figure 4.21. The average, standard deviation, minimum and maximum diameter of the nanoparticles are 5, 1.6, 1.8 and 8.3 nm respectively. From Figure 4.23, nearly 40% of the nanoparticle's diameters are less than 5 nm. The high degree of aggregation and the assumption of that the nanoparticles are a perfect circle contributes towards the standard deviation.

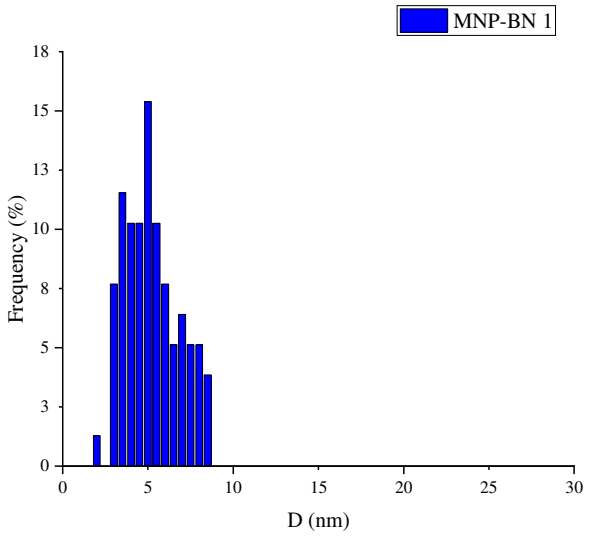

Figure 4.23: Diameter distribution of the particles in the red circle in Figure 4.21

4.3.5 TEM and EDS observations for MNP-BN-calcined

Figure 4.24 shows an overview of MNP-BN-calcined after calcination. A larger cluster of aggregated magnetite nanoparticles was located at the lower-left corner of the TAN nanosheet. Nanoparticle coarsening is the process of small nanoparticles merging into a larger nanoparticle. In an aggregation process, the nanoparticle cluster area is held by intermolecular forces, whereas in nanoparticle coarsening, the nanoparticles are held by intramolecular bonds. Nanoparticle coarsening is enhanced when the concentration increases due to a decrease in the separation between the nanoparticles. The coarsening can be reduced by introducing a new material within

the immediate proximity of the nanoparticle. The larger cluster of aggregated nanoparticles were once again located along the substrate's perimeter, which was consistent with the previous TEM image analysis in Figure 4.21.

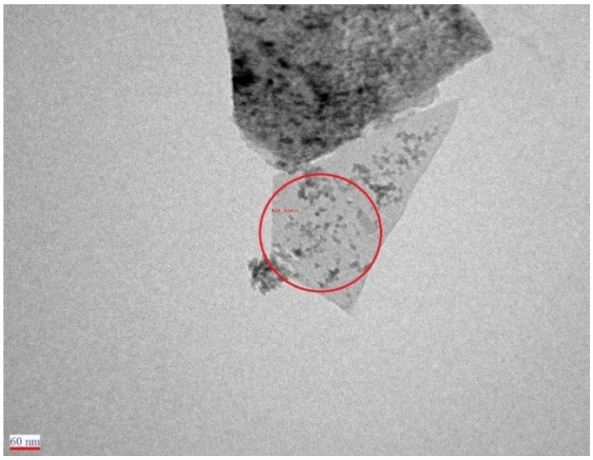

Figure 4.24: An overview view of MNP-BN-calcined after calcination. The red circle is where and EDS analysis is conducted. The red scale bar is 60 nm.

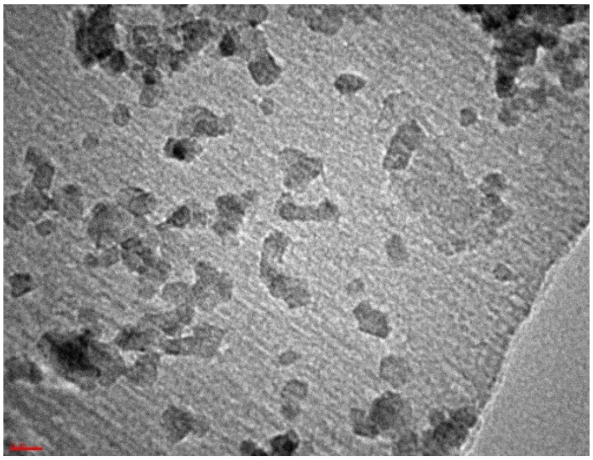

Figure 4.25: A segment of Figure 4.24. The red scale bar is 10 nm.

Nanoparticle coarsening was found at both the top left and right corners of the substrate, where the nanoparticle clusters have the largest aggregation of iron nanoparticles Figure 4.25. Figure 4.26 shows the EDS data for the area marked by the red circle in Figure 4.24. The EDS detected the presence of sodium in the sample, confirming that sodium citrate was produced during the reduction of citric acid with sodium hydroxide. The carbon signal has the highest intensity out of all elements, which demonstrates the presence of citrate ion and the CTAB surfactant. The combination of aluminum, iron and oxygen confirms the presence of iron oxides and aluminium oxide.

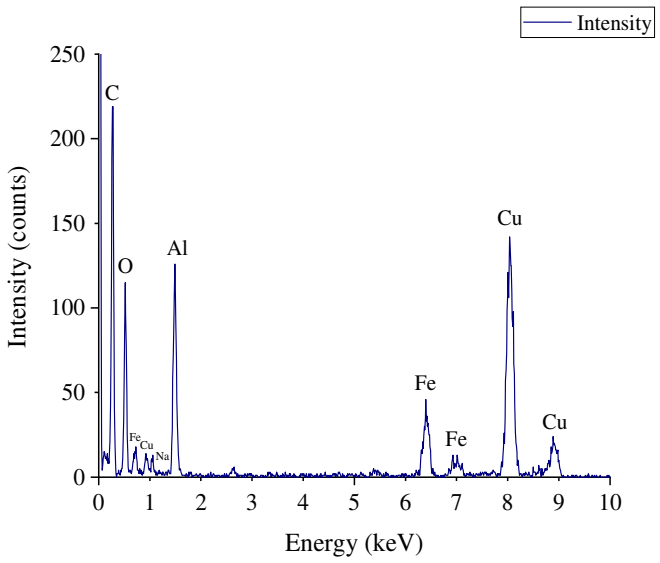

Figure 4.26: An EDS analysis of the red circle in Figure 4.24.

A sample size of 69 nanoparticles was selected to conduct the statistical analysis for diameter distribution shown in Figure 4.27. The measured average, minimum and maximum nanoparticle diameters are 9.1, 4.45, 3.6 and 23.56 nm respectively. This statistical result show that the post calcination of the nanoparticles increases the average diameter and leads to nanoparticle coarsening.

The majority (~94.2%) of nanoparticles have a diameter greater than 5 nm as presented in Figure 4.27. Some of nanoparticles in Figure 4.25 have joined together to form large nanoparticles, which is shown in Figure 4.27, where there are two peaks that have an average diameter greater than 20 nm.

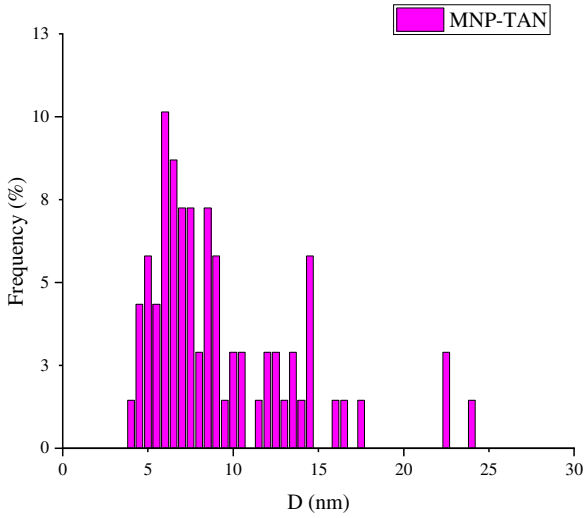

Figure 4.27: Diameter distribution for Figure 4.25

4.3.6 TEM and EDS observations for COSYN-MNP

Figure 4.28 depicts an image of COSYN-MNP, which shows that the thickness of the boehmite nanosheet is approximately 4.9 to 11.1 nm on a slanted angle. However, the contrast between the nanoparticle and nanosheet drops as the magnification increases. It was more difficult to identify the smaller magnetite nanoparticles if they are deposited in low concentrations or embedded within the substrate during the nucleation stage of the nanoparticle growth.

Figure 4.29 shows a higher magnification segment of Figure 4.28. The nanosheet on the top of the image is slightly slanted with another nanosheet underneath. Upon further inspection, multiple layers of boehmite can be observed. The magnetite nanoparticles are moderately dispersed on the boehmite surface. The majority of the nanoparticles are located within the substrate's inner surface, and a small number of nanoparticles are located near the perimeter. In contrast, the exact opposite nanoparticle distribution was observed in the direct deposition batch (MNP-BN) on the same substrate experiment earlier. Aggregated nanoparticles are observed in the top left region, whereas nanoparticle is relatively dispersed in the lower right region.

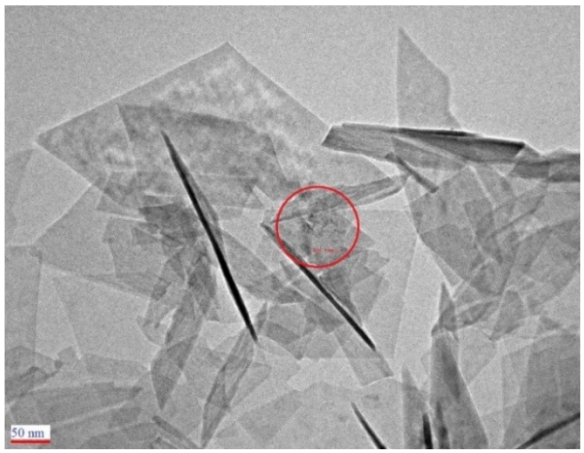

Figure 4.28: An overview of COSYN-MNP co-precipitation. The red circle is where an EDS analysis was conducted. The red scale bar is 50 nm.

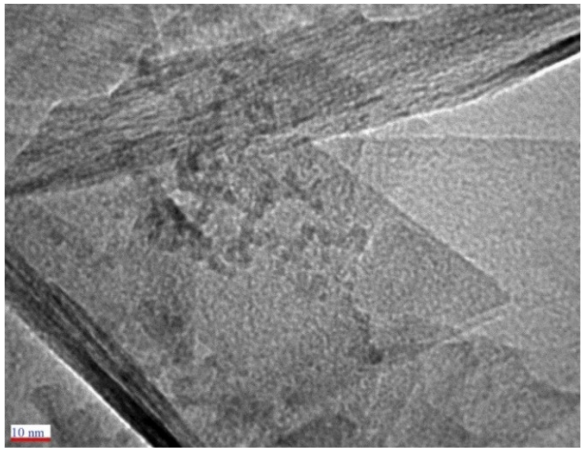

Figure 4.29: A segment of Figure 4.28. The contrast gradient decreases as magnification increases. The red scale bar is 10 nm.

Figure 4.30 is an EDS analysis indicated by the red circle in Figure 4.28. Elemental aluminum, iron and oxygen were detected; this confirms the presence of magnetite and aluminium hydroxide oxide. It is speculated that some of the CTAB surfactant is trapped in the magnetite nanoparticle when the boehmite precipitated later. This hypothesis may explain the weaker carbon signal in Figure 4.30.

A sample size of 69 particles were selected to conduct a statistical analysis of the particles in the red circle in Figure 4.31 The average, standard deviation, minimum and maximum diameter of the nanoparticles are 3.45, 1.1, 2.2 and 6.6 nm respectively. This experimental set gave the smallest average and minimum nanoparticle diameter. A possible explanation for this result is that nanoparticles are embedded in the nanosheet during the synthesizing stage; their growth is impeded due to the presence of the crystallising boehmite nanosheet.

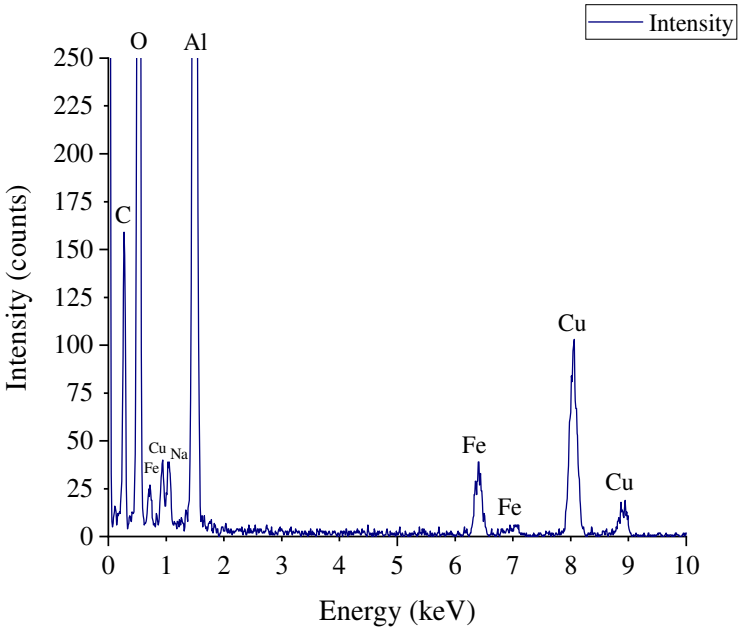

Figure 4.30: The EDS analysis for Figure 4.28.

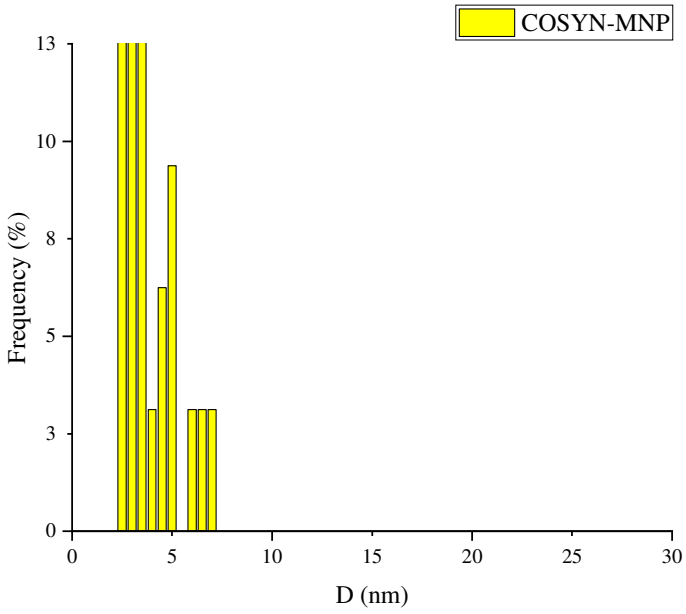

Figure 4.31: Diameter distribution of Figure 4.29.

In order to understand the dynamics of the co-precipitation process, a series of pH measurements were conducted in order to study the effect of slowly adding sodium hydroxide on the trinary salt solution (aluminum and iron salt solutions), Figure 4.32. The pH of the initial aluminum chloride hexahydrate-CTAB solution was 2.203 and the pH of the initial iron chloride hexahydrate and iron sulphate heptahydrates salt solution was 1.533. Mixing these two metal salt solutions resulted in pH of 2.233. The pH of the sodium hydroxide solution was approximately 12. Approximately 30mL of 0.121 M sodium hydroxide solution was injected at a constant flow rate into the trinary metal salt solution by a syringe pump for 3 hours.

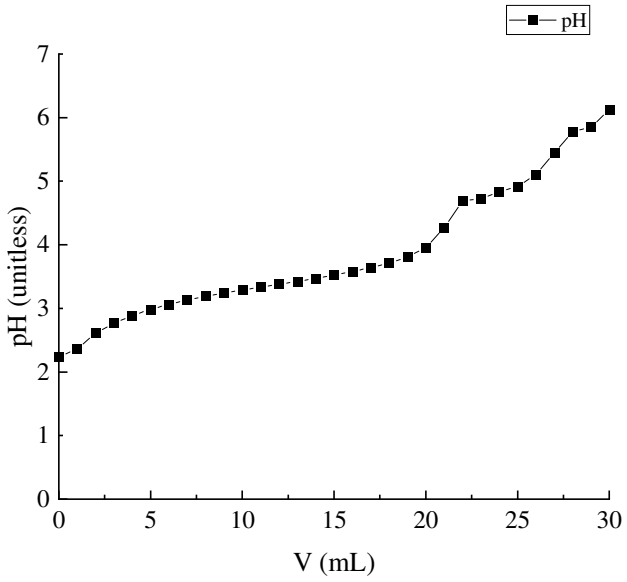

Figure 4.32: The pH of the binary metal salt solution by slowly adding 30mL of 0.1213 M of NaOH (pH=12) throughout 3 hours.

The derivative of pH with respect to the volume of base added to the trinary metal salt solution is shown in Figure 4.33. The initial colour of the binary metal salt solution was light yellow, then the addition of base turned the binary metal salt solution into dark yellow, followed by orange and eventually, a brown colloid is produced. The first minima are reached after the addition of approximately 10 mL of base. The second stage starts after a brown solution is produced, while the change of pH with respect to the base injected increases. Fine black magnetite particles were precipitated out first and then later (pH>4.2) the boehmite nanosheets form later as a white colloid. The colour of binary metal co-precipitation before and after the autoclave process was brown and

pinkish hue, respectively. These peaks in Figure 4.33 show that magnetite completely precipitated out first (pH<4.2) and boehmite precipitates when pH>4.2.

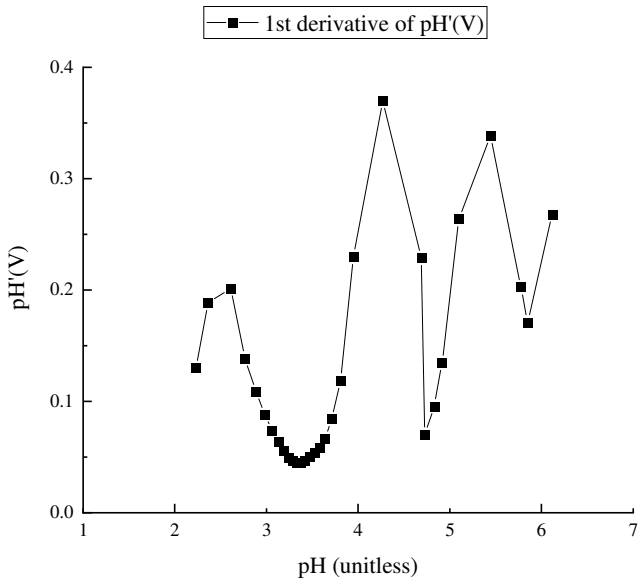

Figure 4.33: The change of pH with respect to base addition.

Compared to the direct deposition of magnetite nanoparticles on both boehmite and TAN nanosheets (Figure 4.21 and Figure 4.25 respectively), it was more challenging to find magnetite nanoparticles using TEM for binary metal salts co-precipitation on both boehmite and TAN nanosheets. The EDS analysis from Figure 4.30 shows that the iron peak intensity is much lower than that of the direct deposition counterpart shown in Figure 4.22. Since the magnetite nanoparticles were first precipitated, the boehmite nanosheet formation encapsulated the magnetite nanoparticles.

4.3.7 TEM and EDS observations for COSYN-MNP-TAN

Figure 4.34 shows a broad view of co-precipitated and co-calcined iron oxide-TAN complex. However, higher magnification image illustrates that very few magnetite nanoparticles were observed in Figure 4.35. The iron oxide nanoparticles in Figure 4.35 are hard to identify between static background noise. Since the iron oxides nanoparticles are not distinguishable, the statistical analysis was not conducted.

The aluminum and oxygen signal peaks in Figure 4.36 confirm that aluminum oxide is present in the sampling area. Also the weak iron signal indicates that the amount of iron oxide is extremely low in this segment of Figure 4.34, which is in agreement with the observation made in Figure 4.35. The darker sections of Figure 4.34 were not examined. It is possible that iron aggregated in these areas.

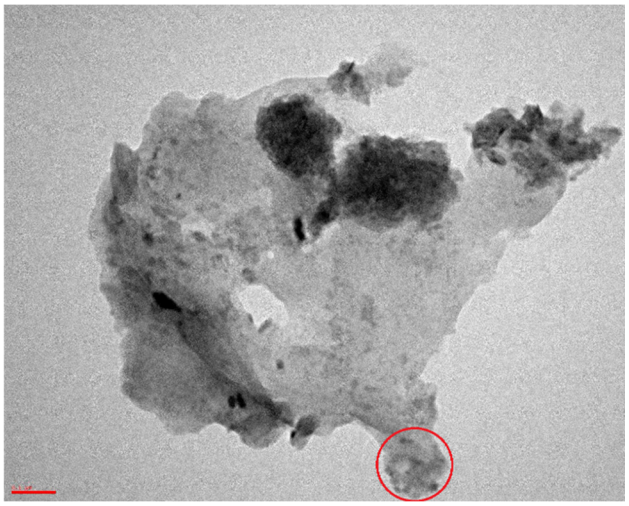

Figure 4.34: A TEM image of COSYN-MNP-TAN. The red circle is where the EDS scan was conducted. The red scale bar is 0.1 µm.

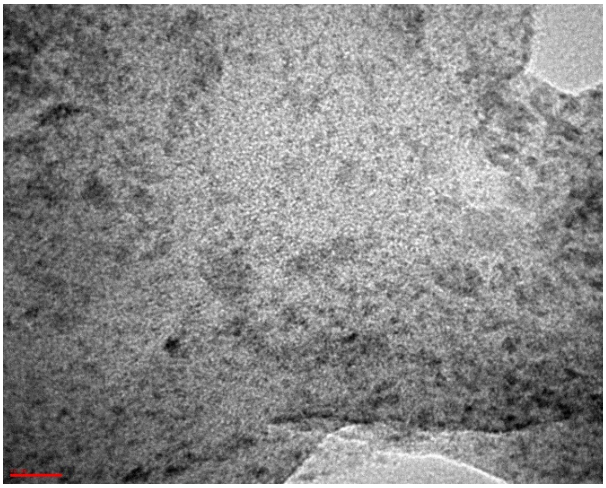

Figure 4.35: A zoomed-in view of the red circle in Figure 4.34. The red scale bar is 20 nm.

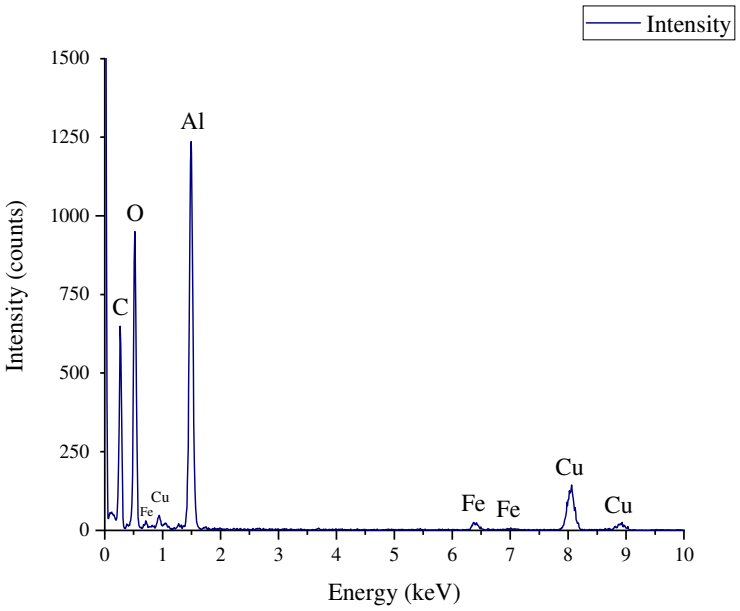

Figure 4.36: The EDS analysis of Figure 4.35.

4.3.8 TEM and EDS observations of 5% wt. Fe_3O_4 deposited on kaolinite (MNP-Kao)

The distribution of magnetite nanoparticle clusters deposited on kaolinite nanosheets presented in Figure 4.37 is much less aggregated compared to the boehmite nanosheet and TAN batches in Figure 4.21 and Figure 4.29 respectively. The higher magnification image in Figure 4.38 reveals that the orientation of these magnetite nanoparticles is different from those deposited on boehmite nanosheet and TAN (Figure 4.21, Figure 4.25 and Figure 4.29). For example, oval shaped particles were observed, also square and rectangular nanoparticles are found in Figure 4.38.

A stark difference is that a cluster of nanoparticles is located inside the kaolinite nanosheet surface. This is different from the boehmite nanosheets and TAN where they accumulated on the edges or vertices of the nanosheets. Kaolinite surfaces have different charge distributions compared to boehmite nanosheets and TAN since kaolinite has two silicon atoms between the four hydroxyl groups in its structure[209].

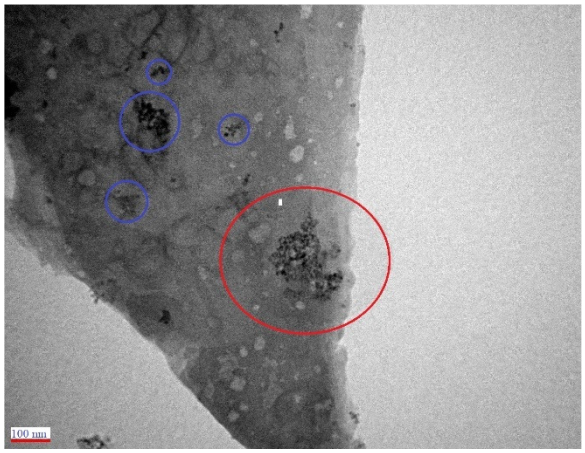

Figure 4.37: Clusters of MNP on kaolinite nanosheet as indicated by the blue circles. The red circle is where the EDS analysis conducted. The red scale bar is 0.1 μm.

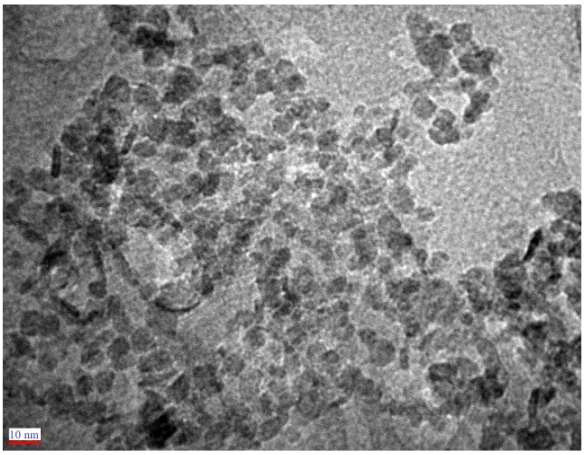

Figure 4.38: A segment view of Figure 4.37. The orientation of the magnetite nanoparticle is different on kaolinite compared to boehmite nanosheet and TAN as some of the particles are rectangular and not circular. The red scale bar is 10 nm.

The EDS analysis in Figure 4.39 shows that iron was present. The silicon peak confirms that the substrate is kaolinite rather than boehmite or TAN. The oxygen peak along with aluminum, silicon and iron peaks proves that some type of aluminum, silicon and iron oxide are present in the area of study. Both CTAB and PVP-10 surfactants have a polymer carbon chain that was present in the magnetite nanoparticle and kaolinite colloid, respectively, during the deposition process. The copper peak is from the TEM matrix grid slide.

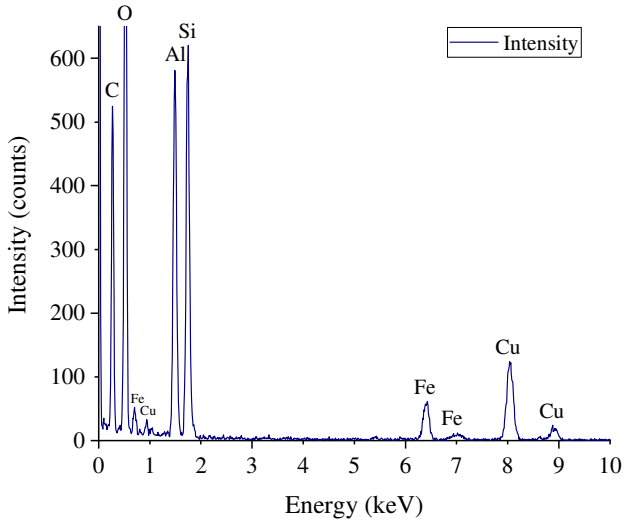

Figure 4.39: EDS analysis of Figure 4.38. The copper peak in the TEM slide grid.

A sample size of 84 particles were selected to perform a statistical analysis of the particles in the selected area marked by the red circle in Figure 4.37. The average, standard deviation, minimum and maximum diameter of the nanoparticles are 5.9, 2.2, 2.1 and 13.9 nm respectively. From Figure 4.40, the vast majority of nanoparticles have diameter greater than 5 nm with a noticeable minority of nanoparticles greater than 10 nm.

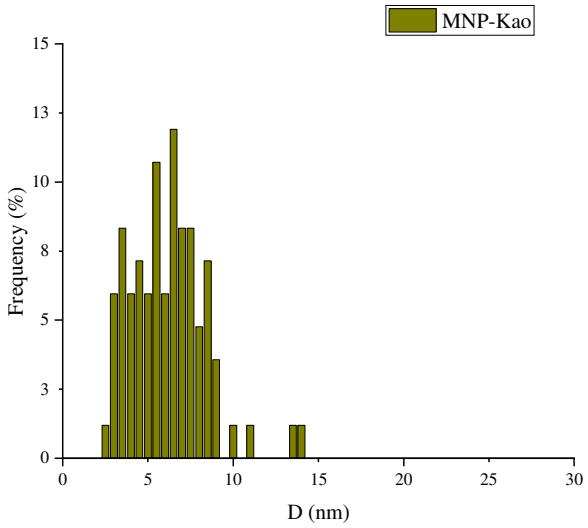

Figure 4.40: Length and diameter distribution for Figure 4.38.

4.3.9 TEM and EDS observations of 5% wt. Fe_3O_4 deposited on kaolinite calcined (MNP-Kao-calcined)

Figure 4.41 shows the image of magnetite nanoparticles deposited on kaolinite nanosheet and calcinated. The nanoparticles were found to distribute inside the nanosheet surface rather than on the substrate perimeter typically found in boehmite (Figure 4.21). This observation follows the same trend before the calcination step shown in Figure 4.38. The darker shade in Figure 4.41 shows that multiple layers of kaolinite are stacked beneath the top deposition layer. A noticeable difference before and after the calcination of the substrate is the disappearance of surface structures (craters, grooves, ridges and valleys), which removes obstacles for nanoparticle translation motion. The kinetic energy for translation motion of the nanoparticles is supplied by thermal energy during the calcination process [210]. The consequence of these features results in smaller dispersed clusters of nanoparticles rather than a fewer cluster of large aggregated nanoparticles.

Upon further inspection of Figure 4.42, it was found that nanoparticles were either aggregated or coarsened together. The morphologies of the nanoparticles in this batch are of more irregular and asymmetrical shape upon post calcination (Figure 4.42). Whereas the morphologies from the

previous batch set are more geometrically ordered with nanoparticles composing of either circular or rectangular shapes before calcination (Figure 4.38).

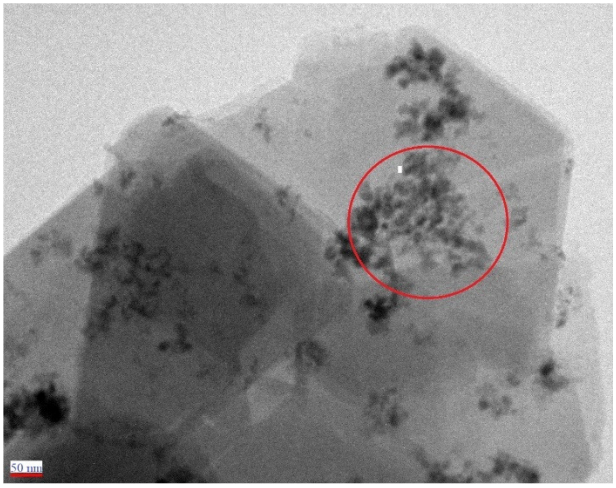

Figure 4.41: MNP-Kaolinite-calcined. The sample is calcined. The red circle is where the EDS analysis was conducted. The red scale bar is 50 nm.

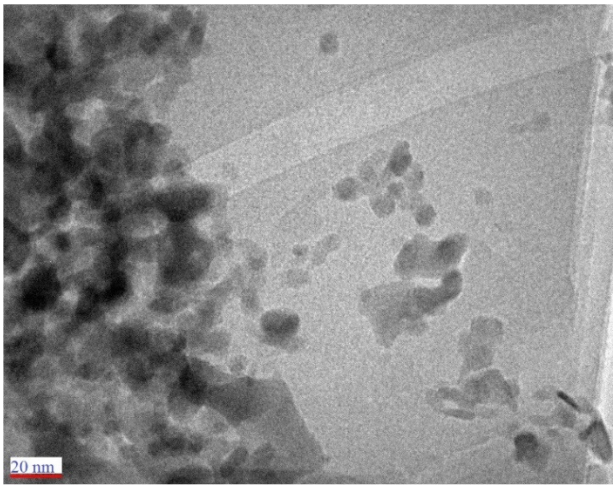

Figure 4.42: A segment view of Figure 4.41. The red scale bar is 20 nm.

Figure 4.43 depicts the EDS analysis of Figure 4.42. The combination of aluminum, silicon and oxygen peaks indicates the presence of kaolinite. The silicon peak is the unique signal that distinguishes kaolinite from boehmite and TAN, since boehmite and TAN do not have silicon in their composition. The signal peak of iron and oxygen pair confirms the presence of iron oxides. The carbon peak suggests coking residue from the thermal decomposition of PVP-10 surfactant during the calcination process.

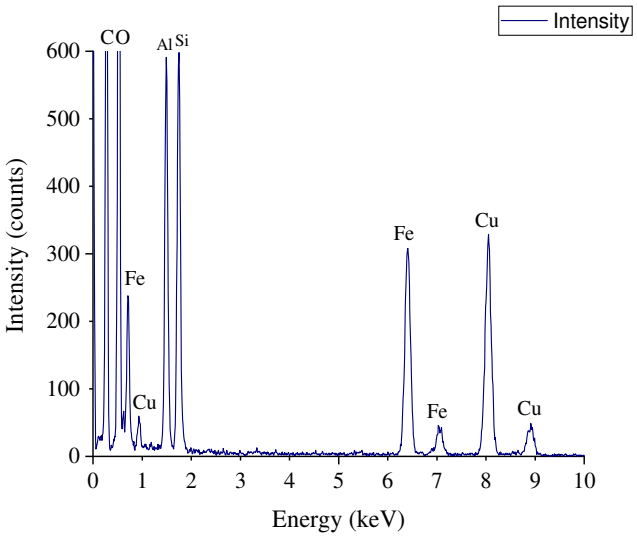

Figure 4.43: The EDS analysis of Figure 4.42.

The statistical analysis that was used on the non-calcined version of kaolinite was utilized for the calcined version. The sample size was 40 to conduct statistical analysis, and the results of average, standard deviation, minimum and maximum diameter of the nanoparticles are 9.7, 5.8, 4.2 and 28.7 nm respectively. Approximately 12 % of the sampled nanoparticles have diameters greater than 20 nm are shown in Figure 4.44. These larger nanoparticles are formed when multiple smaller nanoparticles coarsen together during the calcination process. The statistical analysis in Figure 4.43 demonstrates that nanoparticle coarsening phenomena definitely appear.

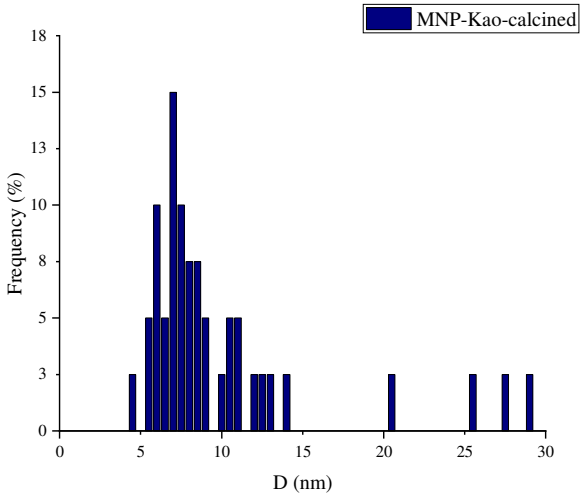

Figure 4.44: Length and diameter distribution for Figure 4.42.

4.3.10 XRD measurements

The XRD spectrum of the magnetite nanoparticles presented in Figure 4.45 from the present experiment closely resemble those in literature [133], [134]. Three types of iron oxides (magnetite, hematite and maghemite) were all detected in all the sample batches that were calcined (TAN batches) [211], where only magnetite peak is present without calcination process. Hematite and maghemite peaks were detected at approximately 32.973°, 35.675°, 50°, 54.054° [212]–[216] and 35°, 62.91° peak sets [217] respectively. This shows that magnetite has reacted with the oxygen component in the air into hematite and maghemite [218], [219] expressed in the reaction below Eq. (4.5);

$$4Fe_3O_4 + O_2 \rightarrow 6Fe_2O_3 \tag{4.5}$$

The unique characteristic peaks of the substrates were also detected. The boehmite characteristic peaks correspond to 13.68°, 31.579°, 38.095°, 49.473° [220], while the TAN characteristic peaks correspond to 31.7°, 45.56°, 67.04° [221] shown in Figure 4.46. The kaolinite signal was present for batches where kaolinite was the substrate for magnetite nanoparticle deposition, and the peak signals were 12.24° and 24.92° , in which the result was also reported in the literature [138]. Also, both leftover reactant and surfactant residuals were detected, and this observation matches the EDS analysis results.

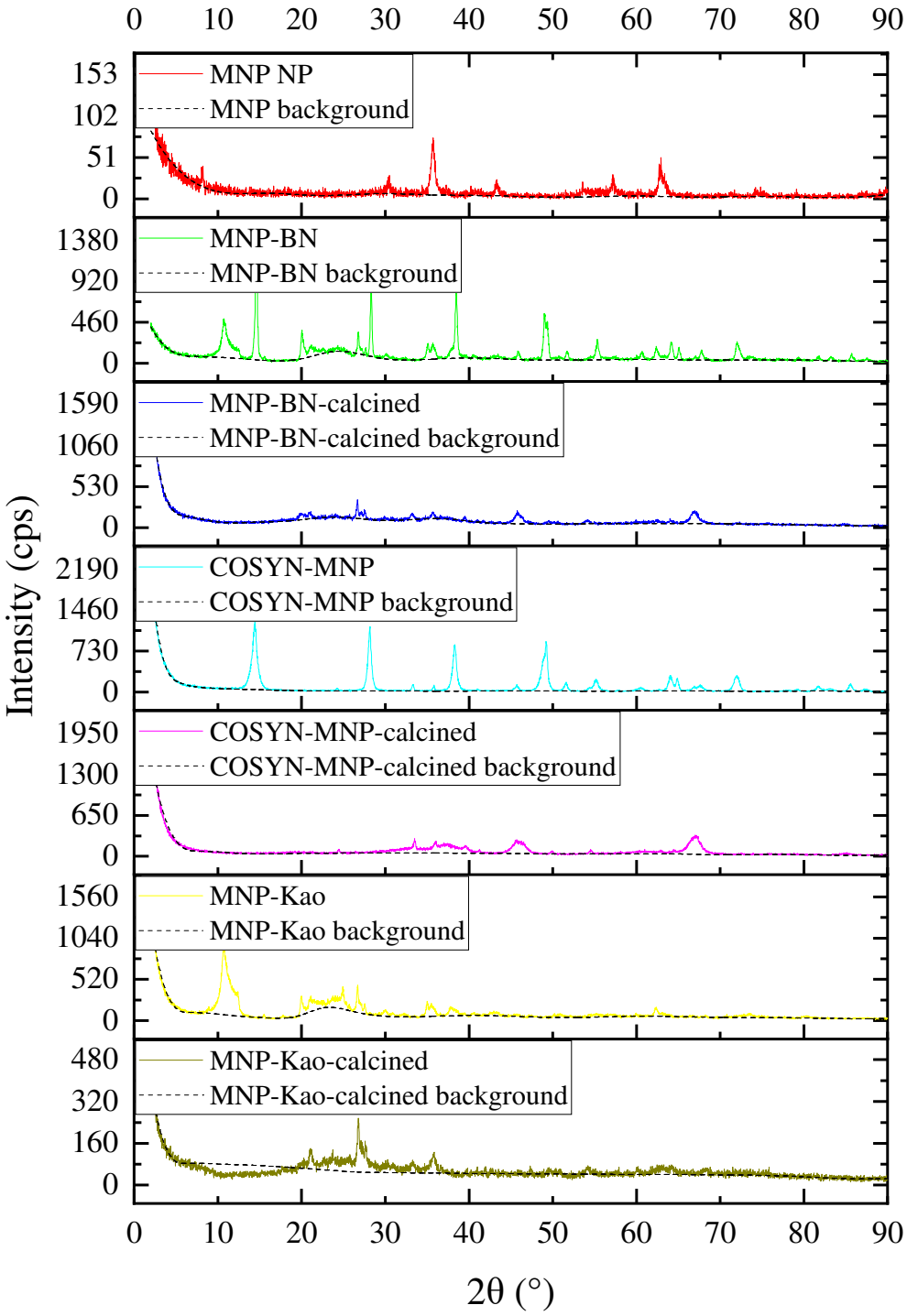

Figure 4.45: XRD spectrum of isolated individual magnetite nanoparticles and iron oxides deposited on six substrates.

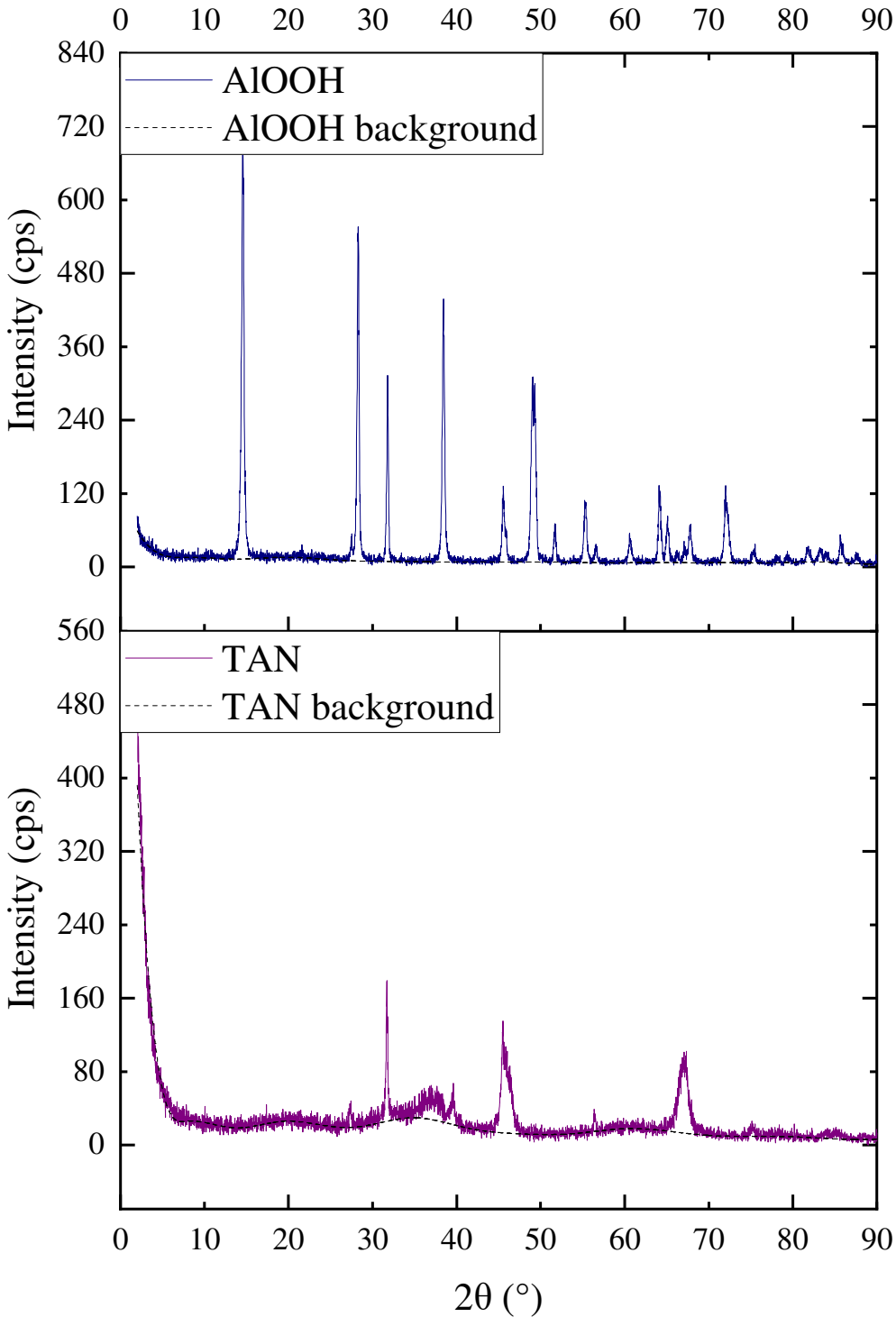

Figure 4.46: XRD spectrum of boehmite (γ-AlOOH) and twined alumina nanosheets (TAN).

4.4 Discussion Summary

The thickness of all three nanosheet substrates was less than 100 nm, and the length and width were in the micron range. Both circular and rectangular nanoparticle morphologies were detected for all cases. There was a higher occurrence of rectangular nanoparticles on kaolinite before calcination.

The average diameter of the nanoparticles is between 3.45 and 5.9 nm before calcination and the majority of the nanoparticles were less than 9.3 to 9.5 nm in diameter after calcination. The fraction nanoparticles having diameters less than 5 nm for MNP, MNP-BN and COSYN-MNP are 65, 41 and 81% of respectively. The sub 5 nm in diameter nanoparticles will affect the base growth mode of carbon nanotubes. The particles larger than 5 nm will have tip growth carbon nanotubes and detach from the surface of the catalysts. This would open up more space on the surface of the catalyst for CNT growth. MNP-BN, MNP-BN-calcined, COSYN-MNP and MNP-Kao batches are potential candidates for the continuous formation of CNTs from methane cracking on these supports.

When combined in the same synthesis vessel, iron nanoparticle and boehmite synthesis do not take place simultaneously, since iron and aluminum precipitate at different pHs. Magnetite nanoparticles precipitate first followed by boehmite and thus encapsulating the initial nanoparticle. EDS analysis shows that iron oxide compounds were embedded in the nanosheet.

XRD spectroscopy indicates that post calcination of magnetite nanoparticle at 600°C under ambient conditions oxidizes magnetite into hematite and maghemite. CNTs can be grown on magnetite, hematite or maghemite [222].

Iron nanoparticles remained on all substrates after ultrasonication prior to analysis indicating that they are physically bound to the substrates. It is suggested calcined substrates be tested as methane cracking catalysts to determine the extent of tip growth for the coarsened nanoparticles on these substrates. It is possible that the larger coarsened nanoparticles be released form the catalyst due to tip growth exposing the smaller sub 5 nm iron particles. This would permit tip growth on the substrate. The non calcined particles should also be tested as catalysts to determine if they are suitable for the base growth of CNTs and if coarsening occurs as the cracking reaction proceeds.

4.5 Conclusions

Magnetite nanoparticles were synthesized and deposited onto nanoplatelet supports made from aluminium oxides-based substrates (boehmite, TAN and kaolinite). The surfactant CTAB was added during the nanoparticle synthesis stage to prevent the nanoparticles from aggregating. SEM and TEM with in-situ EDS were used to characterize the nanoparticle size, morphology, degree of aggregation and elemental composition. XRD spectroscopy was used to verify and determine the catalyst-substrate material composition. Statistical analysis of the TEM images was conducted by using the ImageJ analysis software. The area and perimeter of each nanoparticle was measured manually due to excessive static background noise.

The average diameter of these nanoparticles was less than 5 nm for MNP, MNP-BN and COSYN-MNP respectively. The co-synthesis (COSYN-MNP) batch of the magnetite nanoparticles without calcination had the smallest magnetite nanoparticle diameters where 40% were less than 5 nm in diameter. The sub 5 nm in diameter is a critical criterion met for base growth mode of CNTs. Nanoparticle coarsening occurred when it has calcined at 600°C for 4 hours. XRD spectroscopy revealed that magnetite had oxidized into hematite and maghemite after calcination. However, CNTs can be grown on magnetite, hematite or maghemite. The magnetite nanoparticles deposited on boehmite are located on the perimeter of the boehmite nanosheet due to the charge distribution of boehmite nanosheet.

Iron nanoparticles were found to remain on all substrates after ultrasonication. It is suggested that both non calcined and calcined catalysts be tested in methane cracking to determine the effect of iron nanoparticle distribution on the tip growth of CNTs at the surface of the nanoplatelet supports.

Chapter 5 Fenton degradation of methyl orange using iron nanoparticles on nanoplatelet supported catalysts.

Abstract

Heterogenous iron oxide(s) nanoparticle catalyst deposited on alumina oxide-based substrates were used in the Fenton degradation reaction of methyl orange aiming at evaluating catalyst performance. The duration of each test run was set to be 2 hours with an approximate 15 minutes interval between each sampling. The catalyst is the iron oxide(s) nanoparticles and the substrates are boehmite, TAN and kaolinite. The test results demonstrated that the stand-alone magnetite nanoparticles with hydrogen peroxide had the best performance in terms of the degradation rate. In contrast, the calcined batches of iron oxide(s) catalyst-substrate complex had a low degradation rate. Boehmite nanosheet, TAN and kaolinite platelet substrates were tested to verify if the substrates possess catalytic activity and only boehmite nanosheets were found to react with methyl orange. Magnetite nanoparticles deposited on kaolinite could be recycled to catalyze the degradation of methyl orange. The results show that magnetite nanoparticles were produced without calcination and that other forms of iron oxides such as hematite and maghemite were produced with calcination.

5.1 Introduction

The Fenton reaction was demonstrated to be an effective reaction for the cleanup of textile dyes. The Fenton degradation reaction of dyes catalyzed by magnetite nanoparticles is also used as method to benchmark catalyst performance. The kinetics of degradation of dyes can be measured and compared with other catalysts [223].

The advantages of using heterogeneous rather than homogenous catalysts for the Fenton reaction is that no sludge is produced, the reaction is operated at near-neutral pH and catalysts can be recovered. These reactions are based on the formation of hydroxyl radicals, which are capable of oxidizing large organic molecules into smaller molecules, as well as mineralizing and converting organic compounds into water and carbon dioxide [224]. Traditional Fenton reagent ($Fe^{2+}(aq)$ in H_2O_2) is reactive when the pH<4; this relatively low pH is too acidic for many applications. Iron-based catalyst mixed with hydrogen peroxide, however, can effectively oxidize organic compounds at near-neutral pH.

The most advantageous features of using an iron-based material as a heterogeneous catalyst deposited on a substrate is that iron is magnetic, which makes catalyst recovery much easier compared to non-magnetic materials. There are many studies of iron catalyst deposited on zeolite supports for the degradation of organic compounds [225]–[227].

In this chapter, the iron oxide and supported catalysts synthesized in Chapter 4 were tested to evaluate their catalytic performance by degrading methyl orange using the Fenton reagent comparing their degradation rate.

5.2 Equipment

The fabrication of both substrate and magnetite nanoparticle catalysts to be used for the Fenton degradation reaction of methyl orange as described in Chapters 3 and 4, respectively.

The absorption tests were monitored using by spectrometer from UV to infrared spectrum. The spectrophotometer is a model 4201/120 from Nahita (Spain). The wavelength of the spectrometer

is set to the maximum absorption wavelength of methyl orange at 464 nm [228]. Both large particles and substrates were filtered out by sterile 33 mm in diameter and 0.22 μm of pore size PVDF membrane syringe filter before undergoing absorption test in the spectrophotometer.

5.3 Materials

Methyl orange powder (Fisher Chemical) and Millex-GV Filter, 0.22 μm, PVDF, 13 mm, ethylene oxide sterilized (Darmstadt, Germany) were purchased from Fisher Scientific. The concentration of methyl orange to be degraded was selected from the literature [225]. A 250 mL of 1 mM methyl orange stock solution was first prepared and then diluted to obtain the required sample concentration. A small cylindrical container was used to mix the reaction tubes. This provided mixing without the use of a magnetic stirrer that would promote iron catalyst aggregation.

5.4 Procedure

The methyl orange reactant concentration was selected based on the work of Lin *et al.* [225]. All of the iron oxide nanoparticle batches were tested to benchmark their catalyst performance. The individual substrate (boehmite, TAN and kaolinite) were also tested to check if the substrate itself was a catalyst. A blank run just with hydrogen peroxide was also performed. The concentration of methyl orange and hydrogen peroxide, and the amount of catalyst were kept constant. All of degradation reactions were carried out at neutral pH of 6.9. The Fenton degradation reaction of methyl orange was conducted through these following steps:

1) 45 mL of DI water, 1.35 mL of 10% v/v H_2O_2 and 100 μL of 1 mM of methyl orange was added into a 50 mL centrifuge tube;
2) The newly diluted methyl orange solution was then agitated in a vortex mixer to ensure it was well mixed in the centrifuge tube;

3) Approximately 0.01 g of magnetite nanoparticles were added into 45mL of DI water, 1.35 mL of 10% v/v H_2O_2 and 100 µL of 1 mM methyl orange dye.

    a. To have 0.01 g of iron oxide(s) nanoparticles present in the reaction vessel; 0.2 g of 5% wt. iron oxide(s) nanoparticle-substrate complex were added into the centrifuge tube.

4) The centrifuge tube was placed radially in a cylindrical metal container, and the container rotated along its axis;

5) A 1 mL sample of the reaction mixture and filtered by a syringe filter before placing the sample in the plastic cuvettes and analyzed.

6) After the degradation reaction, the magnetite nano-catalyst was recovered by centrifugation and then underwent the decantation process.

Vertical mixing of the reaction tube by tumbling was required to ensure that magnetite nanoparticles were well mixed in the solution. Vertical mixing prevents the catalyst-substrate complex from sinking to the bottom of the centrifuge tube during the mixing stage between each time interval.

The catalysts where the reaction proceeded were recycled to test their reusability. The used catalysts were decanted five times with 50 mL of DI water through the centrifuge process and were refilled with fresh DI water between each decantation step.

5.5 Results and Discussion

5.5.1 Degradation rate and mechanism of methyl orange

The degradation *D* (%) of methyl orange is expressed below in Eq. (5.1);

$$D(\%) = \frac{A(t)}{A_0} \tag{5.1}$$

Where A_0 and *A(t)* are the absorbance of methyl orange solution at the initial and, at a specific time elapsed in the run. A_b is the absorbance of a blank sample containing H_2O_2.

The absorption of hydrogen peroxide (H_2O_2) on an active site of Fe (III) is expressed in Eq. 5.2). The catalytic activity of magnetite nanoparticles is related to the catalyst surface to convert H_2O_2 into free radicals ($\cdot OH$) [229]. Under acidic conditions, the mechanism of H_2O_2 decomposition on the surface of magnetite nanoparticle may involve adsorption on the active sites of Fe^{2+} and Fe^{3+}. The adsorption and formation of a complex between surface Fe (III) site and H_2O_2 (Eq. (5.3) can occur, allowing the production of HO_2 that can thereafter react to produce oxygen gas (Eq. 5.4). However, the rates of radical formation on Fe(III) are slower compared to their Fe(II) counterpart [230] shown in Eq (5.5).

$$Fe^{III} + H_2O_2 \rightarrow Fe^{III}H_2O_2 \tag{5.2}$$

$$Fe^{III}H_2O_2 \rightarrow Fe^{II} + \cdot HO_2 + H^+ \tag{5.3}$$

$$Fe^{III} + \cdot HO_2 \rightarrow Fe^{II} + O_2 + H^+ \tag{5.4}$$

$$Fe^{II} + H_2O_2 \rightarrow Fe^{III} + \cdot OH + OH^- \tag{5.5}$$

5.5.2 Fenton degradation reaction of methyl orange

Figure 5.1, Figure 5.2, Figure 5.3 and Figure 5.4 shows the degradation rate of the Fenton degradation reaction of methyl orange through the span of 3 hours with the incident beam wavelength of 464 nm. It was observed that the degradation *D* is fastest in the first 25 minutes followed by a gradually slowing down. The degradation rate is clearly a reflection of reaction rate as it has the fastest concentration change with respect to time. Factors that contribute to fluctuation are due to catalyst removal during the absorption sampling test period.

The individual iron nanoparticles batch has the highest degradation performance (Figure 5.1), MNP without hydrogen peroxide had the second fastest reaction and whereas in all of the calcined batches have no reaction as indicated in Figure 5.4. The non-calcined batch had a moderate

degradation performance and boehmite is the only substrate that reacted as illustrated in Figure 5.3. Where in contrast, the post calcination process batch (MNP-TAN, COSYN-MNP-TAN and MNP-Kao-calcined) and individual substrates almost have no reaction at all as shown in Figure 5.2. Based on the XRD spectroscopy analysis in Chapter 4, the post calcination of magnetite nanoparticle deposited on any of the three listed substrates and co-precipitation batches shows the majority of magnetite nanoparticles oxidizes into Fe (III) oxide allotropes (hematite and maghemite). Both hematite and maghemite cannot catalyze the Fenton reaction shown in Figure 5.2 and Figure 5.3.

An interesting observation is the stark difference in degradation rate between MNP-BN in Figure 5.4 and COSYN+MNP revealed in Figure 5.3. From Chapter 4, it was shown that the magnetite nanoparticle precipitates first followed by the boehmite nanosheet. The accessibility to the nanoparticle is greatly reduced due to the presence of the co-synthesized boehmite nanosheet. As a consequence, the opportunity for the redox reaction to proceed is reduced and this effect is illustrated in Figure 5.2.

The three types of substrates were individually tested with the same amount of hydrogen peroxide. There was no reaction for TAN and the ultrasonicated kaolinite. Adding hydrogen peroxide into the methyl orange solution results in the performance of the Fenton reaction shown between the MNP-Kao and the MNP-BN. It is interesting to note that boehmite with hydrogen peroxide (Figure 5.3) indicates almost the same performance in Fenton reaction as the MNP without hydrogen peroxide. A possible explanation is that there were residual CTAB and sodium hydroxide contaminates leftover in the boehmite nanosheets.

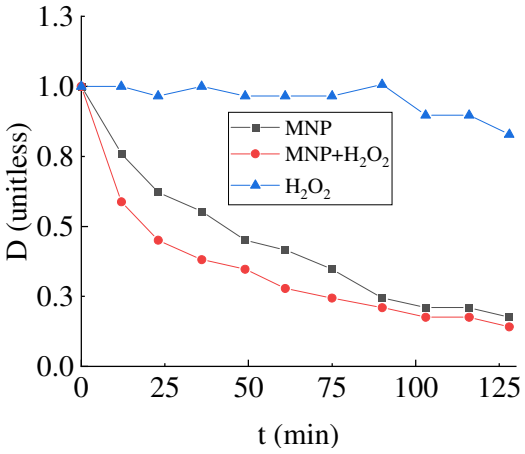

Figure 5.1: Degradation rate of Fenton reaction of methyl orange using isolated magnetite nanoparticle batch through the span of 3 hours. The incident beam wavelength is 464 nm.

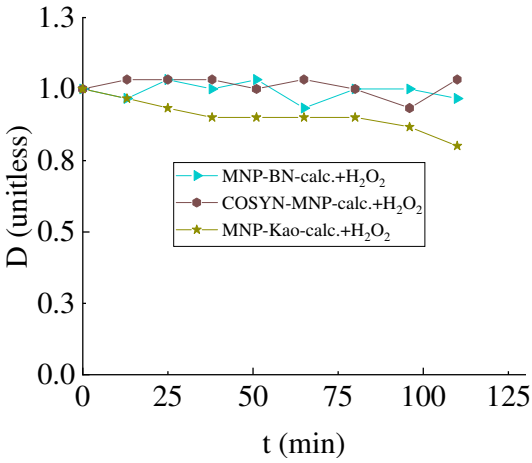

Figure 5.2: Degradation rate of Fenton reaction of methyl orange using calcined magnetite nanoparticle on substrate batch through the span of 3 hours. The incident beam wavelength is 464 nm.

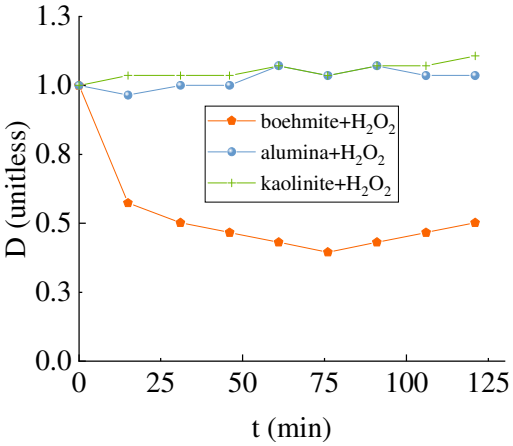

Figure 5.3: Degradation rate of Fenton reaction of methyl orange using isolated substrate batch through the span of 3 hours. The incident beam wavelength is 464nm.

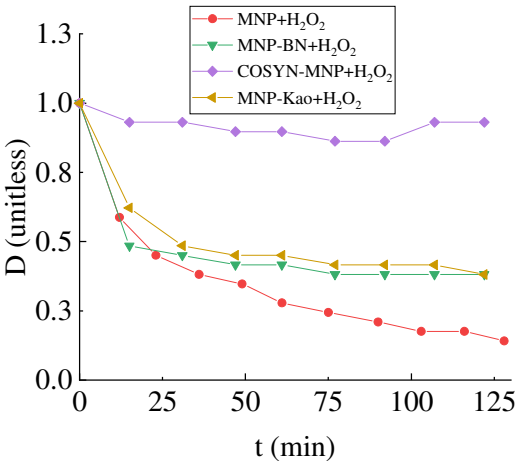

Figure 5.4: Degradation rate of Fenton reaction of methyl orange using non-calcined magnetite nanoparticle on substrate through the span of 3 hours. The incident beam wavelength is 464nm.

5.5.3 Recycling

Reactive catalysts were selected to undergo decantation for performance retest. The same conditions were rerun again using the same catalysts. The performance of the catalyst dropped drastically after the first run. A possible reason for such a result is that the surface of the catalyst is oxidized and needs to be reduced before rerunning the Fenton degradation reaction of methyl orange.

The concentration change of 2nd and 3rd Fenton degradation reactions of methyl orange catalyzed by magnetite nanoparticles deposited on the substrate dropped significantly, as demonstrated in Figure 5.5 and Figure 5.6. However, MNP-Kao has the best performance after the first run. Figure 5.5 and Figure 5.6 indicate that almost all of the catalysts lose their degradation capability after the first run. A good example is associated with the catalysis performance of the MNP-Kao, wherein the degradation rate nearly remains constant. All of the recycled catalysts illustrate that the degradation rate fluctuates throughout the three-hour span.

Recovery of the catalyst activity also depends on the treatment of catalyst particles after the reaction run. For instance, Istratie et al. [231] using iron oxide powder was able to degrade methyl orange in 4 consecutive runs with a slight drop in adsorption capacity after each run. The reason for this result may be that their desorption technique consists of washing the spent magnetite and maghemite nano-catalyst with aqueous solution of ethanol (anhydrous ethanol: water = 2:1), consequently their desorption efficiency gradually decreased from 91% to 60% after 4 cycles. For another example, Xiao et al. [232] in their study on Fenton oxidation of methyl orange on magnetic carbon materials concluded that adsorption capacity can be increased with increasing microporosity in carbon supports while the regeneration efficiency increased with increasing mesoporosity. The absorption capacity of Fe_2O_3 drops from 97 mg/g to 65 mg/g after 6 regeneration cycles.

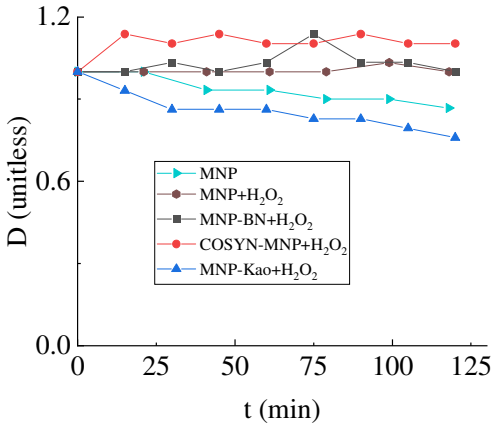

Figure 5.5: 2nd regeneration of Fenton reaction run of methyl orange of individual magnetite nanoparticles and non-calcined batch through the span 3 hours comparison. The incident beam wavelength is 464nm.

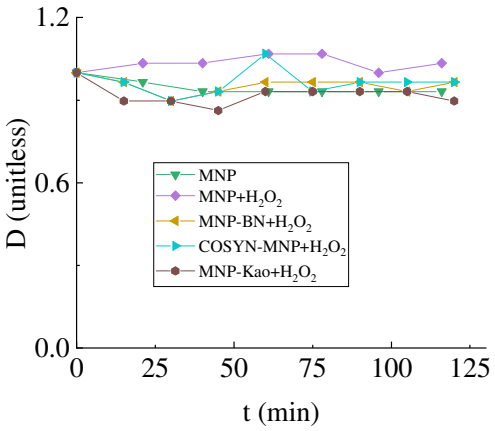

Figure 5.6: 3rd regeneration of Fenton reaction run of methyl orange of individual magnetite nanoparticles and non-calcined batch through the span 3 hours comparison. The incident beam wavelength is 464nm.

5.6 Conclusions

It was found that the unsupported magnetite nanoparticles with hydrogen peroxide had the best catalyst performance in terms of degradation rate. The catalyst with the highest potential for recycling was MNP-Kao.

All of the calcined batches did not show reaction except for the MNP-Kao-calcined batch. The process of calcination results in oxidizing magnetite into hematite and maghemite, as detected by XRD spectroscopy in Chapter 4. Based on Chapter 4, it was demonstrated that the magnetite nanoparticles precipitate first followed by boehmite precipitation, and therefore reducing access to the newly formed magnetite nanoparticles.

The three types of substrates, along with hydrogen peroxide, were individually tested with the dilute methyl orange sample to check if the substrate was a catalyst. All of the substrates did not react with the dilute methyl orange except for boehmite nanosheets.

Chapter 6: Conclusions and recommendations

6.1 Conclusions

Magnetite nanoparticles were synthesized and deposited onto nanoplatelet supports made from aluminium oxides-based substrates (boehmite, TAN and kaolinite). The surfactant CTAB was added during the nanoparticle synthesis stage to prevent the nanoparticles from aggregating. SEM and TEM with in-situ EDS were used to characterize the nanoparticle size, morphology, degree of aggregation and elemental composition. XRD spectroscopy was used to verify and determine the catalyst-substrate material composition. Statistical analysis of the TEM images was conducted by using the ImageJ analysis software. The area and perimeter of each nanoparticle was measured manually due to excessive static background noise.

The average diameter of these nanoparticles was found between 3.45 and 5.9 nm before calcination and the majority of the nanoparticles were less than 9.3 to 9.5 nm in diameter for post calcination. 65, 41 and 81% of the nanoparticles have diameter less than 5 nm for MNP, MNP-BN and COSYN-MNP respectively. The co-synthesis (COSYN-MNP) batch of the magnetite nanoparticles without calcination had the smallest magnetite nanoparticle diameters where 40% were less than 5 nm in diameter. The sub 5 nm in diameter is a critical criterion met for base growth mode of CNTs. Another advantage of co-synthesising nanoparticle and substrate is that the growth of the substrate also controls the growth of nanoparticles as well. Nanoparticle coarsening occurred when it has calcined at 600°C for 4 hours. XRD spectroscopy revealed that magnetite had oxidized into hematite and maghemite after calcination. However, CNTs can be grown on magnetite, hematite or maghemite nanoparticles. The magnetite nanoparticles deposited on boehmite are located on the perimeter of the boehmite nanosheet due to the charge distribution of boehmite nanosheet. Iron nanoparticles were found to remain on all substrates after ultrasonication. It is suggested that both non calcined and calcined catalysts be tested in methane cracking to determine the effect of iron nanoparticle distribution on the tip growth of CNTs at the surface of the nanoplatelet supports.

Work was also performed to produce nanoplatelets from kaolinite by delamination. The results indicate that increasing ultrasonication power without the presence of surfactants breaks-up large

kaolinite particles into smaller ones. The introduction of a surfactant significantly alters the orientation and the distribution of the delaminated kaolinite. Adding CTAB into 50 % wt. urea solution produces single or multilayer kaolinite with circular vertices. There are much fewer fine particles deposited on the delaminated kaolinite layer compared to their non-surfactant counterparts. The distance between each individual platelet increases considerably when the solubility limit of CTAB is reached. Fine kaolinite particles are almost nonexistent with the moderate separation distance between each platelet when PVP K30 is used. The geometric morphology of the platelets is different compared to the CTAB batch, as the vertices are much sharper. The PVP of different molar mass had a different outcome; the geometric orientation of the platelets was circular and had a "dish" like structure. The distance between each platelet is moderately close with fine kaolinite particles on the top of the large platelet. A charged surfactant was also tested; the utilization of sodium cholate has resulted between CTAB and PVP K30. Utilizing equal mass amounts of surfactant in the same urea concentration assemble elongated "bowl" and "dish" like structures with numerous fragmented fine particles scattered on top of larger platelets.

The final experimental set was to determine if more substantial amounts of kaolinite can be delaminated at the same surfactant concentration when more kaolinite was added into the same urea-surfactant solution; higher delaminated kaolinite occurrence, a higher degree of aggregation, much more fine particle fragments and the decreasing separation distance between each platelet.

It can be concluded that the presence of surfactant has positive effects on kaolinite delamination. The kaolinite is delaminated to a greater extent when higher ultrasonication power and concentration of urea and surfactant are used. Kaolinite is most delaminated when the concentration of urea and surfactant is near it is solubility limit and at the highest sonication power.

The performance of the catalysts produced in this work was determined by the degradation of methyl orange via the Fenton reaction. It was found that the unsupported magnetite nanoparticles with hydrogen peroxide had the best catalyst performance in terms of degradation rate. The best reusable set was identified as MNP-Kao batch, which also had a minor activity on the degradation rate after recycling.

All of the calcined batches did not show reaction except for the MNP-Kao-calcined batch. The process of calcination results in oxidizing magnetite into hematite and maghemite, as detected by

XRD spectroscopy. These tests show that hematite and maghemite do not have catalysis capability for the Fenton reaction.

This work was successful in demonstrating that sub 5 nm iron nanoparticles, with the potential to lead to base growth CNTs, can be made and deposited on open nanoplatelet substrates. All metal oxides produced in this work; magnetite, hematite and maghemite can be used to synthesize CNTs. These catalysts have the proper characteristics to be useful in methane cracking where hydrogen and solid carbon can be produced without the release of carbon dioxide.

6.2 Recommendations

1) The MNP, MNP-BN, MNP-Kao and COSYN-MNP catalysts should be tested for direct methane cracking reaction to verify if the base growth mode of carbon nanotubes (CNTs) can be achieved.

2) A direct deposition of magnetite nanoparticle on pre-calcinated TAN should to be carried out.

3) Study the effect of the elongation of CNTs during methane cracking, its shear strength and the work of adhesion strength between nanoparticle and substrate on variation of CNT growth modes.

4) Study CNT nucleation and growth mechanisms including base and tip growth on specific catalyst surfaces in terms of thermodynamics, kinetics combined with density functional theory (DFT) calculations.

References

[1] T. Nejat Veziroğlu, “Hydrogen technology for energy needs of human settlements,” *Int. J. Hydrogen Energy*, vol. 12, no. 2, pp. 99–129, 1987.

[2] D. J. Wuebbles and A. K. Jain, “Concerns about climate change and the role of fossil fuel use,” *Fuel Process. Technol.*, vol. 71, no. 1–3, pp. 99–119, 2001.

[3] T. J. Crowley, “Causes of Climate Change Over the Past 1000 Years,” *Science (80-.).*, vol. 289, no. 5477, pp. 270–277, Jul. 2000.

[4] T. R. Karl, “Modern Global Climate Change,” *Science (80-.).*, vol. 302, no. 5651, pp. 1719–1723, Dec. 2003.

[5] J. T. Overpeck and J. E. Cole, “Abrupt Change in Earth’s Climate System,” *Annu. Rev. Environ. Resour.*, vol. 31, no. 1, pp. 1–31, Nov. 2006.

[6] H. Ritchie and M. Roser, “CO_2 and Greenhouse Gas Emissions,” *OurWorldInData.org*, 2017. [Online]. Available: https://ourworldindata.org/co2-and-other-greenhouse-gas-emissions. [Accessed: 28-Apr-2020].

[7] J. Alcalde *et al.*, “Estimating geological CO2 storage security to deliver on climate mitigation,” *Nat. Commun.*, vol. 9, no. 1, 2018.

[8] G. D. Berry, A. D. Pasternak, G. D. Rambach, J. R. Smith, and R. N. Schock, “Hydrogen as a future transportation fuel,” *Energy*, vol. 21, no. 4, pp. 289–303, 1996.

[9] G. J. Stiegel and M. Ramezan, “Hydrogen from coal gasification: An economical pathway to a sustainable energy future,” *Int. J. Coal Geol.*, vol. 65, no. 3–4, pp. 173–190, 2006.

[10] J. H. Lunsford, “Catalytic conversion of methane to more useful chemicals and fuels: A challenge for the 21st century,” *Catal. Today*, vol. 63, no. 2–4, pp. 165–174, 2000.

[11] A. Holmen, “Direct conversion of methane to fuels and chemicals,” *Catal. Today*, vol. 142, no. 1–2, pp. 2–8, 2009.

[12] J. R. Rostrup-Nielsen, “Catalysis and large-scale conversion of natural gas,” *Catal. Today*,

vol. 21, no. 2–3, pp. 257–267, 1994.

[13] DOE, “What is the volume of world natural gas reserves?,” *EIA*, 2020. [Online]. Available: https://www.eia.gov/tools/faqs/faq.php?id=52&t=8. [Accessed: 29-Apr-2020].

[14] BP, “BP Statistical Review of World Energy,” *Stat. Rev. World Energy*, no. 67, pp. 1–56, 2018.

[15] M. Etminan, G. Myhre, E. J. Highwood, and K. P. Shine, “Radiative forcing of carbon dioxide, methane, and nitrous oxide: A significant revision of the methane radiative forcing,” *Geophys. Res. Lett.*, vol. 43, no. 24, pp. 12,614-12,623, 2016.

[16] A. Portnov, S. Vadakkepuliyambatta, J. Mienert, and A. Hubbard, “Ice-sheet-driven methane storage and release in the Arctic,” *Nat. Commun.*, vol. 7, no. 1, p. 10314, Apr. 2016.

[17] I. Martínez, M. C. Romano, J. R. Fernández, P. Chiesa, R. Murillo, and J. C. Abanades, “Process design of a hydrogen production plant from natural gas with CO2capture based on a novel Ca/Cu chemical loop,” *Appl. Energy*, vol. 114, pp. 192–208, 2014.

[18] B. Gaudernack and S. Lynum, “Hydrogen from natural gas without release of CO2to the atmosphere,” *Int. J. Hydrogen Energy*, vol. 23, no. 12, pp. 1087–1093, 1998.

[19] M. Serban, M. A. Lewis, C. L. Marshall, and R. D. Doctor, “Hydrogen production by direct contact pyrolysis of natural gas,” *Energy and Fuels*, vol. 17, no. 3, pp. 705–713, 2003.

[20] N. Z. Muradov, “CO2-Free Production of Hydrogen by Catalytic Pyrolysis of Hydrocarbon Fuel,” *Energy & Fuels*, vol. 12, no. 1, pp. 41–48, 1998.

[21] J. Fan and L. Zhu, “Performance analysis of a feasible technology for power and high-purity hydrogen production driven by methane fuel,” *Appl. Therm. Eng.*, vol. 75, pp. 103–114, 2015.

[22] L. Gradisher, B. Dutcher, and M. Fan, “Catalytic hydrogen production from fossil fuels via the water gas shift reaction,” *Appl. Energy*, vol. 139, pp. 335–349, 2015.

[23] J. N. Armor, “The multiple roles for catalysis in the production of H2,” *Appl. Catal. A Gen.*, vol. 176, no. 2, pp. 159–176, 1999.

[24] M. A. Peña, J. P. Gómez, and J. L. G. Fierro, “New catalytic routes for syngas and hydrogen

production," *Appl. Catal. A Gen.*, vol. 144, no. 1–2, pp. 7–57, 1996.

[25] S. Arora and R. Prasad, "An overview on dry reforming of methane: Strategies to reduce carbonaceous deactivation of catalysts," *RSC Adv.*, vol. 6, no. 110, pp. 108668–108688, 2016.

[26] T. Zhang and M. D. Amiridis, "Hydrogen production via the direct cracking of methane over silica-supported nickel catalysts," *Appl. Catal. A Gen.*, vol. 167, no. 2, pp. 161–172, 1998.

[27] J. I. Villacampa, C. Royo, E. Romeo, J. A. Montoya, P. Del Angel, and A. Monzón, "Catalytic decomposition of methane over Ni-Al2O3 coprecipitated catalysts Reaction and regeneration studies," *Appl. Catal. A Gen.*, vol. 252, no. 2, pp. 363–383, 2003.

[28] M. S. Rahman, E. Croiset, and R. R. Hudgins, "Catalytic decomposition of methane for hydrogen production," *Top. Catal.*, vol. 37, no. 2–4, pp. 137–145, 2006.

[29] K. Otsuka, S. Takenaka, and H. Ohtsuki, "Production of pure hydrogen by cyclic decomposition of methane and oxidative elimination of carbon nanofibers on supported-Ni-based catalysts," *Appl. Catal. A Gen.*, vol. 273, no. 1–2, pp. 113–124, 2004.

[30] R. Koç, E. Alper, E. Croiset, and A. Elkamel, "Partial regeneration of Ni-based catalysts for hydrogen production via methane cracking part II: Modeling and optimization," *Turkish J. Chem.*, vol. 33, no. 6, pp. 825–841, 2009.

[31] I. Suelves, M. J. Lázaro, R. Moliner, B. M. Corbella, and J. M. Palacios, "Hydrogen production by thermo catalytic decomposition of methane on Ni-based catalysts: Influence of operating conditions on catalyst deactivation and carbon characteristics," *Int. J. Hydrogen Energy*, vol. 30, no. 15, pp. 1555–1567, 2005.

[32] T. P. Beebe, D. W. Goodman, B. D. Kay, and J. T. Yates, "Kinetics of the activated dissociative adsorption of methane on the low index planes of nickel single crystal surfaces," *J. Chem. Phys.*, vol. 87, no. 4, pp. 2305–2315, 1987.

[33] R. Aiello, J. E. Fiscus, H. C. Zur Loye, and M. D. Amiridis, "Hydrogen production via the direct cracking of methane over Ni/SiO2: Catalyst deactivation and regeneration," *Appl. Catal. A Gen.*, vol. 192, no. 2, pp. 227–234, 2000.

[34] V. R. Choudhary, S. Banerjee, and A. M. Rajput, “Continuous Production of H2 at Low Temperature from Methane Decomposition over Ni-Containing Catalyst Followed by Gasification by Steam of the Carbon on the Catalyst in Two Parallel Reactors Operated in Cyclic Manner,” *J. Catal.*, vol. 198, no. 1, pp. 136–141, 2001.

[35] N. MURADOV, Z. CHEN, and F. SMITH, “Fossil hydrogen with reduced emission: Modeling thermocatalytic decomposition of methane in a fluidized bed of carbon particles,” *Int. J. Hydrogen Energy*, vol. 30, no. 10, pp. 1149–1158, Aug. 2005.

[36] J. L. Pinilla, I. Suelves, R. Utrilla, M. E. Gálvez, M. J. Lázaro, and R. Moliner, “Hydrogen production by thermo-catalytic decomposition of methane: Regeneration of active carbons using CO2,” *J. Power Sources*, vol. 169, no. 1, pp. 103–109, 2007.

[37] S. Takenaka, Y. Tomikubo, E. Kato, and K. Otsuka, “Sequential production of H2 and CO over supported Ni catalysts,” *Fuel*, vol. 83, no. 1, pp. 47–57, 2004.

[38] H. F. Abbas and W. M. A. W. Daud, “Thermocatalytic decomposition of methane for hydrogen production using activated carbon catalyst: Regeneration and characterization studies,” *Int. J. Hydrogen Energy*, vol. 34, no. 19, pp. 8034–8045, 2009.

[39] R. T. K. Baker, M. A. Barber, P. S. Harris, F. S. Feates, and R. J. Waite, “Nucleation and growth of carbon deposits from the nickel catalyzed decomposition of acetylene,” *J. Catal.*, vol. 26, no. 1, pp. 51–62, 1972.

[40] R. T. K. Baker, “Catalytic growth of carbon filaments,” *Carbon N. Y.*, vol. 27, no. 3, pp. 315–323, 1989.

[41] Y. Yan *et al.*, “Carbon nanotube catalysts: recent advances in synthesis, characterization and applications,” *Chem. Soc. Rev.*, vol. 44, no. 10, pp. 3295–3346, 2015.

[42] S. Helveg *et al.*, “Atomic-scale imaging of carbon nanofibre growth,” *Nature*, vol. 427, no. 6973, pp. 426–429, Jan. 2004.

[43] R. T. K. Baker, “In Situ Electron Microscopy Studies of Catalyst Particle Behavior,” *Catal. Rev.*, vol. 19, no. 2, pp. 161–209, 1979.

[44] Y. Li, D. Li, and G. Wang, “Methane decomposition to COx-free hydrogen and nano-carbon

material on group 8-10 base metal catalysts: A review," *Catal. Today*, vol. 162, no. 1, pp. 1–48, 2011.

[45] K. Roebuck and A. Y. Tremblay, "The self-assembly of twinned boehmite nanosheets into porous 3D structures in ethanol-water mixtures," *Colloids Surfaces A Physicochem. Eng. Asp.*, vol. 495, pp. 238–247, 2016.

[46] K. Roebuck and A. Y. Tremblay, "Highly permeable twinned alumina nanoparticles for the precoat filtration of fine colloids," *Sep. Purif. Technol.*, vol. 182, pp. 197–206, 2017.

[47] A. Abánades, C. Rubbia, and D. Salmieri, "Thermal cracking of methane into Hydrogen for a CO2-free utilization of natural gas," *Int. J. Hydrogen Energy*, vol. 38, no. 20, pp. 8491–8496, 2013.

[48] E. Miller, "Hydrogen Supply / Demand IEA North American Roadmap Workshop," 2014. [Online]. Available: http://www.iea.org/media/workshops/2014/hydrogenroadmap/7doeericmiller.pdf.

[49] C. M. Kalamaras and A. M. Efstathiou, "Hydrogen Production Technologies: Current State and Future Developments," *Conf. Pap. Energy*, vol. 2013, pp. 1–9, 2013.

[50] J. D. Holladay, J. Hu, D. L. King, and Y. Wang, "An overview of hydrogen production technologies," *Catal. Today*, vol. 139, no. 4, pp. 244–260, 2009.

[51] F. Mueller-Langer, E. Tzimas, M. Kaltschmitt, and S. Peteves, "Techno-economic assessment of hydrogen production processes for the hydrogen economy for the short and medium term," *Int. J. Hydrogen Energy*, vol. 32, no. 16, pp. 3797–3810, 2007.

[52] K. Hassmann and H. M. Kühne, "Primary energy sources for hydrogen production," *Int. J. Hydrogen Energy*, vol. 18, no. 8, pp. 635–640, 1993.

[53] R. Kothari, D. Buddhi, and R. L. Sawhney, "Comparison of environmental and economic aspects of various hydrogen production methods," *Renew. Sustain. Energy Rev.*, vol. 12, no. 2, pp. 553–563, 2008.

[54] M. Balat, "Possible methods for hydrogen production," *Energy Sources, Part A Recover. Util. Environ. Eff.*, vol. 31, no. 1, pp. 39–50, 2009.

[55] M.-R. de Valladares, “Global Trends and Outlook for Hydrogen,” *IEA Hydrog.*, no. December, p. 20, 2017.

[56] “What is CCS?,” *Carbon Capture & Storage Association*, 2018. [Online]. Available: http://www.ccsassociation.org/what-is-ccs/. [Accessed: 22-Aug-2018].

[57] K. Goto, S. Kazama, A. Furukawa, M. Serizawa, S. Aramaki, and K. Shoji, “Effect of CO2 purity on energy requirement of CO2 capture processes,” *Energy Procedia*, vol. 37, pp. 806–812, 2013.

[58] A. Vinca, J. Emmerling, and M. Tavoni, “Bearing the cost of stored carbon leakage,” *Front. Energy Res.*, vol. 6, no. JUN, pp. 1–11, 2018.

[59] L. Weger, A. Abánades, and T. Butler, “Methane cracking as a bridge technology to the hydrogen economy,” *Int. J. Hydrogen Energy*, vol. 42, no. 1, pp. 720–731, 2017.

[60] T. Ishihara, Y. Miyashita, H. Iseda, and Y. Takita, “Decomposition of Methane over Ni/SiO 2 Catalysts with Membrane Reactor for the Production of Hydrogen,” *Chem. Lett.*, vol. 24, no. 2, pp. 93–94, Feb. 1995.

[61] A. M. Dunker, S. Kumar, and P. A. Mulawa, “Production of hydrogen by thermal decomposition of methane in a fluidized-bed reactor - Effects of catalyst, temperature, and residence time,” *Int. J. Hydrogen Energy*, vol. 31, no. 4, pp. 473–484, 2006.

[62] J. Galuszka, R. N. Pandey, and S. Ahmed, “Methane conversion to syngas in a palladium membrane reactor,” *Catal. Today*, vol. 46, no. 2–3, pp. 83–89, 1998.

[63] T. Ishihara *et al.*, “CH 4 Decomposition with a Pd−Ag Hydrogen-Permeating Membrane Reactor for Hydrogen Production at Decreased Temperature,” *Ind. Eng. Chem. Res.*, vol. 41, no. 14, pp. 3365–3369, 2002.

[64] M. N. Pedernera, J. Piña, and D. O. Borio, “Kinetic evaluation of carbon formation in a membrane reactor for methane reforming,” *Chem. Eng. J.*, vol. 134, no. 1–3, pp. 138–144, 2007.

[65] E. Kikuchi, “Membrane Reactor Application to Hydrogen Production,” *Catal. Today*, vol. 56, no. 1–3, pp. 97–101, 2000.

[66] S. Takenaka, M. Serizawa, and K. Otsuka, “Formation of filamentous carbons over supported Fe catalysts through methane decomposition,” *J. Catal.*, vol. 222, no. 2, pp. 520–531, 2004.

[67] M. A. Ermakova, D. Y. Ermakov, A. L. Chuvilin, and G. G. Kuvshinov, “Decomposition of methane over iron catalysts at the range of moderate temperatures: The influence of structure of the catalytic systems and the reaction conditions on the yield of carbon and morphology of carbon filaments,” *J. Catal.*, vol. 201, no. 2, pp. 183–197, 2001.

[68] T. Ishihara *et al.*, “CH4 decomposition with a Pd-Ag hydrogen-permeating membrane reactor for hydrogen production at decreased temperature,” *Ind. Eng. Chem. Res.*, vol. 41, no. 14, pp. 3365–3369, 2002.

[69] A. A. Plazaola, D. A. P. Tanaka, M. V. S. Annaland, and F. Gallucci, “Recent advances in pd-based membranes for membrane reactors,” *Molecules*, vol. 22, no. 1, pp. 1–53, 2017.

[70] A. Iulianelli *et al.*, “H2 production by low pressure methane steam reforming in a Pd-Ag membrane reactor over a Ni-based catalyst: Experimental and modeling,” *Int. J. Hydrogen Energy*, vol. 35, no. 20, pp. 11514–11524, 2010.

[71] K. S. Han, J. H. Kim, H. K. Kim, and K. T. Hwang, “Direct methane cracking using a mixed conducting ceramic membrane for production of hydrogen and carbon,” *Int. J. Hydrogen Energy*, vol. 38, no. 36, pp. 16133–16139, 2013.

[72] S. N. Paglieri, J. R. Wermer, R. E. Buxbaum, M. V. Ciocco, B. H. Howard, and B. D. Morreale, “Development of membranes for hydrogen separation: Pd coated V–10Pd,” *Energy Mater.*, vol. 3, no. 3, pp. 169–176, 2008.

[73] M. H. Kim *et al.*, “Hydrogen production by catalytic decomposition of methane over activated carbons: Kinetic study,” *Int. J. Hydrogen Energy*, vol. 29, no. 2, pp. 187–193, 2004.

[74] M. H. Kim *et al.*, “Hydrogen production by catalytic decomposition of methane over activated carbons: Deactivation study,” *Korean J. Chem. Eng.*, vol. 20, no. 5, pp. 835–839, 2003.

[75] K. K. Lee, G. Y. Han, K. J. Yoon, and B. K. Lee, “Thermocatalytic hydrogen production

from the methane in a fluidized bed with activated carbon catalyst," *Catal. Today*, vol. 93–95, pp. 81–86, 2004.

[76] Z. Wang, X. M. Cao, J. Zhu, and P. Hu, "Activity and coke formation of nickel and nickel carbide in dry reforming: A deactivation scheme from density functional theory," *J. Catal.*, vol. 311, pp. 469–480, 2014.

[77] M. J. Hosseini *et al.*, "New mechanistic approach of inorganic palladium toxicity: Impairment in mitochondrial electron transfer," *Metallomics*, vol. 8, no. 2, pp. 252–259, 2016.

[78] T. K. Grimsrud, S. R. Berge, F. Resmann, T. Norseth, and A. Andersen, "Assessment of historical exposures in a nickel refinery in Norway," *Scand. J. Work. Environ. Heal.*, vol. 26, no. 4, pp. 338–345, 2000.

[79] T. K. Grimsrud and A. Andersen, "Unrecognized risks of nickel-related respiratory cancer among Canadian electrolysis workers," *Scand. J. Work. Environ. Heal.*, vol. 38, no. 6, pp. 503–515, 2012.

[80] H. W. Abu El Hawa, S. N. Paglieri, C. C. Morris, A. Harale, and J. Douglas Way, "Application of a Pd-Ru composite membrane to hydrogen production in a high temperature membrane reactor," *Sep. Purif. Technol.*, vol. 147, pp. 388–397, 2015.

[81] J. S. H. Q. Perera, J. W. Couves, G. Sankar, and J. M. Thomas, "The catalytic activity of Ru and Ir supported on Eu2O3 for the reaction, CO2 + CH4 ⇄ 2 H2 + 2 CO: a viable solar-thermal energy system," *Catal. Letters*, vol. 11, no. 2, pp. 219–225, 1991.

[82] M. a. Ermakova and D. Y. Ermakov, "Ni/SiO2 and Fe/SiO2 catalysts for production of hydrogen and filamentous carbon via methane decomposition," *Catal. Today*, vol. 77, no. 3, pp. 225–235, 2002.

[83] S. Ahmed, A. Aitani, F. Rahman, A. Al-Dawood, and F. Al-Muhaish, "Decomposition of hydrocarbons to hydrogen and carbon," *Appl. Catal. A Gen.*, vol. 359, no. 1–2, pp. 1–24, 2009.

[84] N. Shah, D. Panjala, and G. P. Huffman, "Hydrogen production by catalytic decomposition of methane," *Energy and Fuels*, vol. 15, no. 6, pp. 1528–1534, 2001.

[85] A. Konieczny, K. Mondal, T. Wiltowski, and P. Dydo, “Catalyst development for thermocatalytic decomposition of methane to hydrogen,” *Int. J. Hydrogen Energy*, vol. 33, no. 1, pp. 264–272, 2008.

[86] A. A. Ibrahim, A. H. Fakeeha, A. S. Al-Fatesh, A. E. Abasaeed, and W. U. Khan, “Methane decomposition over iron catalyst for hydrogen production,” *Int. J. Hydrogen Energy*, vol. 40, no. 24, pp. 7593–7600, 2015.

[87] A. H. Fakeeha, A. A. Ibrahim, W. U. Khan, K. Seshan, R. L. Al Otaibi, and A. S. Al-Fatesh, “Hydrogen production via catalytic methane decomposition over alumina supported iron catalyst,” *Arab. J. Chem.*, vol. 11, no. 3, pp. 405–414, 2018.

[88] C. Drive, *Nanomaterials, Nanotechnologies and Design*, vol. 47, no. 04. Elsevier, 2009.

[89] T. V. Reshetenko *et al.*, “Catalytic filamentous carbon: Structural and textural properties,” *Carbon N. Y.*, vol. 41, no. 8, pp. 1605–1615, 2003.

[90] A. P. Simpson and A. E. Lutz, “Exergy analysis of hydrogen production via steam methane reforming,” *Int. J. Hydrogen Energy*, vol. 32, no. 18, pp. 4811–4820, 2007.

[91] B. Dawoud, E. Amer, and D. Gross, “Thermodynamic analysis of H2 production from CaO sorption-enhanced methane steam reforming thermally coupled with chemical looping combustion as a novel technology,” *Int. J. energy Res.*, vol. 31, no. August 2007, pp. 135–147, 2007.

[92] C. Song, Q. Liu, N. Ji, Y. Kansha, and A. Tsutsumi, “Optimization of steam methane reforming coupled with pressure swing adsorption hydrogen production process by heat integration,” *Appl. Energy*, vol. 154, pp. 392–401, 2015.

[93] N. W. Ockwig and T. M. Nenoff, “Membranes for hydrogen separation,” *Chem. Rev.*, vol. 107, no. 10, pp. 4078–4110, 2007.

[94] K. F. Tzanetis, C. S. Martavaltzi, and A. A. Lemonidou, “Comparative exergy analysis of sorption enhanced and conventional methane steam reforming,” *Int. J. Hydrogen Energy*, vol. 37, no. 21, pp. 16308–16320, 2012.

[95] M. G. Poirier and C. Sapundzhiev, “Catalytic decomposition of natural gas to hydrogen for

fuel cell applications," *Int. J. Hydrogen Energy*, vol. 22, no. 4, pp. 429–433, 1997.

[96] A. Luengnaruemitchai, S. Osuwan, and E. Gulari, "Comparative studies of low-temperature water-gas shift reaction over Pt/CeO2, Au/CeO2, and Au/Fe2O3 catalysts," *Catal. Commun.*, vol. 4, no. 5, pp. 215–221, 2003.

[97] S. T. Oyama, P. Hacarlioglu, Y. Gu, and D. Lee, "Dry reforming of methane has no future for hydrogen production: Comparison with steam reforming at high pressure in standard and membrane reactors," *Int. J. Hydrogen Energy*, vol. 37, no. 13, pp. 10444–10450, 2012.

[98] J. K. Dahl, J. Tamburini, A. W. Weimer, A. Lewandowski, R. Pitts, and C. Bingham, "Solar-thermal processing of methane to produce hydrogen and syngas," *Energy and Fuels*, vol. 15, no. 5, pp. 1227–1232, 2001.

[99] S. Rodat, S. Abanades, J. L. Sans, and G. Flamant, "A pilot-scale solar reactor for the production of hydrogen and carbon black from methane splitting," *Int. J. Hydrogen Energy*, vol. 35, no. 15, pp. 7748–7758, 2010.

[100] M. STEINBERG, "Production of hydrogen and methanol from natural gas with reduced CO2 emission," *Int. J. Hydrogen Energy*, vol. 23, no. 6, pp. 419–425, 1998.

[101] X. Li, G. Zhu, S. Qi, J. Huang, and B. Yang, "Simultaneous production of hythane and carbon nanotubes via catalytic decomposition of methane with catalysts dispersed on porous supports," *Appl. Energy*, vol. 130, pp. 846–852, 2014.

[102] N. Muradov, "Catalysis of methane decomposition over elemental carbon," *Catal. Commun.*, vol. 2, no. 3–4, pp. 89–94, 2001.

[103] M. Bajus and M. H. Back, "The use of carbon catalysts and of nitrous oxide in promoting the conversion of methane," *Appl. Catal. A, Gen.*, vol. 128, no. 1, pp. 61–77, 1995.

[104] W. Wu, Q. He, and C. Jiang, "Magnetic iron oxide nanoparticles: Synthesis and surface functionalization strategies," *Nanoscale Res. Lett.*, vol. 3, no. 11, pp. 397–415, 2008.

[105] A. H. Lu, E. L. Salabas, and F. Schüth, "Magnetic nanoparticles: Synthesis, protection, functionalization, and application," *Angew. Chemie - Int. Ed.*, vol. 46, no. 8, pp. 1222–1244, 2007.

[106] L. L. Vatta, R. D. Sanderson, and K. R. Koch, "Magnetic nanoparticles: Properties and potential applications," *Pure Appl. Chem.*, vol. 78, no. 9, pp. 1793–1801, Jan. 2006.

[107] E. Roduner, "Size matters: Why nanomaterials are different," *Chem. Soc. Rev.*, vol. 35, no. 7, pp. 583–592, 2006.

[108] K. J. Klabunde, *Free Atoms, Clusters, and Nanoscale Particles*. 2012.

[109] A. Khaleel, W. Li, and K. J. Klabunde, "Nanocrystals as stoichiometric reagents with unique surface chemistry. New adsorbents for air purification," *Nanostructured Mater.*, vol. 12, no. 1, pp. 463–466, 1999.

[110] K. Nishimura, N. Okazaki, L. Pan, and Y. Nakayama, "In situ study of iron catalysts for carbon nanotube growth using X-ray diffraction analysis," *Japanese J. Appl. Physics, Part 2 Lett.*, vol. 43, no. 4 A, pp. 8–12, 2004.

[111] D. W. Jung *et al.*, "Optimizing control of Fe catalysts for carbon nanotube growth," *J. Nanosci. Nanotechnol.*, vol. 12, no. 7, pp. 5663–5668, 2012.

[112] I. T. Kim, G. A. Nunnery, K. Jacob, J. Schwartz, X. Liu, and R. Tannenbaum, "Synthesis, characterization, and alignment of magnetic carbon nanotubes tethered with maghemite nanoparticles," *J. Phys. Chem. C*, vol. 114, no. 15, pp. 6944–6951, 2010.

[113] H. Kataura *et al.*, "Diameter control of single-walled carbon nanotubes," *Carbon N. Y.*, vol. 38, no. 11, pp. 1691–1697, 2000.

[114] V. Jourdain and C. Bichara, "Current understanding of the growth of carbon nanotubes in catalytic chemical vapour deposition," *Carbon N. Y.*, vol. 58, pp. 2–39, 2013.

[115] S. Rajput, C. U. Pittman, and D. Mohan, "Magnetic magnetite (Fe3O4) nanoparticle synthesis and applications for lead (Pb2+) and chromium (Cr6+) removal from water," *J. Colloid Interface Sci.*, vol. 468, pp. 334–346, 2016.

[116] H. C. Roth, S. P. Schwaminger, M. Schindler, F. E. Wagner, and S. Berensmeier, "Influencing factors in the CO-precipitation process of superparamagnetic iron oxide nano particles: A model based study," *J. Magn. Magn. Mater.*, vol. 377, pp. 81–89, 2015.

[117] D. D. Suppiah and S. B. Abd Hamid, "One step facile synthesis of ferromagnetic magnetite

nanoparticles," *J. Magn. Magn. Mater.*, vol. 414, pp. 204–208, 2016.

[118] B. M. Kumfer, K. Shinoda, B. Jeyadevan, and I. M. Kennedy, "Gas-phase flame synthesis and properties of magnetic iron oxide nanoparticles with reduced oxidation state," *J. Aerosol Sci.*, vol. 41, no. 3, pp. 257–265, 2010.

[119] F. Fajaroh, H. Setyawan, W. Widiyastuti, and S. Winardi, "Synthesis of magnetite nanoparticles by surfactant-free electrochemical method in an aqueous system," *Adv. Powder Technol.*, vol. 23, no. 3, pp. 328–333, 2012.

[120] W. S. Peternele *et al.*, "Experimental investigation of the coprecipitation method: An approach to obtain magnetite and maghemite nanoparticles with improved properties," *J. Nanomater.*, vol. 2014, no. 1, pp. 1–11, 2014.

[121] H. Cui, Y. Feng, W. Ren, T. Zeng, H. Lv, and Y. Pan, "Strategies of Large Scale Synthesis of Monodisperse Nanoparticles," *Recent Pat. Nanotechnol.*, vol. 3, no. 1, pp. 32–41, 2008.

[122] Y. Tian *et al.*, "Fast coalescence of metallic glass nanoparticles," *Nat. Commun.*, vol. 10, no. 1, pp. 1–8, 2019.

[123] F. Behafarid and B. Roldan Cuenya, "Coarsening phenomena of metal nanoparticles and the influence of the support pre-treatment: Pt/TiO 2(110)," *Surf. Sci.*, vol. 606, no. 11–12, pp. 908–918, 2012.

[124] J. Park *et al.*, "One-nanometer-scale size-controlled synthesis of monodisperse magnetic iron oxide nanoparticles," *Angew. Chemie - Int. Ed.*, vol. 44, no. 19, pp. 2872–2877, 2005.

[125] F. Yazdani and M. Seddigh, "Magnetite nanoparticles synthesized by co-precipitation method: The effects of various iron anions on specifications," *Mater. Chem. Phys.*, vol. 184, pp. 318–323, 2016.

[126] T. Ishikawa, S. Kataoka, and K. Kandori, "The influence of carboxylate ions on the growth of β-FeOOH particles," *J. Mater. Sci.*, vol. 28, no. 10, pp. 2693–2698, May 1993.

[127] H. Kodama and M. Schnitzer, "Effect of fulvic acid on the crystallization of Fe(III) oxides," *Geoderma*, vol. 19, no. 4, pp. 279–291, 1977.

[128] T. Ishikawa, T. Takeda, and K. Kandori, "Effects of amines on the formation of β-ferric

oxide hydroxide," *J. Mater. Sci.*, vol. 27, no. 16, pp. 4531–4535, 1992.

[129] K. Kandori, Y. Kawashima, and T. Ishikawa, "Effects of citrate ions on the formation of monodispersed cubic hematite particles," *J. Colloid Interface Sci.*, vol. 152, no. 1, pp. 284–288, 1992.

[130] P. S. Sidhu, R. J. Gilkes, and A. M. Posner, "The synthesis and some properties of Co, Ni, Zn, Cu, Mn and Cd substituted magnetites," *J. Inorg. Nucl. Chem.*, vol. 40, no. 3, pp. 429–435, 1978.

[131] A. Bee, R. Massart, and S. Neveu, "Synthesis of very fine maghemite particles," *J. Magn. Magn. Mater.*, vol. 149, no. 1–2, pp. 6–9, 1995.

[132] M. Simmons, C. Wiles, V. Rocher, M. G. Francesconi, and P. Watts, "The Preparation of Magnetic Iron Oxide Nanoparticles in Microreactors," *J. Flow Chem.*, vol. 3, no. 1, pp. 7–10, 2013.

[133] M. Filippousi *et al.*, "Surfactant effects on the structural and magnetic properties of iron oxide nanoparticles," *J. Phys. Chem. C*, vol. 118, no. 29, pp. 16209–16217, 2014.

[134] J. Wan, G. Tang, and Y. Qian, "Room temperature synthesis of single-crystal Fe3O4 nanoparticles with superparamagnetic property," *Appl. Phys. A Mater. Sci. Process.*, vol. 86, no. 2, pp. 261–264, 2007.

[135] A. Gohier, C. P. Ewels, T. M. Minea, and M. A. Djouadi, "Carbon nanotube growth mechanism switches from tip- to base-growth with decreasing catalyst particle size," *Carbon N. Y.*, vol. 46, no. 10, pp. 1331–1338, 2008.

[136] P. Moodley, J. Loos, J. W. Niemantsverdriet, and P. C. Thüne, "Is there a correlation between catalyst particle size and CNT diameter?," *Carbon N. Y.*, vol. 47, no. 8, pp. 2002–2013, 2009.

[137] J. Dijon *et al.*, "How to switch from a tip to base growth mechanism in carbon nanotube growth by catalytic chemical vapour deposition," *Carbon N. Y.*, vol. 48, no. 13, pp. 3953–3963, 2010.

[138] Z. Pi, Z. Liu, C. Yang, X. Tian, J. Fei, and J. Zheng, "Exfoliation of kaolinite by urea-

intercalation precursor and microwave irradiation assistance process," *Front. Earth Sci. China*, vol. 1, no. 1, pp. 26–29, 2007.

[139] W. A. Deer, R. A. Howie, and J. Zussman, *An Introduction to the Rock-Forming Minerals*. 2013.

[140] X. Zuo, D. Wang, S. Zhang, Q. Liu, and H. Yang, "Intercalation and Exfoliation of Kaolinite with Sodium Dodecyl Sulfate," *Minerals*, vol. 8, no. 3, p. 112, Mar. 2018.

[141] G. Suraj, C. S. P. Iyer, S. Rugmini, and M. Lalithambika, "The effect of micronization on kaolinites and their sorption behaviour," *Appl. Clay Sci.*, vol. 12, no. 1–2, pp. 111–130, 1997.

[142] P. J. Sánchez-Soto, M. Carmen Jiménez de Haro, L. A. Pérez-Maqueda, I. Varona, and J. L. Pérez-Rodríguez, "Effects of Dry Grinding on the Structural Changes of Kaolinite Powders," *J. Am. Ceram. Soc.*, vol. 83, no. 7, pp. 1649–1657, 2010.

[143] R. L. Frost, É. Makó, J. Kristóf, E. Horváth, and J. T. Kloprogge, "Mechanochemical treatment of kaolinite," *J. Colloid Interface Sci.*, vol. 239, no. 2, pp. 458–466, 2001.

[144] R. L. Frost, E. Horváth, É. Makó, and J. Kristóf, "Modification of low- and high-defect kaolinite surfaces: Implications for kaolinite mineral processing," *J. Colloid Interface Sci.*, vol. 270, no. 2, pp. 337–346, 2004.

[145] J. A. G. L. Velho and C. d. S. F. Gomes, "Characterization of Portuguese kaolins for the paper industry: beneficiation through new delamination techniques," *Appl. Clay Sci.*, vol. 6, no. 2, pp. 155–170, Sep. 1991.

[146] M. Valášková, M. Rieder, V. Matějka, P. Čapková, and A. Slíva, "Exfoliation/delamination of kaolinite by low-temperature washing of kaolinite–urea intercalates," *Appl. Clay Sci.*, vol. 35, no. 1–2, pp. 108–118, Jan. 2007.

[147] F. Franco, L. A. Pérez-Maqueda, and J. L. Pérez-Rodríguez, "The effect of ultrasound on the particle size and structural disorder of a well-ordered kaolinite," *J. Colloid Interface Sci.*, vol. 274, no. 1, pp. 107–117, 2004.

[148] A. Weiss, "Ein Geheimnis des chinesischen Porzellans," *Angew. Chemie*, vol. 75, no. 16–

17, pp. 755–762, Sep. 1963.

[149] A. Weiss, and H. Orth, “Neue Einlagerungsverbindungen von Kaolinit, Nakrit, Dickit, Halloysit und Titandisulfid mit Imidazol und Methylimidazol / New Layer Intercalation Compounds of Kaolinite, Nacrite, Dickite, Halloysite and Titandisulfide with Imidazole and Methylimidazole,” *Zeitschrift für Naturforsch. B*, vol. 28, no. 7–8, pp. 446–449, Aug. 2015.

[150] K. TSUNEMATSU, H. TATEYAMA, S. NISHIMURA, and K. JINNAI, “Delamination of Kaolinite by Intercalation of Urea,” *J. Ceram. Soc. Japan*, vol. 100, no. 1158, pp. 178–181, 1992.

[151] K. Tsunematsu and H. Tateyama, “Delamination of Urea-Kaolinite Complex by Using Intercalation Procedures,” *J. Am. Ceram. Soc.*, vol. 82, no. 6, pp. 1589–1591, 2004.

[152] G. Urretavizcaya, A. L. Cavalieri, J. M. Porto López, I. Sobrados, and J. Sanz, “Thermal Evolution of Alumina Prepared by the Sol-Gel Technique,” *J. Mater. Synth. Process.*, vol. 6, no. 1, pp. 1–7, 1998.

[153] H. Arai and M. Machida, “Thermal stabilization of catalyst supports and their application to high-temperature catalytic combustion,” *Appl. Catal. A Gen.*, vol. 138, no. 2, pp. 161–176, 1996.

[154] X. Wang, G. Lu, Y. Guo, Y. Wang, and Y. Guo, “Preparation of high thermal-stabile alumina by reverse microemulsion method,” *Mater. Chem. Phys.*, vol. 90, no. 2–3, pp. 225–229, 2005.

[155] Y. Mizushima and M. Hori, “Preparation of heat-resistant alumina aerogels,” *J. Mater. Res.*, vol. 8, no. 11, pp. 2993–2999, 1993.

[156] P. Burtin, J. P. Brunelle, M. Pijolat, and M. Soustelle, “Influence of surface area and additives on the thermal stability of transition alumina catalyst supports. I: Kinetic data,” *Appl. Catal.*, vol. 34, pp. 225–238, Jan. 1987.

[157] E. A. El-Sharkawy, S. A. El-Hakam, and S. E. Samra, “Effect of thermal treatment on the various properties of iron(III)-aluminum(III) coprecipitated hydroxide system,” *Mater. Lett.*, vol. 42, no. 5, pp. 331–338, 2000.

[158] T. Horiuchi, T. Osaki, T. Sugiyama, K. Suzuki, and T. Mori, “Maintenance of large surface area of alumina heated at elevated temperatures above 1300 °C by preparing silica-containing pseudoboehmite aerogel,” *J. Non. Cryst. Solids*, vol. 291, no. 3, pp. 187–198, 2001.

[159] J. F. Hochepied and P. Nortier, “Influence of precipitation conditions (pH and temperature) on the morphology and porosity of boehmite particles,” *Powder Technol.*, vol. 128, no. 2–3, pp. 268–275, 2002.

[160] B. Tang *et al.*, “A facile and controllable synthesis of γ-Al2O3 nanostructures without a surfactant,” *Eur. J. Inorg. Chem.*, vol. 1, no. 21, pp. 4366–4369, 2005.

[161] T. T. Song *et al.*, “The stability of aluminium oxide monolayer and its interface with two-dimensional materials,” *Sci. Rep.*, vol. 6, no. March, pp. 1–9, 2016.

[162] M. S. Prasad, K. J. Reid, and H. H. Murray, “Kaolin: processing, properties and applications,” *Appl. Clay Sci.*, vol. 6, no. 2, pp. 87–119, Sep. 1991.

[163] W. M. Bundy and J. N. Ishley, “Kaolin in paper filling and coating,” *Appl. Clay Sci.*, vol. 5, no. 5–6, pp. 397–420, 1991.

[164] J. G. Miller and T. D. Oulton, “Prototropy in kaolinite during percussive grinding,” *Clays Clay Miner.*, vol. 18, no. 6, pp. 313–323, 1970.

[165] E. F. Aglietti, J. M. Porto Lopez, and E. Pereira, “Mechanochemical effects in kaolinite grinding. I. Textural and physicochemical aspects,” *Int. J. Miner. Process.*, vol. 16, no. 1–2, pp. 125–133, 1986.

[166] A. Weiss and W. Thielepape, “Method of treating clay and clay produced thereby,” 3,309,211, 1963.

[167] C. B. Maxwell and P. B. Malla, “Kaolin Delamination Techniques and Their Effects on Morphology, Crystallinity, and Suspension Rheology,” vol. 21, pp. 291–303, 2008.

[168] J. E. Gardolinski, F. Wypych, and M. P. Cantão, “Esfoliação e hidratação da caulinita após intercalação com uréia.,” *Quim. Nova*, vol. 24, no. 6, pp. 761–767, 2001.

[169] C. T. Johnston, J. E. Kogel, D. L. Bish, T. Kogure, and H. H. Murray, “Low-temperature

FTIR study of kaolin-group minerals," *Clays Clay Miner.*, vol. 56, no. 4, pp. 470–485, 2008.

[170] R. F. Giese, "Kaolin group minerals," in *Sedimentology*, Dordrecht: Springer Netherlands, pp. 651–655.

[171] F. M. Lee and L. E. Lahti, "Solubility of Urea in Water-Alcohol Mixtures," *J. Chem. Eng. Data*, vol. 17, no. 3, pp. 304–306, 1972.

[172] L. A. Pinck and M. A. Kelly, "The Solubility of Urea in Water," *J. Am. Chem. Soc.*, vol. 47, no. 8, pp. 2170–2172, 1925.

[173] R. S. Shelton *et al.*, "Quaternary Ammonium Salts as Germicides. I. Non-acylated Quaternary Ammonium Salts Derived from Aliphatic Amines," *J. Am. Chem. Soc.*, vol. 68, no. 5, pp. 753–755, 1946.

[174] Ashland, "Commercial Types of PVP polymers," Essen, 2013.

[175] Y. Moroi, M. Kitagawa, and H. Itoh, "Aqueous solubility and acidity constants of cholic, deoxycholic, chenodeoxycholic, and ursodeoxycholic acids.," *J. Lipid Res.*, vol. 33, no. 1, pp. 49–53, 1992.

[176] E. Balan, G. Calas, and D. L. Bish, "Kaolin-group minerals: From hydrogen-bonded layers to environmental recorders," *Elements*, vol. 10, no. 3, pp. 183–188, 2014.

[177] M. H. Eley, P. C. Burns, C. C. Kannapell, and P. S. Campbell, "Cetyltrimethylammonium bromide polyacrylamide gel electrophoresis: Estimation of protein subunit molecular weights using cationic detergents," *Anal. Biochem.*, vol. 92, no. 2, pp. 411–419, 1979.

[178] S. H. Hansen, P. Helboe, M. Thomsen, and U. Lund, "High-performance liquid chromatography on dynamically modified silica : II. Modification of various silica packings with cetyltrimethylammonium bromide," *J. Chromatogr. A*, vol. 210, no. 3, pp. 453–460, Jun. 1981.

[179] M. G. Murray and W. F. Thompson, "Rapid isolation of high molecular weight plant DNA," *Nucleic Acids Res.*, vol. 8, no. 19, pp. 4321–4326, 1980.

[180] E. J. White, M. Venter, N. F. Hiten, and J. T. Burger, "Modified cetyltrimethylammonium bromide method improves robustness and versatility: The benchmark for plant RNA

extraction," *Biotechnol. J.*, vol. 3, no. 11, pp. 1424–1428, 2008.

[181] H. Sugioka, K. Matsuoka, and Y. Moroi, "Temperature effect on formation of sodium cholate micelles," *J. Colloid Interface Sci.*, vol. 259, no. 1, pp. 156–162, 2003.

[182] M. M. Miller, G. A. Prinz, S. F. Cheng, and S. Bounnak, "Detection of a micron-sized magnetic sphere using a ring-shaped anisotropic magnetoresistance-based sensor: A model for a magnetoresistance-based biosensor," *Appl. Phys. Lett.*, vol. 81, no. 12, pp. 2211–2213, 2002.

[183] F. Yazdani, B. Fattahi, and N. Azizi, "Synthesis of functionalized magnetite nanoparticles to use as liver targeting MRI contrast agent," *J. Magn. Magn. Mater.*, vol. 406, pp. 207–211, 2016.

[184] S. Sun and H. Zeng, "Size-controlled synthesis of magnetite nanoparticles," *J. Am. Chem. Soc.*, vol. 124, no. 28, pp. 8204–8205, 2002.

[185] L. Cabrera, S. Gutierrez, N. Menendez, M. P. Morales, and P. Herrasti, "Magnetite nanoparticles: Electrochemical synthesis and characterization," *Electrochim. Acta*, vol. 53, no. 8, pp. 3436–3441, 2008.

[186] G. A. Bukhtiyarova, M. A. Shuvaeva, O. A. Bayukov, S. S. Yakushkin, and O. N. Martyanov, "Facile synthesis of nanosized ε-Fe2O3 particles on the silica support," *J. Nanoparticle Res.*, vol. 13, no. 10, pp. 5527–5534, 2011.

[187] F. H. Chen, L. M. Zhang, Q. T. Chen, Y. Zhang, and Z. J. Zhang, "Synthesis of a novel magnetic drug delivery system composed of doxorubicin-conjugated Fe3O4 nanoparticle cores and a PEG-functionalized porous silica shell," *Chem. Commun.*, vol. 46, no. 45, pp. 8633–8635, 2010.

[188] H. Karami, "Heavy metal removal from water by magnetite nanorods," *Chem. Eng. J.*, vol. 219, pp. 209–216, 2013.

[189] A. R. Mahdavian and M. A. S. Mirrahimi, "Efficient separation of heavy metal cations by anchoring polyacrylic acid on superparamagnetic magnetite nanoparticles through surface modification," *Chem. Eng. J.*, vol. 159, no. 1–3, pp. 264–271, 2010.

[190] E. Lamouroux, P. Serp, and P. Kalck, "Catalytic routes towards single wall carbon nanotubes," *Catal. Rev. - Sci. Eng.*, vol. 49, no. 3, pp. 341–405, 2007.

[191] M. Pudukudy and Z. Yaakob, "Methane decomposition over Ni, Co and Fe based monometallic catalysts supported on sol gel derived SiO2 microflakes," *Chem. Eng. J.*, vol. 262, pp. 1009–1021, 2015.

[192] M. Pudukudy, Z. Yaakob, and Z. S. Akmal, "Direct decomposition of methane over SBA-15 supported Ni, Co and Fe based bimetallic catalysts," *Appl. Surf. Sci.*, vol. 330, pp. 418–430, 2015.

[193] L. Jin *et al.*, "Preparation of activated carbon supported Fe-Al2O3 catalyst and its application for hydrogen production by catalytic methane decomposition," *Int. J. Hydrogen Energy*, vol. 38, no. 25, pp. 10373–10380, 2013.

[194] D. Torres, S. De Llobet, J. L. Pinilla, M. J. Lázaro, I. Suelves, and R. Moliner, "Hydrogen production by catalytic decomposition of methane using a Fe-based catalyst in a fluidized bed reactor," *J. Nat. Gas Chem.*, vol. 21, no. 4, pp. 367–373, 2012.

[195] H. F. Abbas and W. M. A. W. Daud, "Deactivation of palm shell-based activated carbon catalyst used for hydrogen production by thermocatalytic decomposition of methane," *Int. J. Hydrogen Energy*, vol. 34, no. 15, pp. 6231–6241, 2009.

[196] H. F. Abbas and W. M. A. Wan Daud, "Hydrogen production by methane decomposition: A review," *Int. J. Hydrogen Energy*, vol. 35, no. 3, pp. 1160–1190, 2010.

[197] X. Guo *et al.*, "Direct, nonoxidative conversion of methane to ethylene, aromatics, and hydrogen," *Science (80-.).*, vol. 344, no. 6184, pp. 616–619, 2014.

[198] V. L. Kuznetsov, A. N. Usoltseva, A. L. Chuvilin, E. D. Obraztsova, and J. M. Bonard, "Thermodynamic analysis of nucleation of carbon deposits on metal particles and its implications for the growth of carbon nanotubes," *Phys. Rev. B - Condens. Matter Mater. Phys.*, vol. 64, no. 23, pp. 2354011–2354017, 2001.

[199] W. Xiao *et al.*, "Microwave-assisted synthesis of magnetite nanoparticles for MR blood pool contrast agents," *J. Magn. Magn. Mater.*, vol. 324, no. 4, pp. 488–494, 2012.

[200] T. M. Freire *et al.*, "Fast ultrasound assisted synthesis of chitosan-based magnetite nanocomposites as a modified electrode sensor," *Carbohydr. Polym.*, vol. 151, pp. 760–769, 2016.

[201] O. A. Attallah, E. Girgis, and M. M. S. A. Abdel-Mottaleb, "Tailored super magnetic nanoparticles synthesized via template free hydrothermal technique," *J. Magn. Magn. Mater.*, vol. 397, pp. 164–175, 2016.

[202] P. Azcona, R. Zysler, and V. Lassalle, "Simple and novel strategies to achieve shape and size control of magnetite nanoparticles intended for biomedical applications," *Colloids Surfaces A Physicochem. Eng. Asp.*, vol. 504, pp. 320–330, 2016.

[203] W. Glasgow *et al.*, "Continuous synthesis of iron oxide (Fe3O4) nanoparticles via thermal decomposition," *Particuology*, vol. 26, pp. 47–53, 2016.

[204] K. J. Rockne, "Kinetic hindrance of Fe(II) oxidation at alkaline pH and in the presence of nitrate and oxygen in a facultative wastewater stabilization pond," *J. Environ. Sci. Heal. - Part A Toxic/Hazardous Subst. Environ. Eng.*, vol. 42, no. 3, pp. 265–275, 2007.

[205] T. H. Christensen, P. L. Bjerg, S. A. Banwart, R. Jakobsen, G. Heron, and H. J. Albrechtsen, "Characterization of redox conditions in groundwater contaminant plumes," *J. Contam. Hydrol.*, vol. 45, no. 3–4, pp. 165–241, 2000.

[206] J. P. Jolivet *et al.*, "Size tailoring of oxide nanoparticles by precipitation in aqueous medium. A semi-quantitative modelling," *J. Mater. Chem.*, vol. 14, no. 21, pp. 3281–3288, 2004.

[207] S. P. Schwaminger, D. Bauer, P. Fraga-García, F. E. Wagner, and S. Berensmeier, "Oxidation of magnetite nanoparticles: impact on surface and crystal properties," *CrystEngComm*, vol. 19, no. 2, pp. 246–255, 2017.

[208] Y. Xia, X. Jiao, Y. Liu, D. Chen, L. Zhang, and Z. Qin, "Study of the formation mechanism of boehmite with different morphology upon surface hydroxyls and adsorption of chloride ions," *J. Phys. Chem. C*, vol. 117, no. 29, pp. 15279–15286, 2013.

[209] N. Kumar, C. Zhao, A. Klaassen, D. Van den Ende, F. Mugele, and I. Siretanu, "Characterization of the surface charge distribution on kaolinite particles using high resolution atomic force microscopy," *Geochim. Cosmochim. Acta*, vol. 175, pp. 100–112,

2016.

[210] L. D. Marks and L. Peng, “Nanoparticle shape, thermodynamics and kinetics,” *J. Phys. Condens. Matter*, vol. 28, no. 5, p. 53001, 2016.

[211] S. M. Yusuf *et al.*, “Experimental study of the structural and magnetic properties of γ- Fe2 O3 nanoparticles,” *Phys. Rev. B - Condens. Matter Mater. Phys.*, vol. 74, no. 22, pp. 1–11, 2006.

[212] M. Chirita, M. L. Kiss, A. Ieta, A. Ercuta, and I. Grozescu, “Synthesis of micrometric single crystalline magnetite with superparamagnetic properties for biomedical applications,” *Tech. Proc. 2013 NSTI Nanotechnol. Conf. Expo, NSTI-Nanotech 2013*, vol. 1, pp. 378–381, 2013.

[213] K. Kolo, K. Konhauser, W. E. Krumbein, Y. Van Ingelgem, A. Hubin, and P. Claeys, “Microbial dissolution of hematite and associated cellular fossilization by reduced iron phases: A study of ancient microbe-mineral surface interactions,” *Astrobiology*, vol. 9, no. 8, pp. 777–796, 2009.

[214] D. Zhao, X. Wang, S. Yang, Z. Guo, and G. Sheng, “Impact of water quality parameters on the sorption of U(VI) onto hematite,” *J. Environ. Radioact.*, vol. 103, no. 1, pp. 20–29, 2012.

[215] S. Xu, A. H. Habib, S. H. Gee, Y. K. Hong, and M. E. McHenry, “Spin orientation, structure, morphology, and magnetic properties of hematite nanoparticles,” *J. Appl. Phys.*, vol. 117, no. 17, 2015.

[216] R. dos Santos, M. Patel, J. Cuadros, and Z. Martins, “Influence of mineralogy on the preservation of amino acids under simulated Mars conditions,” *Icarus*, vol. 277, no. 2016, pp. 342–353, 2016.

[217] A. Ruíz-Baltazar, R. Esparza, G. Rosas, and R. Pérez, “Effect of the Surfactant on the Growth and Oxidation of Iron Nanoparticles,” *J. Nanomater.*, vol. 2015, 2015.

[218] L. E. LAGOEIRO, “Transformation of magnetite to hematite and its influence on the dissolution of iron oxide minerals,” *J. Metamorph. Geol.*, vol. 16, no. 3, pp. 415–423, 2004.

[219] E. R. Monazam, R. W. Breault, and R. Siriwardane, “Kinetics of magnetite (Fe3O4) oxidation to hematite (Fe2O3) in air for chemical looping combustion,” *Ind. Eng. Chem.*

Res., vol. 53, no. 34, pp. 13320–13328, 2014.

[220] T. C. Alex, R. Kumar, S. K. Roy, and S. P. Mehrotra, "Leaching behaviour of high surface area synthetic boehmite in NaOH solution," *Hydrometallurgy*, vol. 137, pp. 23–32, 2013.

[221] Á. B. Sifontes *et al.*, "Preparation of functionalized porous nano-γ-Al2O3 powders employing colophony extract," *Biotechnol. Reports*, vol. 4, no. 1, pp. 21–29, 2014.

[222] F. Dillon, M. Copley, A. A. Koós, P. Bishop, and N. Grobert, "Flame spray pyrolysis generated transition metal oxide nanoparticles as catalysts for the growth of carbon nanotubes," *RSC Adv.*, vol. 3, no. 43, pp. 20040–20045, 2013.

[223] W. P. Kwan and B. M. Voelker, "Rates of hydroxyl radical generation and organic compound oxidation in mineral-catalyzed fenton-like systems," *Environ. Sci. Technol.*, vol. 37, no. 6, pp. 1150–1158, 2003.

[224] I. Oller, S. Malato, and J. A. Sánchez-Pérez, "Combination of Advanced Oxidation Processes and biological treatments for wastewater decontamination-A review," *Sci. Total Environ.*, vol. 409, no. 20, pp. 4141–4166, 2011.

[225] Y. Lin, C. Yang, R. Xiu, J. Wang, Y. Wei, and Y. Sun, "Decolorization of methyl orange by green rusts with hydrogen peroxide at neutral pH," *Water Sci. Technol.*, vol. 69, no. 2, pp. 371–377, 2014.

[226] N. A. Youssef, S. A. Shaban, F. A. Ibrahim, and A. S. Mahmoud, "Degradation of methyl orange using Fenton catalytic reaction," *Egypt. J. Pet.*, vol. 25, no. 3, pp. 317–321, 2016.

[227] A. E. Nogueira, I. A. Castro, A. S. Giroto, and Z. M. Magriotis, "Heterogeneous Fenton-Like Catalytic Removal of Methylene Blue Dye in Water Using Magnetic Nanocomposite (MCM-41/Magnetite)," *J. Catal.*, vol. 2014, pp. 1–6, 2014.

[228] M. Azami, M. Bahram, S. Nouri, and A. Naseri, "A central composite design for the optimization of the removal of the azo dye, Methyl Orange, from waste water using the Fenton reaction," *J. Serbian Chem. Soc.*, vol. 77, no. 2, pp. 235–246, 2012.

[229] M. A. Voinov, J. O. S. Pagán, E. Morrison, T. I. Smirnova, and A. I. Smirnov, "Surface-mediated production of hydroxyl radicals as a mechanism of iron oxide nanoparticle

biotoxicity," *J. Am. Chem. Soc.*, vol. 133, no. 1, pp. 35–41, 2011.

[230] S. S. Lin and M. D. Gurol, "Catalytic decomposition of hydrogen peroxide on iron oxide: Kinetics, mechanism, and implications," *Environ. Sci. Technol.*, vol. 32, no. 10, pp. 1417–1423, 1998.

[231] R. Istratie, M. Stoia, C. Păcurariu, and C. Locovei, "Single and simultaneous adsorption of methyl orange and phenol onto magnetic iron oxide/carbon nanocomposites," *Arab. J. Chem.*, vol. 12, no. 8, pp. 3704–3722, 2019.

[232] Y. Xiao and J. M. Hill, "Impact of Pore Size on Fenton Oxidation of Methyl Orange Adsorbed on Magnetic Carbon Materials: Trade-Off between Capacity and Regenerability," *Environ. Sci. Technol.*, vol. 51, no. 8, pp. 4567–4575, 2017.